MEASUREMENT OF INCLUSIVE LOW MASS MUON PAIR PRODUCTION BY 225 GeV/c PROTON AND CHARGED PION BEAMS WITH A LARGE ACCEPTANCE SPECTROMETER

Gregory G. Henry

March 21, 1978

THE UNIVERSITY OF CHICAGO

MEASUREMENT OF INCLUSIVE LOW MASS MUON PAIR PRODUCTION BY 225 GeV/c PROTON AND CHARGED PION BEAMS WITH A LARGE ACCEPTANCE SPECTROMETER

A DISSERTATION SUBMITTED TO
THE FACULTY OF THE DIVISION OF THE PHYSICAL SCIENCES
IN CANDIDACY FOR THE DEGREE OF
DOCTOR OF PHILOSOPHY

DEPARTMENT OF PHYSICS

BY

GREGORY G. HENRY

CHICAGO, ILLINOIS

JUNE, 1978

ACKNOWLEDGMENTS

These results are only possible through the intense and willing efforts of each of the experimenters involved in this project. These include Kelby J. Anderson, James G. Branson, Kirk T. McDonald, James E. Pilcher, Eli I. Rosenberg, Gary H. Sanders, A. J. Stewart Smith and Jon J. Thaler. In addition, I would like to express thanks to several people who assisted the project in various ways, including Gary Hogan, James Mueller, Cathy Newman, Rob Pisarski, and John Zerolis. We must thank the Fermilab neutrino line staff who were always cheerful and helpful throughout the run. Both of the University technical staffs were most helpful at all times, including Ken Wright, Walt Bell, Walt Davidson, and Dick Raberman from Princeton. From Chicago, I thank Richard Armstrong, Cliff Brill, Robert Byrnes, Richard Northrup, Glenn Okazaki, Robert ("Archie") Ryan most warmly for their ready and gracious assistance. Bob Norton, Ken Burns and John Dudas were always willing to be of assistance when work on the electronics was needed. The staff of the Fermilab Computer Department deserves special praise for being patient and cooperative to an extent rarely found among data-processing staffs. Marypat Sharer helped greatly throughout the work.

Of those connected with the experiment, Cathy, Kelby, Kirk and Eli deserve special praise. All these people provided many interesting conversations and help. Kelby and Kirk, in addition, also helped by reading portions of this thesis and making many useful suggestions. Eli not only bore the brunt of the sloppy prose by reading through all of the document several times, but offered useful suggestions, keen criticism, and much-appreciated knowledge. Kelby was extremely patient and helpful during the analysis and without his willing cooperation and his talent this stage would have been more difficult, even out of all proportion to the long hours he spent on it. All of the above people deserve much thanks for their work. These last few deserve special credit for making the work interesting and educational.

TABLE OF CONTENTS

LIST OF TABLES

LIST OF ILLUSTRATIONS

CHAPTER I

INTRODUCTION

In a series of experiments performed from 1972 to 1975,[1-10] "prompt" single electron and muon signals from hadronic reactions were observed to be larger than those attributable to known sources. For electrons, "prompt" is defined to be that signal remaining after the electrons from Dalitz and Bethe-Heitler produced pairs, and from Ke_3 decays, were subtracted away. For muons, the particles of interest here, "prompt" is defined to be that signal remaining after the muons produced by pion and kaon decay are subtracted away. The muons are thus either produced directly or are the decay products of sources with lifetimes shorter than $\sim 10^{-10}$ sec.[11] The observed prompt muon signal divided by the pion signal of the same charge (signals corrected for acceptance), a ratio immune to many systematic errors, was found to be about 10^{-4} over a wide kinematic range. [A prompt electron signal of 10^{-4} compared to charged pions was also observed.] The production ratio seemed to be independent of beam energy and independent of transverse momentum (in fact, remarkably so).[12] These experiments had been done predominantly at 90° in the center of mass system.

Dimuon decays of known resonances, predicted electromagnetic sources of dimuons, and single muon decays of predicted particles could account for less than half of the observed single muon signal. Hence, it was hoped, in 1975, that the apparent anomalous prompt lepton signal was an indication of the production of new particles: vector mesons which decay into lepton pairs, or

perhaps "charmed" particles which decay weakly into single leptons plus neutrinos.

This thesis is written to report the results of an experiment designed to accurately assess the contribution by μ-pair sources to the large single muon signal, to detect any new dimuon sources (such as the then recently discovered ψ and ψ' particles), and to measure the production characteristics of mesons decaying to two muons. This experiment could also address the question of whether the prompt leptons occurred singly or in pairs. The experiment was performed in June, 1975, and in November, 1975--March, 1976, in the Muon Laboratory at Fermi National Accelerator Laboratory.

The Situation Prior to This Experiment

The production cross sections for sources of muons at Fermilab energies were poorly known prior to the experiment reported herein, but appeared insufficient to account for the large prompt single muon signal. Those sources and their estimated μ/π contributions are listed here.

(1) $\rho \to \mu^+\mu^-$ and $\omega \to \mu^+\mu^-$ [13,14]

In 1975, on the basis of experimental observation, one estimated $\rho/\pi \lesssim 1/10$ and that the production cross sections for ρ and ω were equal. Hence, noting that the branching ratios for $\rho \to \mu^+\mu^-$ and $\omega \to \mu^+\mu^-$ were about 4×10^{-5} and 8×10^{-5} respectively, the resulting μ/π ratio was about 1.2×10^{-5}.

(2) $\phi \to \mu^+\mu^-$

Although the φ is produced much less copiously than the ρ and the ω, its branching ratio to muon pairs is larger than that measured for the ρ by about a factor of four. An experiment at high p_T gave upper limits of 1.7×10^{-6} at $p_T = 2.48$ GeV/c and 3.0×10^{-6} at $p_T = 3.33$ GeV/c for the μ/π ratio due to

the ϕ.[15] Another experiment at 24 GeV/c in a bubble chamber gave a ϕ production cross section less than 2 per cent of the ρ cross section.[16] Thus, despite the higher dimuon branching ratio of the ϕ, the muon production would still be less than 0.1 that of the ρ, giving $\mu/\pi \lesssim 2 \times 10^{-6}$ from ϕ decay.

(3) $\psi \to \mu^+\mu^-$[17]

At the time this experiment was run, the ψ (or J/ψ) had just been discovered and offered the hope of being the source of single muons at high p_T. This was expected since the p_T distribution of the muons from the decay of the ψ peaks at about half of the ψ mass. Assuming the longitudinal and transverse momentum distributions to be similar to those of the pion led to an estimate of 0.2 for the fraction of prompt muons (at $p_T \approx 2.5$ GeV/c and $\sqrt{s} = 23.8$ GeV) originating from the ψ.[18]

(4) $\eta \to \mu^+\mu^-$ and $\eta \to \mu^+\mu^-\gamma$

The η was largely ignored in early estimates. However, if we use the branching ratio for $\eta \to \mu^+\mu^-$[19-21] and use typical production cross sections,[22,23] we can make a crude estimate of its leptonic contribution.

μ/π estimated to be $\lesssim 2 \times 10^{-6}$.

Using a predicted branching ratio of 3×10^{-4} for the eta Dalitz decay,[24] and the same production cross sections, we obtain a larger eta contribution and one which may yield a significant fraction of the μ/π ratio.

μ/π estimated to be $\lesssim 3 \times 10^{-5}$.

(5) Drell-Yan $\mu^+\mu^-$ pairs[25]

In this picture, quarks from one initial particle annihilate with anti-quarks from the other, giving a massive virtual photon which then materializes as $\mu^+\mu^-$ pairs. The Drell-Yan model was developed to explain the high mass μ

continuum observed at BNL in 1968.[14] The continuum contained a substantial amount of ψ production, though it was unrecognized as such. Being a one-dimensional impulse approximation model, it would apply best to high mass pairs of limited transverse momentum. Nonetheless, estimates of the contribution from low mass pairs have been made and suggest $\mu/\pi \lesssim 10^{-6}$.

A "correction" to this calculation[26] gives a larger contribution by including in the calculation the quarks produced in an initial hadronic reaction. However, though this mechanism seems to be promising from the standpoint of the total differential cross section evaluated at $x_F = 0$, behavior of the differential cross section was not estimated with respect to x_F,[27] p_T or mass.

μ/π ratio is estimated to increase by a factor of approximately 25 to $\mu/\pi \lesssim 2.5 \times 10^{-5}$.

(6) Constituent bremsstrahlung[28]

In this type of model, constituents from one initial particle emit bremsstrahlung, giving a timelike photon which materializes as $\mu^+\mu^-$ pairs. The μ/π ratio was estimated to be negligible from cross sections given by Ref. 28.

(7) Decays of higher mass particles

Theoretical speculation as to the existence of high mass states (intermediate vector bosons, heavy leptons, etc.) which could have leptonic decay modes present another possible source of direct leptons. However, the high μ/π ratio was observed at $\sqrt{s}$ = 11.5 GeV[29] (4.3 GeV for electrons[30]) and continued with no significant increase to $\sqrt{s}$ = 23.7 GeV[12] (62.4 GeV for electrons[31]).[1] Thus the massive states would have negligible contributions to this energy regime.

(8) Charmed particle production[32]

At the start of this experiment, no charmed particles had been seen,

though their existence was postulated. Such massive particles would decay very quickly, though weakly, and hence the decay signal could not be subtracted away in a manner analogous to that of pion decay. The possibility of a charmed particle contribution thus aroused interest in the initial reports of the prompt lepton signal.

This Experiment

Using the Chicago Cyclotron Spectrometer in the Muon Laboratory at Fermilab, we could measure x_F (the Feyneman x variable), from $0.07 \lesssim x_F < 1.0$, p_T (the transverse momentum) from $0.22 \leq M \leq 10.0$ GeV/c^2.. Schematic drawings of the beam transport and detection apparatus are shown in Figs. 1 and 2. Briefly, a hadronic beam was incident on a short nuclear target. The particles resulting from interaction in this target traveled through a series of multiwire proportional chambers (MWPCs) where their transverse positions were measured at several locations along the beam direction. These secondary particles then entered twelve absorption lengths of shielding (2 m of iron, called the hadron absorber) which filtered out electrons and hadrons. The emerging particles--mostly muons--had their tracks measured by more MWPCs and then they entered the magnetic field of the Cyclotron Magnet where the particles were deflected. Upon exiting the magnet, the muon's paths were measured by a series of spark chambers, and the particles entered another 2 m of iron hadron absorber ("Rochester steel") which absorbed any remaining hadrons. After traveling a short distance further, the muons then struck a scintillation counter hodoscope. If this array detected two particles, data acquisition was initiated.

For masses above 2.0 GeV/c^2, the opening angle at the interaction vertex was sufficiently large that the track information upstream of the hadron

absorber (i.e., prior to multiple scattering) was not needed for the analysis. A set of data was accumulated at a higher beam rate than the upstream MWPCs could tolerate and is reported elsewhere.[33] This report will deal with analyses utilizing the MWPCs which gave track information prior to multiple scattering. This approach allowed us to investigate the "terra incognita" of the low mass dimuon spectrum, and as will be shown, allows us to account for the high level of single direct muons.

CHAPTER II

THE APPARATUS, LOGIC AND DATA ACQUISITION

The experiment was performed at the Fermi National Accelerator Laboratory in the Muon Laboratory served by the N1 beam line (see Fig. 1). The hadron beam[34] was produced at 0.8 milliradians to an aluminum target bombarded by 400 GeV/c protons. This was followed by a 3600 ft long secondary beam line tuned to transport 225 GeV/c particles. The spot size of the beam at the Muon Laboratory was about 3.8 cm (horizontal) by 2.5 cm (vertical). When running with the positive beam the flux into the target was kept at or below 10^6 particles/spill to ensure high MWPC efficiencies; when running with the negative beam, the maximum obtainable flux of about 0.5×10^6 particles/spill was used. The positive beam was 80 per cent protons and 20 per cent pions. The negative beam was about 95 per cent pions. Additionally, about 3 per cent of the negative beam and less than 3 per cent of the positive beam consisted of kaons. For both beams, kaons were counted as pions both in the running and in the analysis.

Because of the long secondary beam line, about 4 per cent of the pions and 27 per cent of the kaons in the beam decayed. As a result about 0.2 per cent of the positive beam consisted of muons and a muon halo (muons entering the Muon Laboratory outside of the beam) was observed at the level of 6 per cent of the beam flux. The halo muons contributed no serious background as they were easily recognizable in the analysis stage.

The beam was directed into the Chicago Cyclotron Spectrometer, shown in Fig. 2, which utilizes the Chicago Cyclotron magnet as an analyzing magnet. Much of the spectrometer was built by the Chicago-Illinois-Harvard-Oxford (CIHO) collaboration studying μ-proton scattering.[35,36]

Beam Particle Identification

Three Cherenkov counters were located in the beam and were adjusted to identify mesons versus protons. The counters, C_2, C_3, and C_4 were 24.3, 30.4, and 39.5 m long, respectively, and all were 30.5 cm in diameter. They were filled with helium; the pressures were monitored continuously. The pressure was set just below proton threshold (2.75 psi) during positive beam running (see Fig. 3). For this data, pions were defined as two or three Cherenkovs firing (two pulses were allowed in order to compensate for counter inefficiency). Protons were defined as no more than one of the Cherenkovs firing (one pulse is allowed in order to compensate for accidental problems). The upstream counter was the most susceptible to accidental counts, as it was located after only one set of momentum-defining magnets and thus saw a higher particle flux than the others. For the negative data the Cherenkov information was not used.

Just upstream of the Muon Laboratory were two beam-defining scintillation counters, T_1 (7.6 x 7.6 x 0.64 cm) and T_2 (5.1 x 3.8 x 0.64 cm), with dipole magnets between them. Interleaved with these counters and these dipoles were two sets of scintillators surrounding the beam, each having 10.2 cm holes in the center and providing a signal with which one could veto beam-induced events. The definition of a beam particle required hits in T_1 and T_2 and no hit in any of the veto counters.

On entering the laboratory a beam particle was detected in two more scintillation counters before being allowed to trigger an event. The first, T_3,

was 7.6 x 7.6 x 0.64 cm, the second, T_4, was 3.8 x 3.8 x 0.32 cm. Both counters had a pulse height cut imposed at the trigger level; if more than one minimum ionizing particle was present in either counter, those particles were not allowed to trigger the apparatus (see Fig. 4). In addition, a hodoscope placed in anticoincidence with the beam counters was located between T_3 and T_4. This veto array (V_m) had a hole 5.1 x 5.1 cm in the center, allowing the beam to pass but vetoing halo particles. The beam counters and the veto counters overlapped, thus insuring one and only one particle in the beam.

The Beam Chambers

In order to measure the x and y[37] positions of the beam near the target, a series of eight planes of 6 cm x 6 cm MWPCs were placed between T_3 and T_4. This series consisted of four modules of two planes each; two modules consisted of an x and a y plane orthogonal to each other; the other two modules consisted of a u and a v plane orthogonal to each other and rotated by 45° with respect to the x and y planes. These chambers operated with the same readout system used by the other MWPCs as described below.

The beam chambers were installed and operating just prior to the positive 225 GeV/c data (positive beam). Thus, this information was not available for the negative data. The effect of this on the reconstruction will be discussed in the Chapter on Analysis.

During the 150 GeV/c run a series of four planes in two modules of two planes each (one x and one y) were used. These were located downstream of T_4, and had been installed for use by the CIHO collaboration.

The Target and Interaction Counter

Located immediately downstream of the beam counters was the target, either beryllium or carbon during the low mass runs. The beryllium target was

used in the 150 GeV/c run, and was 7.6 cm long, being chosen as a low A material with moderate density; during the 225 GeV/c run carbon of density 2.2 gm/cm^3 was used--this high density carbon target allowed a short target to be used, insuring a localized interaction point, while providing sufficient interaction probability. During negative running a 12.5 cm carbon target was used; during positive running this target was used for half of the data, being replaced by a 7.5 cm target for the remainder of the data. The two lengths of target were used, other conditions remaining constant, in order to check for possible effects due to secondary interactions in the target. As we will see, there were no evidences of such effects.

The target was immediately followed by an interaction counter, T_5, 7.6 x 7.6 x 0.64 cm. This counter was viewed by an RCA #8575 phototube whose voltage divider chain contained Zener diodes in the last 4 stages to provide a stable output signal in spite of high rate and high multiplicity. The T_5 output was discriminated so as to give a digital signal when two or more (charged) minimum ionizing particles emerged from the target. A pulse height curve for T_5 can be seen in Fig. 5. As will be seen in the section on the absorber chamber analysis, as long as two-charged-particle events were not eliminated from the trigger by T_5, normalization of events did not depend critically on the T_5 cut. The pulse height spectrum was monitored on-line and checked periodically during the run.

The 30 cm MWPCs

Located just downstream of the T_5 counter, and attached to the structure supporting T_5 and the target, were three multiwire proportional chambers, each having one x and one y plane and an active area 30 cm x 30 cm. These chambers were used to measure the trajectories of the particles produced in the target and helped to determine an interaction vertex. Fig. 6 shows the positions of the upstream chambers.

The 55 cm MWPC

One meter downstream of the target was the 55 cm MWPC. This chamber served to provide a high resolution measurement of the dimuon mass spectrum, and consisted of four planes of sense wires. The x and y planes measured the x and y coordinates of a (charged) particle passing through the chamber. The u and v planes were rotated 45° with respect to the x and y planes. We required that at least three intersecting wires be hit to determine a particle's position at the chamber. Details on the construction of the 30 cm, 55 cm and 80 cm chambers can be found in Appendix A. The upstream chambers operated at about 3700 V, with typical efficiencies of 0.85. The resolution, as determined from the analysis, was about 0.8 mm for each plane, and will be discussed later. The 55 cm chamber and the 80 cm chamber (described later) will be referred to as the absorber chambers when discussed in relation to the muon path identification. The 55 cm and 30 cm chambers will be referred to collectively as the vertex chambers when the interaction vertex identification is being discussed.

The Hadron Shield

Directly following the 55 cm MWPC and one meter downstream of the target was a hadron absorber composed of twelve absorption lengths of iron (2.02 m for the 225 GeV/c run, 2.18 m for the 150 GeV/c run). This served to filter out the hadrons created in a reaction, while allowing the muons to pass through. A muon of 20 GeV/c momentum will typically Coulomb multiple scatter about a centimeter transverse to its original path in the twelve radiation length of iron. Iron was chosen as a material of moderate Z--and hence moderate scattering--and of small absorption length, while still being easily obtained. The two meter length was chosen on the basis of beam tests on shower penetration through the absorber.[38] The iron thickness was shortened slightly during the

second run when an experimental study indicated that modest increases in length beyond two meters did not significantly reduce the emergent particle flux.

The one meter distance from the target to the hadron absorber was chosen as a compromise between decreased decay path for pions and kaons and increased separation of the muon tracks at the 55 cm chamber.

The 80 cm MWPC

In order to adjust the muon trajectories for the multiple scattering in the iron, another MWPC--similar to the 55 cm chamber--with an active area of 80 cm x 37 cm (in x and y) was placed midway through the iron. The information from this chamber, incorporated with the information on the momentum downstream of the hadron absorber, helped determine the expected hit position of the muon in the 55 cm chamber. Tests prior to the run showed that its location halfway through the shield was far enough downstream as to be protected from the hadron cascade in the shield and yet far enough upstream to be of use in extrapolating trajectories to the 55 cm chamber.

The J Hodoscope

On the downstream face of the hadron shield was a twenty element scintillation hodoscope shown in Fig. 7. This consisted of nine horizontal and eleven vertical elements, each 0.64 cm thick. For the data discussed in this report, the trigger required one or more particles detected in the horizontal array and one or more particles detected in the vertical array. This trigger will be called the J' trigger.

The J hodoscope was not present during the 150 GeV/c data, but instead the hodoscope labelled G in Fig. 2 was required to have at least one counter struck. The G hodoscope was located just downstream of the spark chambers (see below), and served the same function as the J--one hit in any G element was required in a good trigger. The G was a 20 element horizontal array.

The 1 m x 1 m MWPCs

Located directly downstream of the J hodoscope were eight planes of 1 m x 1 m MWPCs (4 x planes and 4 y planes). In general, the hits in these chambers were quite "clean"; the hadrons had been eliminated by the shield. In addition, these hits were well separated since the particles were now 3 meters downstream of the target. These chambers were operated at about 3.8 kV and efficiencies were typically 0.90 per plane per particle. Efficiencies were calculated in the analysis from the probability that a selected plane had a hit, given that hits from the same track were found in the other three planes in the same projection. The performance of these chambers was also monitored by the use of beam particle triggers and by the on-line collection of hit multiplicity statistics. The efficiencies measured this way were consistent with the figures derived from the analysis.

The wire spacing of the chambers was 1.6 mm and the resolution, as measured by distances of hits from the fitted tracks, was consistent with the theoretical limit, namely 0.46 mm.

These chambers measured the trajectories of the muons after multiple scattering. When combined with track measurements downstream of the magnet, this allowed a determination of the muon's momentum. The addition of the 55 cm chamber information and an adjustment to the momentum to account for the energy lost in the absorber, yielded the muon's momentum at the target.

The one meter chambers were built for the CIHO collaboration at the Enrico Fermi Institute in Chicago and the construction details are described elsewhere (see Ref. 36 and the reference contained therein).

The Chicago Cyclotron Magnet (CCM)

The Chicago Cyclotron magnet was used in this experiment for the momentum analysis. It had a gap height of 1.29 m and a physical pole radius of 2.15 m.

The magnetic field was axially symmetric and the uniformity of the field allowed a hard edge cylindrical field approximation to be used with an effective radius of 2.59 m. Using a flip coil at the central field of 14.6 kG, the field shape was mapped out carefully by the CIHO collaboration. This mapping was checked by both Hall probes and NMR probes at the central field value of 6.98 kG used in this experiment. The field strength was monitored periodically during the experiment and was found to be constant to within 0.3 per cent. For particles within the acceptance of this experiment, the hard-edge approximation was good to $\Delta p/p \simeq 0.5$ per cent in momentum.

The Spark Chambers

Located downstream of the magnet and just outside of the magnetic field, were twenty planes of spark chambers. The first twelve were 2 meters in height by 4 meters in width. The last eight planes were 2 meters in height by 6 meters in width (see Fig. 2). The spatial resolution was about 0.5 mm for each plane as determined from the data.

The 2 x 4 chambers were built at the Enrico Fermi Institute and had shift register readout.[39] The readout scanners used were the same type as those used for the MWPC readouts. These chambers were designed to operate in the fringe field of the CCM.

The 2 x 6 magnetostrictive spark chambers were built at Harvard University. They had a separate readout and encoding system.[35]

Of the twenty planes, nine had vertical wires (measuring directly in the x direction--the direction of deflection of trajectories by the CCM) and the remaining eleven had wires inclined at an angle of 0.124 radians to the vertical. The chamber construction is described elsewhere[35,36] and the operation was the same as described therein with the exception of the D.C. clearing field. The

polarity of the clearing field was reversed on the 2 m x 4 m chambers, resulting in a decrease in the memory time from about 10 μsec to 1 μsec. This resulted in more unambiguous track identification, since fewer tracks not associated with the event of interest were detected in these chambers.

Due to the large redundancy in the number of planes and hence spark information, the efficiency of reconstruction remained stable at about 0.90 per event throughout the low mass run.

The $V\mu$ Counter

In order to eliminate on a hardware level the triggering of the apparatus by a beam muon, a small (7.6 x 7.6 x 0.64 cm) scintillator veto was placed midway through the spark chamber area. This was centered on the deflected beam and any signal from the $V\mu$ counter was sufficient to veto the event (no event would be allowed to trigger the apparatus). This counter was repositioned when the beam polarity was reversed, since the polarity of the CCM was not changed during this run.

The Rochester Iron

Next, the muons entered another steel hadron absorber, from the former University of Rochester cyclotron. This steel was an average of about 2 m thick and served to rid an event of any hadrons that were able to "punch through" the upstream hadron absorber. One meter upstream of the steel was a lead wall 0.4 m thick, serving the same purpose.

The P Hodoscope

Located three meters downstream of the Rochester iron was the P hodoscope, the main element of the dimuon trigger. This was a bank of 53 scintillators, 27 above and 26 below the beam height. A diagram of the arrangement is shown

in Fig. 8. By requiring that either two non-adjacent (in the vertical or in the horizontal) elements or that more than two elements be hit, we could restrict the trigger to two separate muons penetrating the apparatus. A lead wall 0.20 m thick was placed just upstream of the P hodoscope in order to suppress delta rays originating in the Rochester steel or in the air between the steel and the hodoscope bank. This lead wall also created delta rays but these electrons, having originated much closer to the P bank, were confined closely to the muon track and tended to satisfy the non-adjacency trigger requirement. Monte Carlo studies showed that at a mass of 0.55 GeV/c^2, less than one per cent of muon pairs originating in the target would be lost due to this trigger requirement.

The P hodoscope hit distribution from the analyzed data was compared to the hit distribution obtained from the Monte Carlo. The x_F and p_T distributions from the data at the ρ-ω mass were fed into the Monte Carlo. The resulting counts of hits per counter were divided into the hits from the real data and the agreement was good. Shown in Fig. 9 is the resulting ratio for $p + C \rightarrow \rho + X$ and $\pi^+ + C \rightarrow \rho + X$.

The Logic and Trigger

A diagram of the fast electronics, composed of standard NIM and CAMAC modules, is shown in Fig. 10. T_1, T_2, T_3 and T_4 were the beam defining counters described above. V_m was the veto wall upstream of the target and surrounding the beam. V_μ was the small counter between the spark chambers, and served to veto beam muons. V_j was a set of vetoes near T_1 and T_2, which identified beam halo.

In the notation below + denotes a logical or of all +ed signals, $\cdot$ denotes a logical and, while $_{\geq 2}$ means that two or more single minimum ionizing particles were seen in a counter, and $\bar{}$ means that a signal is logically complemented.

Some of the important levels of the beam logic were

$$B'' = T_1 \cdot T_2 \cdot T_3 \cdot T_4$$

$$B' = T_1 \cdot T_2 \cdot T_3 \cdot T_4 \cdot (\bar{B}'' \text{ delayed by 20 nsec})$$

$$V = V_m + V_\mu + V_j + (T_3)_{\geq 2} + (T_4)_{\geq 2}$$

$$B = B' \cdot \bar{V}$$

$$B_I = B' \cdot \bar{V} \, (T_5)_{\geq 2}$$

Thus B'' is the minimum requirement to define a beam particle, B' includes the requirement that no particle was seen in the previous RF bucket (RF buckets are machine-created "slots" for the particles to travel in. At Fermilab the buckets are 2 ns wide and are separated by 18 ns). V is the or of all veto signald and the signal of two or more minimum ionizing particles in T_3 or T_4 (see the Apparatus Section). B is the final beam requirement: one and only one beam traveling through T_1 --- T_4. B_I is the B requirement and the requirement that more than one minimum ionizing particle travels through T_5.

The hodoscopes downstream of the hadron absorber served to identify events which included muons. The logic signals were

J' = one or more J element hit in x and one or more hit in y

G = one or more G counters hit

P = two non-adjacent P elements hit or more than two P elements hit.

For data acquisition, we demanded that the target interaction be associated with muons downstream of the magnet. Thus the dimuon trigger incorporated B_I and P. Interspersed with the dimuon trigger were triggers taken without the target interaction requirement. Because less than 34 per cent of the beam interacted with the target, triggers without the $T_{5_{\geq 2}}$ requirement were prescaled by a factor of 64. This trigger was used as a monitor of T_5 during the run and was also used to check on the efficiency of the T_5 cut and of vertex cuts. Thus the final triggers were

$$\left.\begin{matrix} B_I \cdot J' \cdot P \\ (B \cdot J' \cdot P)_{\text{prescaled}} \end{matrix}\right\} \quad 225 \text{ GeV/c}$$

$$\left.\begin{matrix} B_I \cdot G \cdot P \\ (B \cdot G \cdot P)_{\text{prescaled}} \end{matrix}\right\} \quad 150 \text{ GeV/c}$$

The pulse heights of beam defining counter and Cherenkøv counter signals were recorded for all triggered events. All counters were timed relative to T_3 and fixed duration coincidences were started by T_3. Both times and accidental coincidences were generated in the electronics and displayed on-line and recorded on tape for cross-checking during analysis.

Computer Data Acquisition

The electronic trigger initiated the data recording. The SIGMA III computer received a signal to prepare for data acquisition. At the same time, the spark chambers were fired and a veto was placed on any additional data acquisition. After a short time for noise from the spark chambers to die out, the readouts of the wire chambers was initiated. The computer then received chamber, counter, and beam information from a CAMAC system and stored the information in its memory. At the end of the beam spill, event information, as well as beam spill information, was written on magnetic tape. The total dead-time imposed on the electronics during one event was 20 msec.

During the run the SIGMA monitored the performance of the equipment. Hodoscope hit distributions, wire chamber illuminations, wire chamber hit multiplicities, plane efficiencies, Cherenkov and trigger counter pulse height distributions, coincidence information, and beam and trigger information were monitored by on-line cathode-ray tube displays and by computer print-out. Event displays were generated showing the location of the chamber and counter hits. An on-line track finder aided in correlating these hits. Faulty CAMAC data

transfers and other readout faults were diagnosed and communicated to the experimenters.

All recorded information was written on magnetic tape at the end of each beam spill, in one or more 600 word (16 bits/word) records. An abbreviated off-line analysis program checked the performance of the spectrometer on a run-to-run basis.

CHAPTER III

THE ANALYSIS AND MONTE CARLO

Analysis of the data proceeded in four stages. In the first stage the raw data tapes were analyzed to (1) obtain beam tracks, (2) find good muon tracks downstream of the hadron absorber, (3) link the tracks upstream and downstream of the magnet, and (4) determine the momenta of the muons. In the second step this information was incorporated with the low mass analysis. The upstream chamber information was analyzed to (a) find valid hits in the 55 and 80 cm chambers, (b) find an interaction vertex from "hadron" tracks in the 55 and 30 cm chambers, and (c) make improved calculations of the effective dimuon mass, x_F and p_T. In the third stage final cuts and histograms in mass x_F and p_T could be generated and events were weighted by acceptances. In the fourth stage the histogram information was combined with beam and target information to yield cross sections. The first stage of the analysis is described elsewhere in detail,[33] so only a brief description will be given here.

The Beam Track Finder

For the 150 GeV/c data, beam chambers which gave x and y information were used. If several chambers yielded information, a least squares fit was applied. If only one chamber gave x or y information, the x or y information was used directly.

For the 225 GeV/c data the four beam chambers described previously were installed just upstream of T_4. Because beam tracks are parallel within these chambers, the x and y information was obtained by projecting all x, y, u and v

information to a common z value and a clustering was searched for in x and y. This analysis at a common z position was possible because of the small beam divergence.

For the negative data, the straightest (least slope) track in the 55-30 cm system was extrapolated to the target to obtain a "beam track" in x and y.

The beam track information was used to aid the 30 and 55 cm chambers in determining accurately the interaction point in the target. Further discussion of this point appears in the Vertex Analysis section.

The 1 x 1 Track Finder

Since the 1 x 1 meter chambers yielded "clean" tracks and the plane efficiencies were high, the momentum analysis started in these MWPCs. In the first step, the track finder searched for three and four plane hits in the x and y projections. This was done by searching for hits inside a zone three standard deviations wide around a line connecting pairs of hits in the same view. If a three or four wire track could not be found, two wire "tracks" employing unused hits were allowed. In all cases, track candidates were required to have a χ^2 probability greater than 0.02 for originating in the target. In cases where two tracks shared more than one hit, the track with the greater χ^2 was excluded from the set of possible upstream tracks.

The Downstream Track Finder

In the second step, the spark chambers downstream of the CCM were searched for tracks. Due to the efficiency of the spark chambers--typically 83 per cent for the 2 m x 4 m chambers, and 93 per cent for the 2 m x 6 m chambers--and the large number of them, a simple combinatorial track-fitting method similar to the 1 x 1 track finder was impractical to use downstream. As a result, a

more sophisticated algorithm was employed. The x projection was analyzed first. For each upstream track in the x projection, we could obtain an impact parameter. Since any cylindrically symmetric magnetic field will "conserve" a particle's impact parameter, any valid x track upstream can provide one of the two parameters necessary to specify the corresponding track downstream. The other parameter is provided by a hit. Each downstream hit, when associated with each upstream impact parameter, will yield a possible downstream track. The intersection of such a possible track and a plane at a fixed arbitrary z position--our z plane was chosen near the middle of the spark chambers--would yield a point on that plane. A series of such hits from the same track would result in a clustering of such points. Points within a 3 mm window around the cluster were used to select x hits for use in calculating the x projection of the downstream track.

Since the u' and v' wires of the spark chambers were inclined at small angles to the x wires, for a given x-hit included in the x projection fit, the associated u' or v' hit could be found. The intersection of these wires would yield a y position. The intersection of the lines joining these points to the target at the common z plane would yield another clustering. A set of y hits were chosen within a window of 12.5 mm of one another.

All the remaining x and y hits were then fit to yield a new line. Hits within 4 mm of this line were used as downstream track candidates if they included three or more x hits and three or more u' or v' hits distributed over 62 cm along the track line.

Final downstream track candidates were those tracks which pointed, within a small momentum-associated error, to a struck P hodoscope counter.

Linking

In the third step, the upstream and downstream tracks were paired to provide complete particle tracks. Figs. 11, 12, and 13 display the impact parameter,

y intercept and y slope differences of tracks upstream and downstream of the magnet. To define an acceptable trajectory, tracks must have had impact parameters within 25 mm of each other. In addition, the quantity

$$\left(\frac{\text{y intercept difference}}{25\text{ mm}}\right)^2 + \left(\frac{\text{y slope difference}}{.005}\right)^2$$

had to be less than 25.0 for an acceptable link. The denominators were determined from the widths of the corresponding difference plots. The use of the sum is an attempt to approximate empirically a χ^2-like cut quantity. The cut was chosen so as to include events not otherwise known to be suspect.

Momentum Cuts

In order to eliminate any problems from beam muons in the analysis described so far, a cut was made on events which had high momentum muons. If either muon passed within 38.1 mm in x and 38.1 mm in y of the V_μ counter, the event was cut. This cut was imposed to eliminate any final positioning problems with that counter. The size used was larger than that of the counter. Additionally, any muon with momentum greater than 180 GeV/c (120 GeV/c for the 150 GeV/c data) and any muon with momentum greater than 150 GeV/c and with a slope in the 1 x 1 MWPCs less than 0.006 was cut. These requirements eliminated about 2 per cent of the remaining tracks.

Rate Constancy

The event rates for the analysis described thus far versus the data runs are shown in Fig. 14. The ordinate is the number of good events satisfying the J' trigger requirement divided by the number of incident beam particles, all normalized to one. We see that the event rates are stable through the run.

The Vertex Analysis

For the 225 GeV data the 30 cm and 55 cm chambers were used to find the interaction vertex. For a typical interaction the emergent secondary particles were confined to a small cone about the extrapolated beam particle track. Most of these particles were hadrons and were absorbed by the 2 meters of iron. In principle only two muons could travel all the way through the iron, trigger the apparatus, and be momentum analyzed in the downstream chambers. Nonetheless, the hadrons did yield valuable information since their tracks in the chambers upstream of the absorber pointed to the interaction vertex. An accurate knowledge of the vertex helped to improve the probability of finding the muon hits in the 55 cm chamber. The small search zone in x and y in the 55 cm chamber was defined by the error (which scaled as 1/p) associated with the extrapolated hit position. The vertex knowledge in the z dimension also helped to improve the knowledge of the opening angle of the muons.

During the analysis the relative alignment of the 30 cm and 55 cm planes was determined from the data to an accuracy of about 0.1 mm (1/15 of a wire spacing). Least square fits were then applied to the hits in the chambers and in each projection only tracks with three or four planes hit (out of a possible four) and with a χ^2 probability greater than 0.10 were kept. A number of good tracks were rejected by the χ^2 test, but the tracks and hence hits were so dense that this was the only way to eliminate extraneous track solutions. These tracks were then candidates for another χ^2 fit to the best estimate of the interaction vertex. If N, the number of good tracks so found, was less than three, the following analysis was not used, and the target center was used as the best estimate of the z position of the vertex, with the x and y positions given by the beam chambers.

If N was greater than two, ten equally spaced positions in the target were tested as possible vertices. Given such a position, "zs", and estimated x and y positions of the vertex as given by the beam chambers, "x beam" and "y beam," we can find the n "hadronic" tracks most closely approaching the point (x beam, y beam, zs). The following chart gives n as a function of N.

N	1	2	3	4	5	6	7	8	9	10	11	12	13	14	15	16
n	/	/	3	4	4	4	4	4	5	5	5	5	6	6	6	6

Using an $n \leq N$ was an attempt to eliminate problems associated with secondary interactions. These n tracks were recorded and the other nine trial zs positions were sampled. These ten trials typically yielded two to five different combinations of n lines. Each different combination had a χ^2 test imposed which yielded a possible vertex position (x_p, y_p, z_p).

Given n tracks with slopes m_i, intercepts b_i, and errors in the transverse positions σ_i, along with x beam and y beam and their errors, $\sigma_{x\ beam}$ and $\sigma_{y\ beam}$, we can calculate a χ^2 for the n tracks having originated from the point (x,y,z). This is

$$\chi^2 = \sum_{i=1}^{n_x} \left[\frac{(x - m_{xi}z - b_{xi})^2}{\sigma_{xi}^2} \right] + \frac{(x - x\ beam)^2}{\sigma_{x\ beam}^2}$$

$$+ \sum_{i=1}^{n_y} \left[\frac{(y - m_i z - b_{yi})^2}{\sigma_{yi}^2} \right] + \frac{(y - y\ beam)^2}{\sigma_{y\ beam}^2}$$

Upon minimizing, we found a possible vertex point. If all n lines were in the x(y) view, the χ^2 was appropriately redefined and the vertex point was (x_p, y_{beam}, z_p) [or (x_{beam}, y_p, z_p)]. Solutions with z_p within 17.5 mm of the target limits and within the estimated resolution for that vertex were candidates for the final vertex choice explained below. The wire spacing of 1.6 mm ideally yields an rms deviation of $\sigma = \frac{1.6\ mm}{\sqrt{12}} = 0.46$ mm. However, the situation is complicated, and σ is enlarged, by other factors, particularly the wire hit multiplicity.

The σ calculated by folding in this factor is about 0.8 mm and agrees with the experimental distribution of fitted tracks to the his position distances. Thus the σ_{xi} and σ_{yi} at the target are obtained by using a σ for each hit on each plane of 0.8 mm.

If the distance of a given plane (or hit in that plane) from the vertex position is Δz and the number of hits for a given track is N, the relation between σ and σ_i is

$$\sigma_i = \sqrt{\frac{\sigma^2(\Sigma\Delta z^2)}{\Sigma\Delta z^2 - (\Sigma\Delta z)^2}}$$

This was the value inserted in the χ^2 equation for the expected error in the position within the target.

The vertex resolution was calculated by finding the z such that $\chi^2(x_0,y_0,z) = \chi^2(x_0,y_0,z_0) + 1$. Then the estimated resolution was $|z-z_0|$ where (x_0,y_0,z_0) is the best fit to the interaction vertex. The resulting resolution distribution is shown in Fig. 15.

With an average of about eight particles produced in a primary reaction in the short carbon target, 54 per cent of the primary interactions were accompanied by one of more secondary interactions--70 per cent in the long C target. Consequently, not all of the hadronic tracks detected by the upstream chambers originated at the primary vertex. Thus the set of trial points, the (x_p,y_p,z_p)'s could not be expected, even within errors, to yield a common interaction vertex. In order to avoid choosing secondary vertices from among the candidates (see Fig. 16), the most upstream vertex with an acceptable χ^2 was chosen for the interaction vertex.

The sensitivity to the χ^2 probability cut was investigated. Between a probability of 0.05 and 0.20 the mass resolution of the sample of events satisfying the cut was not noticeably affected. However, the number of events fit with the calculated vertex did decrease as the cut was lowered below the final value of 0.10.

The z distribution of "primary" interactions in the target can be seen in Fig. 17. This distribution can be compared qualitatively with a simple Monte Carlo distribution of primary interactions. For this simulation, the distribution is that of an exponentially absorbed beam interacting with the long carbon target and with the resulting interaction position smeared by the experimentally estimated resolution from Fig. 15 (see Fig. 18). Interaction "vertices" found outside of the target were pulled back into the target by the same algorithm described above.

The most downstream vertex from the data can also be found (see Fig. 19). This can be compared qualitatively with a second Monte Carlo distribution of interaction vertices using an average charge multiplicity of $\langle n \rangle = 8$ from a primary interaction, shown in Fig. 20. When no particles "interacted," the primary vertex was plotted. Only one secondary vertex per event was plotted and no tertiary vertices are plotted. The vertex position is smeared as above. The real data vertex finder has its job complicated in both the most upstream and the most downstream plots in having to choose vertices using both secondary and tertiary tracks. Given this complication the Monte Carlo agreement is reasonable.

The secondary interactions did not contribute a significant dimuon signal to the data. This can be seen from Fig. 21, taken from data analyzed without upstream chamber information. This is a graph of the ratio of the differential (in x_F) cross section obtained from the long C target to that obtained with the short C target. A dimuon from a secondary vertex will be produced with a lower longitudinal momentum than the (secondary) particle which produced it. Hence we would expect that a significant dimuon signal from secondary interactions would express itself in a ratio, at low x_F, greater than one. This is not seen. A similar test using the upstream information will be shown below.

The additional effect on the x_F distribution due to the vertex analysis can be tested on events with mass in the ρ-ω peak. The ratio of events with x_F lower than 0.30 to events with x_F greater than 0.30 is 2.75 with the vertex analysis. The same ratio without the vertex analysis--using the target center for the vertex--was 2.78 ± 0.02. The same ratio using the z_p with the minimum χ^2 yielded events with a ratio of 2.64.

In the final analysis, the calculated vertex was used if the probability associated with the χ^2 test was greater than 0.10 and the resolution in z was better than 30 mm. If not, the target center was used as the vertex position. While this method probably pushed the vertex upstream, on the average, the overall effect of this analysis was beneficial, as this method increased the number of events fit in the 55 and 80 cm chamber analysis by about 3 per cent.

Figure 22 shows the x and y views of the computer displays of the vertex finder for a typical event. T denotes the corners of the target. I denotes the best vertex estimate, + the tracks available for use by the routine, x and y the hits in the chambers, - the plane positions.

The 55-80 cm Analysis

Given the muon track momenta downstream of the hadron shield (see Fig. 23), the effective dimuon mass is given by

$$M_{\mu\mu}^2 = 2\mu^2 + 2E_1E_2 - 2p_1 p_2 \cos(\theta'_{12})$$

$$\theta'_{12} = \theta'_1 + \theta'_2$$

where μ is the mass of the muon (105.66 MeV/c^2), E_1 and E_2 are the energies of the muons, p_1 and p_2 are the magnitudes of the muons' momenta (corrected for energy loss on the hadron absorber) and θ'_{12} is the opening angle of the muons as determined after multiple scattering (θ'_1 and θ'_2 are the observed angles downstream of the hadron absorber).

However, incorporating the upstream information, the mass of the dimuon can be calculated more accurately. From the downstream momenta and the vertex position of the interaction, a χ^2 calculation can be done to yield the most probable opening angle. Using the resulting angles, θ_1 and θ_2, with $\theta_{12} = \theta_1 + \theta_2$, a better estimate of the dimuon mass may be obtained. For the detailed calculation of θ_1 and θ_2 we refer to Appendix B.

In a similar manner, the most probable x and y position of the muon track at the 80 cm chamber can be found by a χ^2 minimization, given the momentum downstream of the hadron shield and information on the vertex. The 80 cm chamber is then searched in the region of the expected hit. Using this new hit (if found) along with the downstream momentum and the vertex position, we repeated this procedure in identifying muon hits in the 55 cm chamber. The hit is then looked for within a small distance, and the new hit defines an x or a y. To be kept as a good event, both muons had to have had a found hit in the 55 cm chamber.

Prior to the analysis, the plane alignment was carefully checked and all planes were aligned to about 0.1 mm with respect to one another.

The pattern recognition proceeded in three steps. First all x-y wire combinations were used to predict a u and a v position. Then the u and v wires were searched for hits within one wire spacing of this position (1.59 mm). All good three or four wire combinations were kept. The procedure was repeated but with the roles of the x and y and the u and v planes interchanged. Wire sets thus found were called NSETS combinations and were numerous--for an event with the average plane hit multiplicity of about 10, the number of NSETS wires was occasionally as great as 200.

A number of criteria was used to reduce the number of NSETS. For each wire in the above patterns, a wire could appear in several sets. In order to

limit the number of sets retained, only the "best" set of the several sets was kept for each wire. A four wire set was chosen preferentially over a three wire set and within such groupings the set having the smallest spatial separation was kept. For a four wire set, the spatial separation is given by

$$|u(\text{obtained from the x-y intersection}) - u(\text{from the u wire})|$$
$$+ |v(\text{obtained from the x-y intersection}) - v(\text{from the v wire})|.$$

For three wire sets the separation was similarly defined. The remaining combinations, called KSETS, were still greater than the number of hits.

The third and last step was to form a set of combinations called LSETS. For each wire, KSETS was searched for the number of times that a given wire was used in distinct sets. If the wire was used only once, the set it was used in was added to LSETS. For those sets with wires used more than once, the program looped over the wires used just twice to find the wires that had not been used in any of the LSETS combinations yet. If all the wires to be found in any pairing had been used by this time, LSETS was in its final form. If any struck (and paired in KSETS) wire was still missing the number of allowed couplings was increased to three and the sets were searched for sets containing the missing wire. If all wires were used, LSETS was complete; if not, four couplings were allowed, and so forth until the maximum number of couplings was allowed. As a final step, any set where all of its wires were used by other sets in LSETS was thrown out.

The number of sets in NSETS was very high, averaging about 80; the number in KSETS was typically 16, and the number in LSETS averaged about 12. The peak to background ratio using NSETS was no better than that using no chamber information at all because there were many extraneous combinations among the "hits." These extraneous combinations were almost completely eliminated by using LSETS and imposing the χ^2 test described earlier. Two checks can be made

on the LSETS effectiveness by using tracks downstream of the absorber from one event and trying to make these tracks fit LSETS hits in the following event. This gives a measure of the upper limit of the background introduced by this procedure. The distance from such a track at the 55 cm chamber to all LSETS hits within the chamber can be plotted and this distribution can be compared to a similar distribution for real tracks. This plot is given in Fig. 24. A strong real track signal can be seen as well as a signal due to uncorrelated track-hit pairs. The background level shown is an upper limit for finding single track-hit pairs; our experiment requires two such hit-pairs.

A plot can be made of the track-hit pairs which actually pass the analysis cuts and yield a dimuon mass. As can be seen in Fig. 25 the false track events were greatly suppressed by the χ^2 requirement of matching an LSETS hit with an allowed hit position. This analysis "background" was on the 8 per cent level for completely uncorrelated track-hit combinations. This "background" was not subtracted from the signal. As explained, the "background" was obtained by assuming no correlations between the downstream tracks and the hits in the absorber chambers. The trigger, however, required that the muons were produced in the target and therefore that the particle-hit combinations were strongly correlated. Moreover, the Monte Carlo (soon to be discussed) had uncorrelated absorber chamber wire hits superimposed on the muon hits. Reconstructed Monte Carloed events showed no obvious background.

It should also be noted that the requirement that tracks match to hits in the 55 cm chamber suppressed events that were simulated by decays outside of the target--the χ^2 hit position was calculated using a vertex in the target--as a decay particle would typically have a kink in its track and thus in general the real hit position was outside of the χ^2 search zone. A measure of this

decay background can be determined from the level of like sign muon pairs ($\mu^+\mu^+$ and $\mu^-\mu^-$) satisfying the analysis requirements. A discussion of decay backgrounds will be seen in the RESULTS section.

Another potentailly serious source of background events was suppressed by use of the 55 cm chambers. A secondary particle could interact in the hadron absorber and give rise to a muon pair. The requirement that two LSETS hits be found in the 55 cm chamber however, suppressed such events greatly, for again, a most likely track position in the 55 cm chamber was calculated assuming that the interaction took place in the target and hence uncorrelated hits had to be found in the (mis)calculated positions in the absorber chambers in order to fake an event. Monte Carlos were run simulating dimuon production from the hadron absorber. The resulting downstream "tracks" and false 80 cm MWPC hits were then combined with wire hits from the data. These fake data were then analyzed with the normal analysis program. The number of such events generated at a mass of 300 MeV/c^2 and accepted by the analysis was less than 1/17 that of comparable events Monte Carloed from the target. This suppression factor of absorber-induced events was even greater at higher masses.

In Fig. 26, we see a plot of the mass spectrum calculated without the benefit of the low-mass analysis, i.e., with only the fit-mass available. This can be compared directly with Fig. 27, which utilizes the low-mass analysis. We see that the ρ-ω peak is clearly visible in the first plot but that there is no suggestion of a ϕ peak. In the second we see the small ϕ peak and we see a much-improved ρ-ω peak. In Fig. 26 we have recalculated the mass, using the vertex calculation, and we see a slightly improved ϕ peak. We note that the very low mass contribution remains in the second and third plots and hence we infer that the contribution does not originate with the shield.

The Monte Carlo and Acceptance

To determine the acceptance of the apparatus over the kinematic range of the experiment, a Monte Carlo program was run at discrete points in mass, x_F and transverse momentum. The matrix of input points consisted of

225 GeV/c Data

7 x_F points at 0.07, 0.10, 0.15, 0.20, 0.40, 0.60, 0.80

7 p_T points at 0.0, 0.5, 1.0, 1.5, 2.0, 2.5, 3.0 GeV/c

8 mass points at 0.22, 0.32, 0.40, 0.50, 0.75, 1.0, 1.5, 2.0 GeV/c^2

150 GeV/c Data

8 x_F points at 0.125, 0.15, 0.20, 0.30, 0.40, 0.50, 0.60, 0.80

5 p_T points at 0.0, 0.5, 1.0, 1.5, 2.5 GeV/c

6 mass points at 0.25, 0.35, 0.50, 1.0, 1.5, 2.0 GeV/c^2

A dimuon was generated in the target consistent with known absorption cross sections and with a fixed mass, x_F and transverse momentum. Decays of these dimuons were generated isotropically in the center of mass system. Monte Carlo studies showed that complete polarization would affect the overall normalization by less than 20 per cent.

The produced dimuons multiply scattered in the remainder of the target and then drifted to the 55 cm chamber where the experimental resolution and efficiency were used to determine the probability of a given wire being struck. Real-data "hadronic" wire hits were superimposed on these Monte Carlo events in order to accurately simulate the wire-sorting problems of the actual data. The muons were then multiply scattered through the iron and again the "hits" were superimposed on some 80 cm chamber real-data hits and with appropriate efficiencies. The trajectories were deflected by the magnet and were also multiply scattered at the Rochester iron. Energy loss tables were obtained from a previous Fermilab study[40] and were used in both the analysis and the Monte Carlo.

Fluctuations in energy lost in the various scatterers were included in the Monte Carlo. Hits were imposed on the P hodoscope elements at the appropriate positions. These "events" were recorded on magnetic tape and were analyzed by the data analysis program (including wire sorting, satisfying the P non-adjacency requirement, missing of V_μ, and satisfying momentum cuts, to be described later). From 2000 to 10000 such events were generated for each input point in 12 minutes of CDC 6600 central processor time. This time was necessary because of the complexity of the pattern recognition within the 80 and 55 cm chambers. The number of events reconstructed by the program divided by the number of generated events constituted the acceptance factor of the experiment at that kinematic point. Acceptances over the range of the data were typically 0.10 to 0.40, including the folding-in of wire chamber plane efficiencies. The acceptance of the experiment did extend below $x_F = 0.07$. However, that cutoff was imposed on the data in order to assure that individual events, when weighted by the reciprocal of the acceptance, did not appreciably affect the final x_F distributions.

Once acceptance factors were determined for the matrix of points, a third degree polynomial was used to smoothly interpolate the shape of the acceptance between points. Such a fit was allowed because of the gentle varying acceptance as a function of mass, x_F, and p_T. This polynomial fit was checked in detail for the acceptance values across many "slices" in the three dimensional space. The fits were smooth and reasonable across all input values.

In addition, the acceptance weighting was checked by feeding a flat spectrum in x_F and p_T at discrete masses into the Monte Carlo and analyzing and weighting Monte Carloed events as was done with the data. The resulting spectrum accurately reproduced the input spectrum. This indicates (1) that

the acceptance weighting algorithm was reasonable, and (2) any net shifts in observed quantities due to the analysis did not visibly affect the acceptance weighting. During the real data analysis events with acceptance weighting greater than 25 were printed out by the computer. The number of such events was very small and did not appreciably affect the overall results.

Resolution

The effects of various measurement errors and uncertainties on the momentum and mass of the dimuon events were studied. As determined by the Monte Carlo without the low mass analysis, the following sources contributed to the mass resolution at 1 GeV/c^2:

Source	Contribution
Multiple scattering in hadron absorber	80 MeV/c^2
Energy loss in hadron absorber	18
Measurement of errors in chambers downstream of the hadron absorber	13
Vertex position uncertainty (in z)	22

These are the standard deviations of the resulting mass spectrum at the input mass. In each case these were determined by "turning off" all contributions but the one in question. When combined in quadrature, the errors account for about 86 MeV/c^2. The Monte Carlo resolution at 1 GeV/c^2 is about 100 MeV/c^2 (σ) which is consistent with a mass plot of the data, which can be seen in Fig. 26.

For the low mass analysis, the energy loss in the hadron absorber and the measurement errors in the chambers downstream of the absorber still contributed to the overall error. As a result of the 30 cm-55 cm MWPC analysis the vertex position estimate was improved on the average, although the estimate in individual cases could be worse than that obtained from the target center estimate. The overall contribution from this source is about 12 MeV/c^2, deter-

mined from the overall resolution in z of about 20 mm. The uncertainty in the upstream track measurement was calculated to vary from about 25 to 35 MeV/c^2 depending upon whether both muon hits in the 55 cm chamber were four wire hits, one was a four wire hit and one was a three wire hit, or both were three wire hits. If the muon path extrapolation-particle hit correlation was not perfect, the error would be greater. Thus we had contributions from the upstream analysis due to both measurement errors and the reconstruction technique. The overall estimates of the standard deviations at 1000 MeV/c^2 thus follow.

Source	Contribution
Upstream analysis	35 MeV/c^2
Energy loss in hadron absorber	18
Downstream measurement	13
Vertex position uncertainty	12

These errors, when added in quadrature, amount to 43 MeV/c^2. If the errors were not independent as could have happened, for example, if a wrong vertex position estimate led to an improper hit pattern in the 55 cm MWPC, the total was greater. Monte Carlo studies using a fixed mass and the measured p_T and x_F distributions led to an estimate of about 60 MeV/c^2 at 1 GeV/c^2 for the total. This is consistent with Fig. 28.

CHAPTER IV

THE RESULTS

The mass spectra resulting from the low-mass analysis are shown in Figs. 29 to 31. Before discussing these results in detail, we consider possible background sources, which while producing valid $\mu^+\mu^-$ events, are not directly produced.

Normalization

Events were binned in x_F and in p_T for each of the five mass intervals studied. Cross sections per bin and total cross sections from the bin totals were obtained by

$$\sigma = \left(\sum_{\text{events}} \frac{1}{\epsilon_i} \right) \frac{\sigma_a}{B} \frac{c}{[1-\exp(-\ell/\Lambda)]}$$

where σ_a is the absorption cross section per nucleus, $\Lambda[= A/(N_o \rho \sigma_a)]$ is the absorption length in the target, A is the atomic number, ρ is the target density, N_o is Avogadro's number, B is the beam incident upon the target, ℓ is the length of the target, ϵ is the acceptance at the spectrometer for each observed event and c contains corrections for phototube inefficiencies (1 per cent), downstream trackfinder inefficiencies (15 per cent) and second order corrections to upstream MWPC efficiencies (7 per cent). Typical pion and proton absorption cross sections[41] were used in order to obtain the absorption rate of the beam in the target. Table 1 shows the normalization and cuts information for the data. Errors in the cross sections which were not associated with statistics were typically about 10 per cent, and were mainly due to uncertainties in absolute acceptance and wire chamber efficiencies.

The acceptance-corrected mass plots from the ρ, π^+ and π^- data are shown in Figs. 32 to 34. In addition Fig. 35 shows the average weighting ($\langle\frac{1}{\varepsilon}\rangle$) per x_F bin for the data in the ρ-ω region. As can be seen, the average weight does not exceed 9.0 in any bin--another cross check on the acceptance calculation. As was explained in the Monte Carlo Section, the acceptance at low x_F was carefully checked, so that an insignificant portion of the data is weighted with large weights. As also explained in the Monte Carlo section, net shifts in the measured x_F, p_T or mass (relative to the input dimuon spectrum) did not visibly affect the weighting of the events.

Decay Backgrounds

The existence of the drift space between the target and the hadron absorber enabled secondary hadrons (mostly pions and kaons) to decay before absorption in the iron. Thus for some fraction of the target interactions, decay product muons will trigger the apparatus. As was discussed earlier, most such events will be rejected by the low-mass χ^2 test. The remaining signal can be easily subtracted. Since correlations between produced hadrons are small,[42] the like-sign signal ($\mu^+\mu^+ + \mu^-\mu^-$) will be equal to the opposite sign signal ($\mu^+\mu^-$). Monte Carlo studies using meson production and decay characteristics[43] show that the number of like-sign pairs observed in the "downstream" analysis is consistent with all such events having originated from pion and kaon decays. A mass plot of like-sign events superimposed on the opposite-sign events from the same data sample is shown in Fig. 36. As can be seen, the level of this background decreases with increasing effective mass. However, the opposite-sign sample also decreases in this region. Thus this decay contribution is most significant in the highest mass region. The like-sign to opposite-sign ratios as a function of mass are

Region	Mass	$(\mu^+\mu^+ + \mu^-\mu^-)/\mu^+\mu^-$
I	$0.21 < M \leq 0.45$ GeV/c	.054
II	$0.45 < M \leq 0.65$	.097
III	$0.65 < M \leq 0.93$	.043
IV	$0.93 < M \leq 1.13$	.074
V	$1.13 < M \leq 2.00$	.170

All of the resulting cross sections have been corrected for such decays by reducing the opposite-sign cross sections in each of the five mass regions by the like-sign contribution. No appreciable differences were observed between the pion and proton samples. Any possible background signal from a "prompt" single muon plus a decay muon will also appear in the like- and opposite-sign signals and will be subtracted away at the same time.

Secondary Production Check

One possible "background" to the desired spectrum is the production of dimuons from secondary interactions in the target. This source has been discussed in the Vertex Analysis Sections. A final check on this possible source can be made by taking the ratio of the number of events from the long target to those from the short target in each x_F bin. A ratio at low x_F higher than the ratio of high x_F would indicate the presence of secondary production in the target due to the lower incident energy for the second reaction. A plot of such ratios is shown in Fig. 37. No secondary production is apparent.

Fits to the Data

Shown in Figs. 38 and 39 are plots of the data binned in $E\frac{d\sigma}{dx_F}$ or $\frac{1}{p_T}\frac{d\sigma}{dp_T}$ versus x_F and p_T respectively for the ρ-ω mass region. The data are shown for the observed events for $0.07 \leq x_F \leq 0.97$ and for $0.0 < p_T \leq 3.0$ GeV/c. The errors shown are due to statistics and uncertainties in the absolute acceptance only. Cross sections, $\Delta\sigma_i$, given versus x_F or p_T interval (within a given x_F or p_T interval, 0.1 absolute or 0.2 GeV/c units wide respectively) are also given with their restricted errors in Tables 2-4.

Fits were made to the data again using the restricted errors discussed above. The p_T data was fit according to

$$\frac{1}{p_T}\ \frac{d\sigma}{dp_T} \alpha\ \exp(-bp_T)$$

and gave the fit parameter b for the data points with $p_T > 400$ MeV/c. A χ^2 quantity was minimized in fitting the parameter to the data and an error was calculated for b which was the change in b required to increase the value of the χ^2 by one. Because the dimuon data is lower near $p_T = 0.0$ relative to an otherwise exponential fit, the first two p_T points (corresponding to $p_T \leq 400$ GeV/c^2) were excluded from the fit. A more complex and less intuitively satisfying functional form would have been required to fit the data over the entire region. A slightly poorer fit to $\exp(-cp_T^2)$ could have been used, but the fit to the data at higher p_T would have suffered. The chi-squares per degrees of freedom for the fit are included in the table and the fits were reasonable.

Several fits to the x_F distributions were attempted. Fits of the forms

$$\frac{d\sigma}{dx_F} \alpha\ (1-x_F)^n$$

$$\frac{d\sigma}{dx_F} \alpha\ \exp(-dx_F) \quad \text{and}$$

$$E\ \frac{d\sigma}{dx_F} \alpha\ (1-x_F)^n$$

were tried but yield poor representation to the data. Both the $\frac{d\sigma}{dx_F}$ and the $E\frac{d\sigma}{dx_F}$ show a large cross section component at low x_F and hence do not accommodate the $(1-x_F)^n$ fits, which are convex near $x_F = 0$. In fact, in $\frac{d\sigma}{dx_F}$ even the exponential fit is much lower than the data at the x_F point nearest 0.0 ($\langle x_F \rangle = 0.12$) The net effect of the centered mass energy E in $E\frac{d\sigma}{dx_F}$ is to lower the low x_F points relative to the higher x_F entries. This factor allows a fit to be made of the form

$$E\ \frac{d\sigma}{dx_F}\ \alpha\ \exp(-cx_F).$$

This was by far the best of the four fits tried. The restricted errors were used for these fits and the χ^2/degree of freedom for this fit can be found in the cross section parametrization tables. In two mass regions, $0.45 < M \leq 0.65$ and $0.65 < M \leq 0.93$, the lowest entry $E\frac{d\sigma}{dx_F}\Big|_{<x_F> = .12}$ was significantly higher than the fit value. The care with which the low x_F cross section influences were checked in the Monte Carlo--for example, the amounts of all absorbing and scattering material in the apparatus was carefully accounted for--and the consistency checks imposed (see The Monte Carlo) indicate that the large low x_F cross section contributions are real. The $E\frac{d\sigma}{dx_F}$ cross sections, when plotted in rapidity (for the definition of rapidity, see Comparison of Data to Models) space, yield plots with no upturn at the lowest rapidity value measured, though such plots are not definitive in yielding total cross sections, as the extrapolation to $x_F = 0.0$ is large in rapidity space (over one unit out of about three in the forward direction). The reader is warned that the fits represent a parametrization of the data to aid in calculations, but the quality of the fits is not always sufficient to accurately represent all aspects of the physics. For that reason the binned cross sections are given separately in Table 2. Again, the errors on the parameters are calculated from an increase in the χ^2 by one. The errors do not reflect the goodness or poorness of the functional form of the fit to the data. The consistency of the increase in average p_T with increasing mass, regardless of the sources, helps to assure us that the continuum and resonance signals in the ρ and ϕ regions have similar distributions. There is no such assurance for the fits in x_F. An attempt was made to fit the $E\frac{d\sigma}{dx_F}$ distributions in the $0.45 \leq M \leq 0.93$ GeV/c^2 regions to two exponentials representing (at the ρ-ω , for example) continuum and resonance contributions. The results were not encouraging. In the end a single functional form was used

and the result is assumed to be approximately valid for each individual contribution.

The results of the two fits were combined to yield a representation of the form

$$E\frac{d\sigma^3}{dp^3} = A \exp(-bp_T) \exp(-cx_F).$$

The parameter A was normalized so that the fit, when numerically integrated over $0.0 \leq p_T \leq 3.0$ GeV/c and $0.07 \leq x_F < 0.97$, yielded the measured cross section in each mass interval.

The errors due to statistics and absolute acceptance were typically 6 per cent for most of the measured cross sections. The errors quoted for total measured cross sections are 12 per cent which also includes possible normalization errors.

Tables 5 through 9 show the measured ($0.07 \leq x_F \leq 0.97$) and estimated total ($0.00 \leq x_F$) cross sections for various mass intervals. Both cross sections per nucleus and per nucleon are shown. For masses below 0.93 GeV/c^2 the conversion factor used was $A^{\cdot 67}$, above 0.93 and below 1.13 GeV/c^2 the factor used was $A^{\cdot 75}$, and above 1.13 GeV/c^2 the conversion factor used was $A^{\cdot 85}$.[33] Two alternative assumptions were made to obtain the total cross sections. In the first case, the fit discussed above was used and the cross section was extrapolated exponentially in $E\frac{d\sigma}{dx_F}$ to $x_F = 0.0$ and numerically integrated. In the second case the cross section was extrapolated flat in $E\frac{d\sigma}{dx_F}$ to $x_F = 0.0$ from $x_F = 0.07$ and integrated. Thus the only difference between the two total cross sections is in the amount of cross section ascribed to the region $0.00 \leq x_F < 0.07$. The amount of error associated with the extrapolated cross sections is that of the errors for the measured cross sections plus an error associated with the small uncertainty in the fit parameters. Again the errors do not reflect the goodness or poorness of the functional form (exponential or flat in $E\frac{d\sigma}{dx}$) chosen. The total extrapolated cross section errors quoted are $\pm$ 15 per cent.

Relative Continuum and Resonance Contributions

The mass plots show strong peaks at about 780 MeV/c^2 and at about 1020 MeV/c^2, which can be attributed to ρ, ω, and ϕ meson decays. The ρ has a mass of 773 MeV/c^2 and the ω has a mass of 783 MeV/c^2, with respective full widths at half maximum of 152 MeV/c^2 and 10 MeV/c^2. Because the mass resolution is about 60 MeV/c^2 at 780 MeV/c^2, we cannot separate those peaks on the basis of the mass spectrum. The narrowness of the observed peak at 780 MeV/c^2 indicates that there is substantial ω production. We note also that there is a "continuum" below the peaks which falls rapidly with increasing mass. In order to extract cross sections for the ρ-ω peak and for the ϕ peak, an estimate of the continuum (the non-resonant contribution to the signal) must be made. Since the source mechanism of the bulk of the low-mass signal is not known--and hence no functional form for the low-mass signal is known--and since empirical fits to higher mass data using an exponential form are common, this method will be followed here (see Figs. 40 to 42).

Fits were made to the data using the region just below the ρ-ω (575 to 625 MeV/c^2) and the region just above the ϕ (1.125 to 1.20 GeV/c^2). The signal above the fit was thus attributed to the appropriate resonance. The parameters used all led to an exponential slope of about 4.9 c^2/MeV. The fractions of the signal in the appropriate mass intervals, as obtained from the empirical fit, are shown in the chart below.

Data Type	Mass Region (GeV/c^2)			
	0.65 to 0.93		0.93 to 1.13	
	$\rho+\omega$	cont.	ϕ	cont.
p	0.707	0.293	0.612	0.388
π^+	0.728	0.272	0.704	0.296
π^-	0.731	0.269	0.667	0.333

From the dimuon data of the ρ-ω peak (after continuum subtraction) we can obtain the relative ρ and ω contributions by assuming that the ρ and ω

are produced in equal amounts.[13] The $\mu^+\mu^-$ branching ratios are 4.3×10^{-5} and 7.6×10^{-5} for the ρ and ω respectively,[44] and thus 0.36 of the resonance signal is due to the ρ and 0.64 is due to the ω. For the ϕ we use a branching ratio of 2.5×10^{-4}.[44] Thus we obtain total observed cross sections of 15.3 mb, 15.3 mb and 996 μb per nucleus for the pC total cross sections, above $x_F = 0.07$, for the production of the ρ, ω and ϕ. Dimuon resonance and continuum cross sections are given in Tables 10-13.

As seen in the figures, a sizeable continuum remains after the resonances are taken into account. We soon address the question of possible sources of the continuum signal.

General Trends of the Data

Before examining in detail possible sources of low mass dimuons we note some general features of the low mass distributions.

First, we note that, independent of the beam particle type, transverse momentum distributions are remarkably similar. The transverse momentum fit parameters are,within errors, equal for the proton and the charged pion beams (see Fig. 43). In the lowest mass regions the momentum distributions are very steep. The distributions then widen with increasing mass on up to the highest mass interval measured. This phenomenon has been observed as well in the higher mass data from this experiment.[33] Overlapping the mass regions studied, we note that this trend extends from $M = 0.2$ GeV/c^2 to 3.5 GeV/c^2.

The longitudinal momentum distributions show strong differences between the proton and pion induced events. The pion induced data fall off more slowly as a function of x_F than the proton data. In fact, we can see that the proton x_F parameter is about 4 units greater, in corresponding mass regions, than the pion parameter (see Fig. 44).

The integrated cross sections for several x_F regions are given in Tables

8-11. While the resonance cross sections per nucleus are roughly equal, the cross sections per nucleon for $x_F > 0.15$ are lower for the 225 GeV/c carbon data than for the 150 GeV/c beryllium data. Looking at the continuum tables we see that the cross sections are uniformly lower for the 225 GeV/c data, whether given per nucleus or per nucleon.

Bethe-Heitler Process

Muon pairs can be produced by photons from decays of secondary neutral pions interacting with a nucleus, as in Fig. 45(a). This is Bethe-Heitler production. The total effective Bethe-Heitler cross section can be expressed by

$$\sigma_{eff} = 2\langle n_\pi \rangle \eta \tfrac{1}{2}[1-\exp(-\ell/\Lambda)]\ \sigma_{BH}$$

where $\langle n_\pi \rangle$ is the average number of neutral pions produced per collision,

η is the fraction of all neutral pions producing a photon with energy great enough to produce a dimuon with x_F 0.07,

Λ is the radiation length in dense carbon (35.4 cm)

ℓ is the length of the target (12.5 or 7.5 cm), and

σ_{BH} is the cross section for creating a muon pair from a photon.

The factor of ½ is inserted because an average photon will only "see" the remaining half of the target. The factor of 2 accounts for 2 photons per pion. The number of pions was determined from the average of yields of positive and negative pions as fit to 225 GeV/c from other data.[45] The number used is 3.16 pions per interaction. In practice, η was determined by feeding the pion production spectrum[46] into a Monte Carlo program simulating neutral pion decay and requiring that p_z for the photon be greater than 16.4 GeV/c. Thus, η = 0.0897. The full photon spectrum was also fed into another program that integrated the Bethe-Heitler dimuon production cross section.[47] The result was that σ_{BH} = 3.8 μb for carbon nuclei and 60.4 mb for iron. As explained earlier,

the 55 cm chamber provided a rejection against iron produced pairs appearing in the data by a factor of 17. We thus obtain 322 nb and 300 nb for the Bethe-Heitler cross section expected in the long target data (negative beam) for the carbon and iron produced pairs, respectively. We obtain 257 nb and 240 nb for the combined length data (positive beam). This is to be compared to cross sections of about 4800 and 4600 nb for the long and combined target data respectively. Thus about 13 per cent and 11 per cent of the lowest mass region cross sections can be attributed to Bethe-Heitler production in the long target and the combined target data respectively. Thus while this signal is not insignificant, by far the greatest portion of the low-mass signal cannot be attributed to Bethe-Heitler production.

Omega Dalitz Decays

If the branching ratio for $\omega \to \pi^{\circ}\mu\mu$ is not exactly zero, we expect that the data will include a dimuon signal due to the two muons from this decay. We can estimate the contribution using the predicted branching ratio and our own measurement of the inclusive ω^{o} production cross section.

We inserted the ω production cross sections as a function of x_F and p_T into the standard Monte Carlo. The ω was generated with production characteristics, observed for the resonance peaks and was allowed to decay to a pion and two muons via a vector meson dominance diagram, shown in Fig. 45(b), with a branching ratio of 8×10^{-5}.[24] An $x_F \geq 0.07$ cut was then applied to the Dalitz muon pairs. The resulting dimuon cross sections were 752 nb, 1030 nb and 929 nb for the proton, positive pion and negative pion data respectively. The reconstructed dimuon mass distribution and relative size to the entire dimuon signal is shown in Fig. 46. We thus see that this decay, while contributing a non-negligible signal to the data (assuming the calculated branching ratio) leaves the major portion of the signal as yet unaccounted for.

Eta Decays

Another possible source of signal exists--that of the eta Dalitz decay. The direct eta decay $\eta \rightarrow \mu\mu$ has a branching ratio of $(2.2 \pm 0.8) \times 10^{-5}$,[19-21] while the $\eta \rightarrow \mu^+\mu^-\gamma$ decay is expected to have a branching ratio of 3×10^{-4}.[24] Thus the dimuon signal from the eta can be significant even in the absence of a distinguishable resonance signal at the eta mass. We can estimate the eta production cross section if we assume that all of the remaining dimuon signal in the region $0.25 \leq M \leq 0.35$ MeV/c (after subtracting off the omega Dalitz and Bethe-Heitler process contributions) originated with the eta Dalitz decay. In order to obtain the mass distribution of the eta Dalitz muons, we used the production characteristics of mass interval II (the eta region) and decay matrix elements[48] appropriate to the eta [see Fig. 45(c)]. The decays were then Monte Carloed in the same manner as that described for the omega Dalitz decays. The cross sections obtained follow:

	Maximum Eta Production Cross Sections			
	$x_F \geq 0.07$		$x_F \geq 0.0$ (per nucleus)	
	per nucleus	per nucleon ($A^{2/3}$)	flat extrapolation	exponential extrapolation
Proton	17 mb	3.3 mb	31 mb	45 mb
π^+	15 mb	2.8 mb	26 mb	32 mb
π^-	14 mb	2.7 mb	24 mb	28 mb

(The differences between beam types are due to slightly different x_F and p_T distributions from mass region II.) This is to be compared to a similarly estimated 1 mb (for $x_F > 0.3$ and $p_{beam} = 16$ GeV/c) obtained at SLAC[49] in a p-p dimuon experiment. The resulting mass distribution and the resulting $\eta \rightarrow \mu\mu$ mass distribution (using BR = 2.2×10^{-5}) are shown in Fig. 46, along with the other low-mass contributions. Thus it can be seen that the estimated branching ratio and contribution assumption lead to not unreasonable estimates for the eta cross section, although the overall shapes of the estimated and measured signals are not wholly in agreement.

We may make an alternative estimate for the eta production cross section. Using the previously measured ratio of 0.34 for the ratio of the production cross section of the eta to that of the rho[22] and using the branching ratios already discussed, the rho cross section measured in this experiment leads to a proton induced cross section for the eta of 5.2 mb per nucleus for $x_{F_\eta} \geq 0.07$ (5.9 and 5.3 mb for π^+ and π^-) and an eta Dalitz cross section of 1.0 μb per nucleus for $x_{F_{\mu\mu}} \geq 0.07$ (0.99 and 0.89 μb for π^+ and π^-). This estimate leads to the distribution shown in Fig. 47.

We note that this appears by the shapes of the spectrum to be a more reasonable estimate of the contribution of the Dalitz decay pairs to the low mass signal as determined from the spectra shapes. It should be stressed that the total of these signals are still dependent upon (1) the calculated omega Dalitz decay branching ratio and (2) the eta Dalitz decay branching ratio. We also note that the signals from both of these processes drop sharply at about 500 MeV whereas the continuum signal does not exhibit a sudden break in this region. It would thus not be surprising if one or both of the contributions were somewhat smaller than obtained from the calculated branching ratios.

The cross section obtained for these calculated contributions (η Dalitz, ω Dalitz, $\eta \rightarrow \mu\mu$, and Bethe-Heitler process pairs) is 2.36 μb versus about 6.2 μb for the data below the ρ-ω regions, leaving about 62 per cent of the signal in the two lowest mass bins unexplained by conventional sources.

The transverse momentum distribution of the lowest mass region can be compared to that of the Monte Carloed eta Dalitz pairs. Fig. 48 shows the $\frac{1}{p_T}\frac{d\sigma}{dp_T}$ distributions for the data with $0.21 < M < 0.45$ GeV/c^2 and for the Monte Carloed distribution. The Monte Carlo contribution is normalized to give the fraction of the 1.0 μb cross section which would fall into the lowest mass

region (about 0.95). We note that the p_T distribution of the Dalitz pairs is much broader than the data. The assumption of even 20 per cent of the lowest mass signal originating from the eta Dalitz decay is thus inconsistent with the data.

Comparison of the Data to Models

As we have seen, even after we subtract the omega Dalitz decay pairs, the Bethe-Heitler produced pairs, the generous eta Dalitz decay pairs estimate and the pairs from the eta (direct) dimuon decay, there is still a sizeable low mass dimuon signal the origin of which is still unexplained. In this section we briefly compare the remaining signal with two of the most promising explanations of dimuon production through electromagnetic processes: the constituent bremsstrahlung mechanism,[28,50] and an enhanced Drell-Yan mechanism.[26]

The first of the bremsstrahlung models,[28] used for its estimate of the dimuon production cross section a minimum effective mass of 1.2 GeV/c^2 obtained from an earlier experiment.[14] The estimate of the dimuon contribution made in the paper was thus 0.20 nb--an extremely small contribution when compared to the non-resonant dimuon signal of several μb measured in this experiment. If we recalculate the contribution by setting the minimum mass at 0.21 MeV/c^2 (i.e., the lowest possible mass of the two muons), we obtain 14 nb. This is still much smaller than the observed signal.

A later paper[50] attempted to explain the large single lepton signal (discussed in the Introduction) as the result of a parton bremsstrahlung mechanism. Unfortunately, there is little from the model that can be compared to experiment, as the photon spectrum is itself argued from a modified observed pion spectrum and it is normalized to observed muon spectra. The model additionally depends upon a reinterpretation of several experiments in order to explain the model's prediction that electrons are produced more copiously than

muons by a factor of about 2-3. The experiments observed e/π ratios consistent with μ/π ratios observed by others.

In the bremsstrahlung model, the mass distribution falls as 1/m for the masses presented here. Fig. 49 shows such a spectrum compared to the measured spectrum with the bremsstrahlung spectrum normalized to the data in a region just above the ϕ. The contributions to the low-mass spectrum discussed above are given as well. It can be readily seen that this bremsstrahlung spectrum is insufficient to explain more than a small portion of the low mass signal.

The other popular model with which the data can be compared is the Drell-Yan model (or a more recent model[51] which yields the same results for masses below about 5 GeV/c^2). As discussed in the Introduction, the model yields a dimuon prediction that then fails to account for the observed μ/π ratio. Following Bjorken and Weisberg, we estimate that at 90° in the center of mass system $\frac{d\sigma}{dy} = \left(\frac{1}{3}\right)^a \frac{1\text{GeV}^2}{Q^2_{\text{min}}}$ $(7 \times 10^{-33}$ cm) with a = 0 or 1 depending on whether we believe in "color"--a concept used to explain quark confinement, to symmetrize and antisymmetrize hadron wave functions and to reduce cross sections--or not. The rapidity variable y is a measure of the longitudinal momentum of the muon pair and is defined by

$$y = \tfrac{1}{2} \ell n \frac{E + p}{E - p}$$

and is related to x_F by

$$x_F = \frac{2\sqrt{m^2 + p_T^2}}{\sqrt{s}} \sinh(y)_{cm}$$

(at high y, $y \simeq \ell n \frac{x_F \sqrt{s}}{\sqrt{m^2 + p_T^2}}$). Thus at large y, $\frac{d\sigma}{dy} = E\frac{d\sigma}{dx_F}\frac{2}{\sqrt{s}}$. If we let $Q_{\text{min}} \simeq 0.26$ as indicated from the mass plots above, we obtain a naive prediction of $\frac{d\sigma}{dy} \simeq \left(\frac{1}{3}\right)^a 1 \times 10^{-31}$. This rough calculation can be compared to the data. If we impose a rapidity plateau on the data and extrapolate flat to $x_F = 0.0$ from $x_F = 0.07$, after subtracting the signal for the Dalitz

decays, the Bethe-Heitler produced pairs, and the direct resonance contributions (ρ, ω, ϕ, and the non-maximized η yield shown in Fig. 47) we obtain $E\frac{d\sigma}{dx_F} = 4.5 \times 10^{-30}$ cm^{2}GeV/c^2 or $\frac{d\sigma}{dy} = 4.4 \times 10^{-30}$ cm^2. Thus we see that this simple estimate is too small by about a factor of 44, even neglecting color. However, it should be pointed out that those who introduced the theory emphasized that the calculations were only applicable down to a mass of about 1 GeV/c^2. This was required because it had to be assumed that the protons in the colliding particles were free during the collision--in other words the impulse approximation was valid. It is true as well that the quark (proton) distributions are not well known at low x (the x_F of the protons previous to the collision) because the number of "wee" (low momentum) protons is not well known. Thus the two factors work against one another and one doesn't know what the net effect will be.

An attempt was made, however, to estimate a factor which would make the cross section larger. Bjorken and Weisberg pointed out that the quarks produced in a Hadronic reaction will themselves contribute to the available parton-anti-parton annihilation pairs. This they calculated to yield a factor of about 25 "improvement" to the cross sections. This would bring the crude estimate of the cross section to $\frac{d\sigma}{dy} \simeq \left(\frac{1}{3}\right)^a 2.6 \times 10^{-30}$ cm^2 (compared to the estimate of 4.4×10^{-30} cm^2), and we see that the estimate is within a factor of 1.7 of the experimentally estimated value if one does not believe in color and a factor of 5 if one does.

The Single Muon Contribution

As discussed in the Introduction, the large single muon signal from hadron collisions observed prior to this experiment was part of the motivation for this experiment. By directly measuring the dimuon signal from hadronic

reactions we could determine a single muon yield due to the production of muon pairs. This we now do.

The single muon contribution due to proton-beryllium reactions at 150 GeV/c has already been reported by this experiment.[52] The result was reported for both the contribution to $E\frac{d^3\sigma}{dp^3}$ at $x_F = 0.0$ and for $\frac{d\sigma}{dx_F}$ from $x_F = 0.1$ to $x_F = 0.6$ and was compared to experiments measuring the single muon to pion ratio in these regions by using inclusive pion production data. The result for $\frac{d\sigma}{dx_F}$ (integrated over $p_T < 600$ MeV/c) is just that measured by the experiment and thus stands alone. However, the contribution at $x_F = 0.0$ depends somewhat upon the extrapolatio of the dimuon data at $x_F \geq 0.15$ to $x_F = 0.0$. The method used in the earlier calculation was to use a fit of the data to the form

$$\frac{1}{p_T}\frac{d^2\sigma}{dx_F dp_T} = A(1-x_F)^c \exp(-bp_T)$$

It was pointed out in the paper that the fit in x_F yielded an integrated cross section within 10 per cent that obtained by assuming that $E\frac{d\sigma}{dx_F}$ is flat for $x_F < 0.15$ (or equivalently, that a rapidity plateau is imposed). However, in the 225 GeV/c data no such rapidity plateau is seen down to $x_F = 0.07$. The single muon contribution at low x_F can only be increased. We thus make a new calculation of the dimuon contribution to the single muon yield by using the results of the newer measurement where the dimuon is measured closer to $x_F = 0.0$ ($x_F \geq 0.07$).

The contribution to the single muon yield was calculated independently for each of the resonances (ρ, ω, and ϕ) and for each of the mass regions of the continuum signal measured by the low mass experiment. In addition, the single muon contribution of the dimuon decay of the ψ is included. The ψ cross section and its x_F and p_T dependence is taken from the higher mass measurement by our research group.[33] The relative ρ and ω contributions were separated as discussed above. All resonances were assigned to their nominal mass values

with the exception of the ρ, which was assigned a Gaussian distribution of 150 MeV/c^2 full width at half maximum centered at its nominal mass value. The continuum signal was generated in mass according to

$$\frac{d\sigma}{dM} \alpha \exp(-5M)$$

within each of the five mass regions, in agreement with the parametrization of the data discussed earlier.

A Monte Carlo program then generated events in x_F and p_T weighted in accordance to the measured cross sections per bin (x_F and p_T fits were not used) and each event was assigned a weight in accordance with the Lorentz-invariant production cross section for the muons. The dimuons were allowed to decay isotropically if their rest frame, and the muons of a given charge were binned in an x_F and p_T grid and weighted as above. The resulting cross sections as a function of p_T varied by less than 20 per cent depending upon whether the decay was isotropic or varied as $1 + \cos^2\theta^*$. As explained elsewhere[33] any decay polarization was small $[1 + (0.02 \pm 0.07)\cos^2\theta^*]$ at the ρ-ω region as determined by a measurement by this group which involved higher statistics than was possible with the low mass analysis.

In all of the following the single muon yields were compared to pion yields from other experiments. While the single muon yields were obtained from a carbon target, the pion yields were obtained from beryllium targets. Hence all single muon yields were weighted to beryllium yields by assuming a dependence of $A^{2/3}$ below the ϕ, $A^{.75}$ for masses between 0.93 GeV/c^2 and 1.13 GeV/c^2, $A^{.85}$ from a mass of 1.13 GeV/c^2 to 2.0 GeV/c^2 and A at the ψ mass. Thus the cross sections are weighted by factors of 0.83 at the lowest masses to 0.75 at the highest.

The resulting dimuon distribution in the forward direction as a function of x_F and integrated over all $p_T < 600$ MeV/c is shown in Fig. 50. Both the vector

meson contribution and the total contribution are given. The pion yield is that obtained from an experiment done at 24 GeV/c[53] and the comparison assumes Feyneman scaling. This scaled experiment agrees to within 20 per cent with the less complete results of a measurement made at 200 and 300 GeV/c. The more rapid fall off of the single muon yield than the pion yield can be attributed, in large part, to the steep x_F distribution of the dimuon continuum at low mass. The resulting μ^-/π^- ratio as a function of x_F can be seen in Fig. 51 with the vector meson contribution shown along with the total contribution. The results of experiments directly measuring the single μ yield are superimposed on the figure.[54-56] As can be seen in the figure the dimuon contribution to the single muon yield is in reasonable agreement with the direct single muon results. We thus note that the single muons of $x_F \gtrsim 0.1$ are produced from dimuons arising from decays other than ρ, ω, ϕ, and ψ decays, a result in agreement with a low resolution experiment[56] which suggested that the "bulk" of single muons originate from electromagnetic interactions. We find, in addition, that most single muons from non-resonant pairs came from sources with invariant masses smaller than 600 MeV/c^2, a result in disagreement with Ref. 56.

We emphasize that the above results follow directly from the measured dimuon signal and are not dependent upon extrapolations or fits.

Since the p_T dependence of single muon productions had been investigated primarily at $x_F = 0.0$, an extrapolation of our dimuon data to $x_F = 0.0$ was required to compare to those single muon experiments. Before discussing the extrapolation to zero, we will look at the sensitivity of the single muon p_T spectrum to the input spectrum of the dimuon. The dimuon p_T is, on the average, only slightly larger than the p_T of a daughter single muon when the single's p_T is significantly larger than the mass of the dimuon. For example,

single muons with p_T = 1.0 GeV, produced at 90° and from a dimuon of 780 MeV/c^2 arose from dimuons with a mean p_T of 1.2 GeV/c. The result is that single muons produced at moderate p_T (less than 2.5 GeV/c) arise prodominantly from dimuons with p_T in the measurable range. This combined with the rapidly falling p_T spectrum, insures that the deduced single muon spectrum is an accurate representation of the data for moderate p_T.

Since the data is still rising in $E\frac{d\sigma}{dx_F}$ at the lowest x_F point measured, a single simple extrapolation to x_F = 0.0 was not possible. Thus two alternative extrapolations were used. In the first method the differential cross section $E\frac{d\sigma}{dx_F}$ was extrapolated flat from the lowest measured x_F bin (with $\langle x_F \rangle$ = 0.12) to x_F = 0.0. Since $E\frac{d\sigma}{dx_F} \alpha \frac{d\sigma}{dy}$ this is equivalent to imposing a rapidity plateau in the cross section starting at x_F = 0.07. As the data are still rising rapidly at this point this may provide a kind of lower bound to the dimuon data at x_F = 0.0. The second method used the exponential fit obtained in the Fits to the Data section to extrapolate $E\frac{d\sigma}{dx_F}$ to x_F = 0.0 from the measured region.

The resulting spectra can be seen in Fig. 52. Shown also is the pion dependence,[57] measured at 300 GeV/c, and scaled downwards (by about 10 per cent) as a function of p_T, using the energy dependence as a function of p_T measured in the same experiment. The ratio of the two yields can be seen in Fig. 53. Superimposed on the calculated yield are the results of single muon experiments.[58-60,63] As no difference in μ^+/π^+ and μ^-/π^- ratios has been observed in single muon experiments, measurements of both ratios are included. We see that the extrapolation which is exponential in $E\frac{d\sigma}{dx_F}$ yields a single muon ratio about a factor of two higher than the extrapolation which is flat in $E\frac{d\sigma}{dx_F}$, in accordance with the dimuon cross section differences between the exponential and flat extrapolation in the lowest mass region studied.

Thus we see that muon pairs contribute a large fraction of the muons observed by single muon experiments, both in the forward hemisphere where no assumptions are necessary to directly deduce the singles contribution and at low x_F where a "low" estimate yields a reasonable agreement with direct single muon experiments.

The question of whether charmed particles (or other heavy particles which decay leptonically and are produced in pairs) contribute heavily to the dimuon signal can now be addressed. Assuming that such a particle decays about 10 per cent of the time to products including a muon, the probability for both particles decaying to muons is suppressed by an additional factor of ten. From the two μ/π figures we see that any muonic signal left after subtracting off the dimuon contribution is small. If we assume that half of the di-μ continuum contribution is due to such charmed decays, we obtain a single muon production rate from "non-dimuon" events (for muons of a given sign) nine times greater than that from the selected continuum events. The resulting single muon signal (the single muon signal from vector mesons + the single muon signal from "continuum" events times 9.0/2) is clearly higher than that allowed by the single muon components. We additionally note that the dimuon signal from two heavy particles would yield reconstructed masses and average transverse momentum higher than the observed continuum masses and transverse momenta. The continuum signal at low masse remains unexplained.

CHAPTER V

SUMMARY

We have performed a high resolution experiment which measured the low mass dimuon signal produced in hadronic interactions over a wide range in x_F and p_T, using a large acceptance spectrometer. The experiment has yielded the dimuon cross sections as a function of mass and as functions of x_F and p_T. A "continuum" has been observed under the resonance signals. Resonance cross sections have been extracted and the continuum contribution has also been estimated. Various contributions to the continuum signal have been estimated and the contributions considered fail to account for more than 60 per cent of the signal in the lowest mass region. The most promising models attempting to predict the low mass signal either (1) fail to account for the data or (2) are insufficiently precise at this stage to predict the mass distribution of the low mass signal and to predict the large cross section observed. The dimuon contribution to the single muon's signal has been calculated and is in reasonable agreement with the exciting large signal observed in single muon experiments. Thus the question of the origin of single muons is being replaced by another equally intriguing question. What is the source of low mass dimuons?

APPENDIX A

UPSTREAM MWPCs

Construction of the 55 cm, 80 cm and 30 cm MWPCs

The 55 cm and 80 cm chambers were of the same geometry, the only significant difference being the sizes of the active areas. Fig. 54 shows the 80 cm chamber, and Fig. 55 shows the 30 cm chambers. The 30 cm chambers were of different geometry but construction, testing and use (physically) were the same as for the 55 cm and 80 cm chambers and interplane spacing (i.e., between anode and cathode planes) was 4.8 mm (3/16").

Wire spacing was 1.59 mm (1/16"). The anode wires were 0.8 mil diameter gold plated tungsten. Cathode wires were 4 mil diameter silver plated copper-beryllium. An expanded view of the chambers is shown in Figs. 56 and 57.

The x and y planes were orthogonal. The u and v planes were orthogonal to each other but were rotated 45° with respect to the x and y planes. If we call each assembly module a frame, then the five frames shown in Fig. 56 consisted of wire planes as follows:

Frame 1	Cathode plane and x plane
Frame 2	Cathode plane and u plane
Frame 3	Cathode plane and y plane
Frame 4	Cathode plane and v plane
Frame 5	Cathode plane only

An exploded drawing for the 30 cm chambers' three planes can be seen in Fig. 58.

The cathode planes and anode planes were mounted on common frames so that (1) there would be fewer frames, hence the geometry would be better defined and the frame would be more rigid, and (2) the chambers would be very compact, so that x, y, u, and v information would be obtained from essentially the same z position; this was important in the pattern recognition analysis.

Wires were wound by machine on a drum and connected by epoxy at the proper distances to G10 strips. The G10 strips (and hence wires) were later stretched across the G10 frames and epoxied in place. The anode wires were stretched with a force of 6.8×10^4 dynes. The cathode wires were stretched with 7.1×10^6 dynes. When wires broke and had to be replaced, new wires were replaced with equal tension. Wires were held in place by epoxy.[61]

The G10 frames were constructed of 8 slats [4 each layer, two layers deep, each layer being 4.76 mm (3/16") thick]. Slats were glued with epoxy. All mating surfaces were measured carefully with a micrometer and shimmed (with tape) or filed carefully to ± 76 μm (3 mils) of the nominal thickness. The dimensions were carefully adjusted, since at operating voltage, 25 μm (1 mil) in interplane spacing was equal to 20V potential difference. Thus the fields within the chambers were kept uniform to equilize efficiencies of all portions of the chamber. On the surfaces where a mother board and hence solder connections were present, a lucite strip replaced the G10. Lucite was used in these locations because the strips had to be thin and lucite of the proper dimensions was easier to work with.

All surfaces were checked several times that there were no non-machined surfaces touching inside (e.g., solder joints could not touch a neighboring frame, glue surfaces could not touch a neighboring frame); for any such matings unforeseen forces could have distorted the geometry within the chambers. The anode wires fed through a glue ridge onto an etched, copper surfaced G10

"mother board." The mother board held two amplifier cards every 2.54 cm of its length. Each amplifier card thus received the signal from eight wires and passed along a logical signal output. The amplifier cards operated on +5.V - 6.V + 12.V (and ground) - the -6.V and +12.V connections were made at both ends of all mother boards, and the +5.V and ground wires were both brought in at each end of the mother board and connected to a special bus line--double sided copper plated G10 2.5 cm wide--which was connected physically and electrically to the mother board. This bus was necessary to insure a low resistance line to the cards--each card used 0.245 A at +5 volts, 45 mA at +12 V, 30 mA at -6V. Voltages were adjusted on-site and prior to testing, to -6.0, +12.0, and +5.0 volts at the cards.

The chambers were enclosed within a frame made from 6063-T52 rectangular extruded aluminum tubing (see Fig. 59). Gas was fed in from the top edge of one-half of the frame and was exhausted through the bottom edge of the other half. The gas manifold was made of lucite and had uniformly spaced entrances (into chamber) and exits (from chamber) to insure laminar flow. The window on the downstream side of the chamber was made of aluminized mylar to discourage build-up of static charge on the window. However, the window on the upstream side of the chamber was made of clear mylar. This window was of immeasurable help in allowing visual inspection of the chamber during all stages of its operation and assembly.

The solder at the locations where the anode wires fed into the mother boards was somewhat rough in spite of care taken not to leave solder points from which discharges could originate. As a result, these surfaces were epoxied over once loose wire ends and shorts between wires were carefully checked. The unconnected (severed) ends of both anode and cathode wires were epoxied over after similar checking.

In spite of geometry precautions, it was found that the aluminum frames were not sufficiently sturdy. As a result, sturdy, aluminum C beams were incorporated into the aluminum frame on three sides of each half (see photograph). (The fourth had to be free so the hadron shield could be rolled in and out for alignment checks.) After this addition no more distortion problems existed.

Surrounding all the mother boards and cards was aluminum housing which served as a conduit for cooling by air blown by box fans and served to shield the cards from electronic noise. All shielding, framing, cards and cabling were carefully grounded. No cross talk between cards was observed. For each 55 cm and 80 cm plane and for each 30 cm chamber, a 1 MΩ resistor was placed in series with the cathode wires on the high voltage line. This resistor served as protection against a short through the chamber. In case of a discharge no wires would burn out. At the highest beam intensity the voltage drop across the resistor was about 150V.

Chamber Readout

Eight adjacent wires fed into an amplifier card (see Figs. 60 and 61). Each input was amplified and the resulting signal triggered a one-shot (a monostable multivibrator). The one-shot was timed to last 450 nsec and the pulse was differentiated. A coincidence between the trailing edge of this differentiated signal and the load pulse supplied by the fast electronics then caused a bit to be loaded into the shift register which was read out by the scanner (located in the Portacamp) and the coupler (on the chamber). The scanner sent clock pulses to the chambers upon command and then read back these clock pulses, along with the bits associated with the struck wires in the chamber. The scanner-coupler readout system is described in more detail elsewhere.[39]

Cleaning and Conditioning

Every chamber builder has a favorite method for cleaning wires and this one is no different, though it will be readily admitted that there are no clearly superior methods known to this builder. An adequate method is to clean the wires with a series of cleaners including methanol, ethanol, acetone and water. During the building, each of these was able to clean off some impurity that none of the others could remove. The liquid was applied with a small brush (preferably one which itself does not dissolve in the liquid). Backlighting provided by a slide projector in a dark room is most helpful in locating dirt on the wires. The environment had to be kept dust free, while cleaning, and all cleaning had to be done rapidly, as any dust attaching itself to the wires would necessitate another cleaning.

After a couple of brush cleanings, another cleaning followed, this time with an acetone spray. The spray pressure was supplied by nitrogen gas, and both frame and wires were cleaned. A similar spray cleaning with water followed this application. These cleanings allowed for a rapid final cleaning and all frames and wires were immediately covered upon completion of the spray.

Once the chamber was sealed, some burning-off was necessary. This consisted of slowly raising the voltage on the wires, either in air or in chamber gas. Very small dust particles would burn off very slowly by this process. This process (of slowly raising the voltage) could last about a day. A speck seen to glow longer than usual had to be removed by brush. The chamber, if extremely clean, could be raised to about -3900 V in gas, or -4100 V in air before a general glow set in. (The cathode wires were raised; anodes remained near ground.) By observing the chamber in an extremely dark room after being dark adapted, glowing spots or discharges (indicating dirt), a general glow in a specific area (indicating non-uniform geometry), or specific glowing wires

(indicating poor electronic connection to the amplifier) could be seen.

Reversing the polarity of the voltage on the wires was tried on one of the small chambers. A voltage of +2.8 kV was applied to the cathode wires for about 5 secs (through a 5 MΩ limiting resistor) resulting in a current of about 1 μA. This had a definite adverse effect on the chamber; high erratic currents were observed afterward. Voltage reversal was not tried again. Cleaning followed.

A discharge problem not related to cleaning was encountered on the V plane. The V plane was unique in that it had an edge where anode wires and cathode wires entered the G10 edge in back of one another; on the other planes cathode wires and anode wires entered a different edge of the G10 frame. This discharge, apparently caused by high gradients in the region of the dielectric bounded by the different wires was cured by backing the cathode wires by a kynar covered wire epoxied to the edge and allowed to float at cathode potential. This allowed for a smoother field near the edge and no further discharges resulted.

Gas Mixture

The gas used in the experiment was a mixture of argon (80 per cent), freon (0.4 per cent) and CO_2 (20 per cent). The so-called super magic gas mixture[62] was tried but found unsatisfactory--wires soon were coated with various residues which caused discharges until cleaned. The gas was then switched.

General Electric RTV 21[63] was used to seal the chamber. Because some mother boards were close to one another (back to back), sealing in the space between was a problem. Air leaks showed up in the testing; the plane efficiency decreased with increasing on-time of the cooling fans. Extra RTV had to be applied, leaks being found by use of a leak detector.

Dark Currents

With proper cleaning, dark currents within the chamber were kept to less than 20 nA with no source applied at -3700 V. A graph of dark current versus voltage with no source is shown in Fig. 62.

Noise Suppression

Soon after the chamber was in operation, noise was observed along with real particle hits in the chamber. (Wire hits were observed even with no H.V. on.) This was due to the amplifiers picking up the load pulse signal and sending along a very weak signal to the one-shots. The one-shot would sense the incoming signal but instead of firing for its 450 nsec duration, it would start to fire and then "back down" immediately, the result was a small positive pulse of a couple nsec duration. The differentiated signal from this short pulse, however (out of the capacitor following the one-shot) was large enough to be loaded into the shift register chip (see Fig. 63). This was cured by connecting a wire to the load pulse and stringing it (it was insulated) over the mother board leads to the amplifiers (see Fig. 64); the load pulse and the amplifier leads were thus (indirectly) coupled. Thus when a load pulse was sent, all one-shots that had not fired some 400 nsec before would now fire properly and the differentiated trailing edge was well out of time of the load pulse. No further noise was observed (see Fig. 65).

Support Wires

Since all of the anode wires were long, and the tension on the fragile wires was low, electrostatic repulsion between the wires could have been sufficient to separate them. The resulting non-planarity would have distorted the field inside. In order to avoid this support wires were installed in the 55 and 80 cm chambers. The support wires were locates well away from the beam

center but far enough from the edges to serve usefully. Support wires were attached to the anode wires by small drops of Glyptal;[64] cathode wires were under greater tension and hence did not require support wires. Prior to assembly all anode wire connections to support wires were checked. This was especially important as acetone, one of the cleaning fluids, dissolved Glyptal. Using very small scintillators as probes, the efficiency of the plane in the region of the support wires was observed. The efficiency plateaued at about 95 per cent with -1100V applied to the support wires (in addition to the normal cathode plane voltage). This setting was used during the data taking.

Checks

Clock and load pulses were regenerated at the chamber to insure sharp, strong signals. In addition, small delay cables were added in appropriate locations within the chamber so that all pulses reached all cards simultaneously. This allowed shortening of the load pulse while still insuring uniform efficiency from all planes. (Load pulse was eventually set to a safe 70 ns.) All cards were carefully timed by the same person to assure uniformity, and cards that showed drift in timing as a function of temperature had their one-shots replaced. By placing a radioactive source far away from the chamber (about 5 ft) and triggering on a small scintillator near the source, a raw illumination histogram of the chamber could be made in a couple of hours. This served to locate rapidly any dead wire within the chamber.

Extensive tests on plane efficiency as a function of position within the plane, voltage, time the cooling fans had been left on, gas flow, load pulse width, and delay time (the total length of time between passage of a particle and the receipt of the load pulse on the cards) were carried out on a PDP 11/20 prior to installation at Fermilab. Noise levels and wire hit spreads were also recorded. Figs. 65 and 66 display the results of some of these tests. Ramping

(increasing and decreasing the voltage between beam spills) the HV was also studied; ramping times appropriate to chamber size (capacitance) were chosen.

An annoying problem was discovered during the final portion of the testing (and late enough before the low mass run that the electronics could not be changed). In employing the illumination test described above, spiking in the raw numbers of hits versus wire number was observed (with a period of eight wires). After much hunting, the culprit was found; the plated lands on the cards prior to the amplifiers (and grounding resistors) were of different length. The land for the eighth wire on the card (at the connector) was opposite that for the first wire, the seventh was opposite the second, and so forth. However, the amplifier for the first wire required the longest lead from the connector, the eighth the shortest. Hence, there was a very small uneven capacitive coupling between wires #1 and #8, less between #2 and #7, etc. Thus, a signal on one wire could generate a very small signal on its opposite wire, and hence, wires could show hits where there were no hits. This was a problem on the few per cent level and because of the wire sorting (the inter-plane hit correlation done during the analysis) posed no problem. But it is a problem that could have had an effect if a wire hit correlation requirement were not present in the analysis. It is an effect that could be helped by an improvement on the plateauing characteristics (desirable for other reasons as well), and by changing the layout of the card.

Performance During the Run

During the run, the efficiencies of the chambers were closely monitored through both the cathode current and on-line checks of the efficiency. During the low mass run the beam flux was kept below 10^6 particles/spill to minimize loss of plane efficiency due to one-shot dead time and IR voltage loss across

the limiting resistor. This maintained an efficiency of about 0.85 per track for each plane. A special trigger, started by B.Vμ (see the Fast Electronics section) allowed periodic tests of the chamber efficiencies. This was used to check the efficiency versus voltage, efficiency versus beam intensity and to check that the timing of the load pulse had not changed. The most upstream (30 cm) chamber developed high currents during the run, but the efficiency of the chamber was not seriously impaired and due to the method by which the 30 cm chamber information was used, normalization of the data was in no way affected. No broken wires occurred during the run.

The high voltage on the chambers was ramped down by 500 V (to about -3200 V) between beam spills. This caused large displacement currents at the beginning and end of each spill. The ramp timing was carefully monitored to insure that the chambers were at plateau voltage before the first beam particles arrived.

Improvements That Could Be Made

In the future, chambers could be made more easily, more quickly and to perform better if the following changes were made:

(1) Make the chamber construction more massive. Chambers need not be made thicker to acquire additional strength but a larger mating surface area should be provided (e.g., the lucite strips were only 2.5 cm wide, a wider strip would provide more resistance to torque) and the frames should be extremely rigid from the beginning.

(2) Amplifiers sensitive to smaller signals (typical signals were 60 mV at the amplifier input) would be worth the effort to install--if the chambers could plateau 400 V lower (this is possible--it has recently been done by another group), currents (and hence discharges) could be kept to a minimum. The cleaning problems would be much less severe.

(3) Quick take-apart should be designed into any chamber. This is invaluable in development, testing and in cleaning.

(4) The amplifier cards should be modified to minimize the capacitive coupling between channels.

APPENDIX B

THE FIT MASS CALCULATION

Given an interaction point (x_o,y_o,z_o), and the locations where the muons exit the downstream face of the hadron absorber (x_1,y_1,z_A) and (x_2,y_2,z_A) and their slopes in x and y at these locations (m'_{x1}, m'_{y1}) and (m'_{x2}, m'_{y2}), a best estimate of the slopes of the muon tracks at the target (m_{x_1}, m_{y_1}) and (m_{x_2}, m_{y_2}), can be calculated (see Fig. 23). The joint probability density function for the projected multiple scattering with an angle $\Delta\theta$ and displacement Δx is[65]

$$P(x,\theta_x) \alpha \exp\left[-\frac{4}{\theta_s^2}\left(\frac{\Delta\theta^2}{z} - \frac{3\Delta x\Delta\theta}{z^2} + 3\frac{\Delta^2}{z^3}\right)\right]$$

where z is the length of the scattering medium

θ_s is $\frac{(0.021)^2}{PiPf}\frac{1}{x_o}$

Pi and Pf are the initial and final momenta in GeV/c

(i.e., upon entering and exiting the medium), and

x_o is the radiation length of the medium.

The for a given event scattering from the slopes above to the slopes and positions above is thus given by

$$P(x,\theta_x) \alpha \exp(-\chi^2/2)$$

where

$$\chi^2 = A(\theta'_{x_1} - \theta_{x_1})^2 + 2B(x'_1 - x_1)(\theta'_1 - \theta_{x_1}) + C(x'_1 - x_1)^2$$

+ terms for the y projection of track 1

+ terms for the x projection of track 2

+ terms for the y projection of track 2

where θ' is the observed angle of the muon track ($m' = \tan\theta'$)

and θ is the angle of the same track prior to multiple scattering

($m = \tan\theta$)

x' is the observed position of the track, and

x is the position of the track had there been no multiple scattering

$$A = \frac{8PiPf}{(0.021)^2}\frac{x_o}{z}$$

$$2B = \frac{-24PiPf}{(0.021)^2}\frac{x_o}{z^2}$$

$$C = \frac{24PiPf}{(0.021)^2}\frac{x_o}{z^3}$$

We choose the m_{x_1}, m_{x_2}, m_{y_1} and m_{y_2} to minimize the χ^2. It can readily be seen, however, that the χ^2 can be minimized in all four variables independently, since (a) scattering of track 1 and of track 2 proceeds independently of one another, and (b) the absorber is thick and hence the projected scattering in the x and y views is independent.

Thus, for each projection of each track an m can be chosen to minimize a simple χ^2,

$$\chi^2 = \Delta\theta^2 + 2B\Delta x\Delta\theta + \Delta x^2$$

where

$$\Delta\theta = \frac{m'-m}{1 + m'm}$$

m' = measured slope ($\tan\theta'$)

m = best estimate of the slope ($\tan\theta$)

$$\Delta\theta = \theta' - \theta \simeq \tan(\theta' - \theta)$$

$$\Delta x = x' - [x_o + m(z_A - z_o)]$$

$$= (x' - x_o) - m(z_A - z_o)$$

$$= \Delta_x - m\Delta_z$$

where (x_o, y_o, z_o) is the best estimate of the production point,

z_A is the z plane where x' is observed,

$\Delta_x = x' - x_o$ and

$\Delta_z = z_A - z_o$.

Thus

$$\chi^2 = A\left(\frac{m'-m}{1 + m'm}\right)^2 + 2B(\Delta_x - m\Delta_2)\left(\frac{m'-m}{1 + m'm}\right) + C(\Delta_x - m\Delta_2)^2$$

but, $m'm << 1$ because the track angles are small ($m'm$ is typically $\lesssim 0.012$).

$$\chi^2 = A(m'-m) + 2B(\Delta_x - m\Delta_z)(m'-m) + C(\Delta_x - m\Delta_z)^2$$

Now we minimize with respect to m

$$0 = \frac{\delta\chi^2}{\delta m} = -2A(m'-m) - 2B[(\Delta_x - m\Delta_z) + \Delta_z(m'-m)] - 2C(\Delta_x - m\Delta_z)\Delta_z$$

And solving for m,

$$m = \frac{Am' + B(\Delta_x + m\Delta_z) + C\Delta_x\Delta_z}{A + 2B\Delta_z + C\Delta_z^2}$$

The opening angles obtained from these slopes, when inserted into the equation in The 55-80 cm Analysis, yield the dimuon mass.

REFERENCES

1. Experiments cited by J. W. Cronin in Review of Direct Lepton Production in Nucleon-Nucleon Collisions, Lecture prepared for the International School of Subnuclear Physics, Erice, July 1975. The lecture presents a useful summary of the experimental situation, as of 1975, with respect to the high direct lepton signal observed in hadronic reactions. Several of the references below, about the state of the art as of 1975, are also to be found as references in the J. W. C. paper. Experiments referred to by J. W. C. with respect to the large single muon signal include Ref. 2-9 below. Useful caveats and interpretations of the experiments are also provided by J. W. C. (see also Ref. 10).

2. G. B. Bondarnko et al., cited by V. Lebedev in Proceedings of the XVI International Conference on High Energy Physics, The University of Chicago and Fermi National Accelerator Laboratory, 1972, Edited by J. D. Jackson and A. Roberts (National Accelerator Laboratory, Batavia, IL., 1973), Vol. 2, p. 329.

3. V. V. Abramov et al., reported in Proceedings of the XVII International Conference on High Energy Physics, London, 1974 (Rutherford Lab., Chilton, Didcot, 1974), p. V-53.

4. J. P. Boymond et al., Phys. Rev. Lett. 33, 112 (1974).

5. J. A. Appel et al., Phys. Rev. Lett. 33, 722 (1974).

6. D. Bintinger et al., Phys. Rev. Lett. 35, 72 (1975).

7. R. C. Lamb et al., Phys. Rev. Lett. 15, 800 (1965).

8. P. J. Wanderer et al., Phys. Rev. Lett. 23, 729 (1969).

9. C. M. Ankenbrandt et al., Phys. Rev. D3, 2582 (1971).

10. L. B. Leipuner et al., Phys. Rev. Lett. 34, 103 (1975).

11. This was observed in experiments where variable density targets were used to extrapolate to "infinite density"--i.e., to lifetimes comparable to the travel time of a particle passing between nuclei. See references under Ref. 1.

12. An extended discussion on energy and transverse momentum dependence can be found in Ref. 1. See also Ref. 4.

13. V. Blobel et al., Phys. Lett. 488, 73 (1974).

14. J. H. Christenson et al., Phys. Rev. D8, 2016 (1973).

15. J. A. Appel et al., Phys. Rev. Lett. 35, 9 (1975).

16. V. Blobel et al., Nucl. Phys. B69, 237 (1974). One caveat would be in order here; this experiment measured only the exclusive reaction pp → ppM where M is the meson of interest (ρ, φ, etc.).

17. For useful discussions of the discovery of, and the dimuon physics of the psi, see the Ph.D. thesis by J. G. Branson, Measurement of Inclusive Muon Pair Production by 225-GeV/c π^+, π^-, and Proton Beams With a Large Acceptance Spectrometer, Princeton University, May 1977, and references contained therein.

18. M. Bourquin and J.-M. Gaillard, Phys. Letts., 59B, 191 (1975).

19. B. D. Hyams et al., Phys. Lett.29B, 128 (1969).

20. A. W. Wehmann et al., Phys. Rev. Lett. 20, 748 (1968).

21. Particle Data Group, Rev. Mod. Phys. 48, S1 (1976).

22. J. Bartke et al., Preprint, 2 Aug. (1976), CERN/EP/PHYS. 76-2B Rev., The evaluation is more recent than Ref. 23 and at higher energy, but is also more recent than 1975, at which time the interest in single lepton experiments was at its peak.

23. F. Bulos et al., Phys. Rev. 187, 5, 1830 (1969).

24. C.-H. Lai and C. Quigg, Fermilab Note FN-296 2000.000.

25. S. D. Drell and T. M. Yan, Phys. Rev. Lett. 25, 316 (1970).

26. J. D. Bjorken and H. Weisberg, Phys. Rev. D13, 1405 (1976).

27. If $s = [(E_1,p_1)+(E_2,p_2)]^2$, is the square of the beam-particle-plus-target-particle invariant energy, the "Feyneman x" variable, x_F, for a given produced particle is defined to be $x_F = 2p^*_{\parallel} / \sqrt{s}$, where $p^*_{\parallel}$ is the longitudinal momentum (along the beam direction) of that particle in the center of mass system of the initial particles.

28. S. M. Berman, D. J. Levy, T.L. Neff, Phys. Rev. Lett. 23, 1363 (1969).

29. See Ref. 3, p. V-54.

30. E. W. Beier et al., Paper B-05 submitted to International Conference on High Energy Physics, Palermo, June, 1975. A more recent publication from this group can be found in Phys. Rev. Lett. 37, 1117 (1976).

31. F. W. Büsser et al., Phys. Lett. 53B, 212 (1974). Also F.W. Büsser et al., B-06 paper--presented to the International Conference on High Energy Physics, Palermo, June 1975.

32. L. M. Lederman, Proceedings of the 1975 International Symposium on Lepton and Photon Interactions at High Energies, Stanford Univ., p. 265 (1975).

33. J. G. Branson, Princeton University, Ph.D. Thesis, May, 1977.

34. B. Aubert et al., FERMILAB- Conf.-75/31-EXP, April, 1975.

35. Stephen H. Pordes, Harvard University, Ph.D. Thesis, February, 1976.

36. Richard Fine, University of Chicago, Ph.D. Thesis, May, 1976.

37. Z is increasing toward the downstream end of the experiment and is along the beam, y is up and x is to the left, looking downstream. This defines a right-handed coordinate system.

38. K. J. Anderson et al., Addendum to Fermilab Proposal 331, unpublished.

39. T. A. Nunamaker, "University Wire Detector CAMAC Scanner," Enrico Fermi Institute, University of Chicago.

40. D. Theriot, Fermilab-TM-229, March, 1970.

41. S. P. Denisov et al., Nucl. Phys. B61, 62 (1973).

42. F. C. Winkelmann et al., Phys. Lett. 56B, 101 (1975).

43. L. Foa, Phys. Rep. 22C, 3 (1975); J. Whitmore, Phys. Rep. 27C, 187 (1976).

44. For the ρ and ω branching ratios μ-e universality is assumed and we use e^+e^- annihilation data. We use $\Gamma(\rho \to \mu\mu)/\Gamma(\rho \to \text{all}) = 4.3 \times 10^{-5}$, $\Gamma(\omega \to \mu\mu)/\Gamma(\omega \to \text{all}) = 7.6 \times 10^{-5}$ and $\Gamma(\phi \to \mu\mu)/\Gamma(\phi \to \text{all}) = 2.5 \times 10^{-4}$. See Ref. 21.

45. A. M. Rossi et al., Nucl. Phys., B84, 298 (1975).

46. A. M. Rossi et al., Nucl. Phys. B84, 269 (1975); U. Amaldi et al., Nucl. Phys. B86, 403 (1975); M. G. Albrow et al., Nucl. Phys. B73, 40 (1974).

47. Y. S. Tsai, Rev. Mod. Phys. 46, 815 (1974).

48. C.-H. Lai, private communication. See also Ref. 24.

49. K. Bunnel et al.- SLAC-PUB-2027, Oct., 1977, submitted to Phys. Rev. Lett.

50. G. Farrar and S. Frautschi, Phys. Rev. Lett. 36, 1017 (1976).

51. M. Duong-Van et al., SLAC Preprint (1976) "A Model for Massive Lepton Pair Production."

52. K. J. Anderson et al., Phys. Rev. Lett. 37, 799 (1976).

53. T. Eichten et al., Nucl. Phys. B44, 333 (1972).

54. J. G. Branson et al., Phys. Rev. Lett. 38, 457 (1977).

55. D. Buchholz et al., Phys. Rev. Lett. 36, 932 (1976).

56. L. B. Leipuner et al., Phys. Rev. Lett. 35, 1613 (1975); H. Kasha et al., Phys. Rev. Lett. 36, 1007 (1976).

57. J. W. Cronin et al., Phys. Rev. D11, 3105 (1975).

58. D. Antreasyan, private communication, Data will appear in Ph.D. Thesis by James Muller, Princeton University. Most of the data used here is a re-analysis of the data presented in J. P. Boymond et al., Phys. Rev. Lett. 33, 112 (1974).

59. J. A. Appel et al., Phys. Rev. Lett. 33, 722 (1974).

60. D. Bintinger et al., Phys. Rev. Lett. 35, 72 (1975).

61. Epi-Cure epoxy 874:815 in 1:6 mix ratio, Celanese Coatings Co., Louisville, Ky.

62. The super magic gas maxture is 24 per cent isobutane, 71.3 per cent argon, 4 per cent dimethoxymethane, 0.7 per cent Freon 13B1.

63. General Electric, Silicon Products Dept., Waterford, N.Y.

64. General Electric, Schenectady, N.Y.

65. B. Rossi and K. Greisen, Cosmic Ray Theory, Rev. Mod. Phys. 13, 267 (1941).

TABLE 1

225 GeV/c DATA SAMPLE INFORMATION

	Beam type		
	p	π^+	π^-
Beam particles	1.05×10^{10}	2.26×10^9	7.70×10^9
Triggers[a]	---- 2.00×10^5 total ----		2.52×10^5
Low mass reconstruction	1.25×10^4	3.41×10^3	1.43×10^4
After momentum cuts	1.24×10^4	3.39×10^3	1.41×10^4
After weighting by acceptance including chamber efficiency	8.43×10^4	2.04×10^4	8.92×10^4
Sensitivity (events/nb)	1.16	0.296	1.31

[a]Includes shield-induced events, decay produced pairs, prescaled trigger, etc.

TABLE 2

CROSS SECTIONS BINNED IN x_F

Region	0.12	0.22	0.32	0.42	0.52	$\langle x_F \rangle$ 0.62	0.72	0.82	0.92	Total ($0.07 \leq x_F$)
					Proton $\frac{d\sigma}{dx}\Delta x$					
I	0.367E-29 ±0.253E-30	0.681E-30 0.359E-31	0.163E-30 0.116E-31	0.414E-31 0.508E-32	0.957E-32 0.260E-32	0.152E-32 0.880E-33				0.4566E-29
II	0.127E-29 ±0.741E-31	0.247E-30 0.118E-31	0.971E-31 0.600E-32	0.343E-31 0.340E-32	0.139E-31 0.220E-32	0.449E-32 0.136E-32	0.216E-32 0.100E-32	0.343E-33 0.344E-33		0.1671E-29
III	0.168E-29 ±0.102E-30	0.494E-30 0.206E-31	0.196E-30 0-917E-32	0.101E-30 0.599E-32	0.560E-31 0.428E-32	0.274E-31 0.303E-32	0.102E-31 0.216E-32	0.475E-32 0.181E-32		0.2573E-29
IV	0.285E-30 ±0.238E-31	0.743E-31 0.581E-32	0.286E-31 0.299E-32	0.117E-31 0.183E-32	0.603E-32 0.132E-32	0.918E-33 0.531E-33	0.765E-33 0.541E-33			0.4069E-30
V	0.740E-31 ±0.944E-32	0.168E-31 0.262E-32	0.507E-32 0.124E-32	0.340E-32 0.946E-33	0.199E-32 0.752E-33	0.000E-00 0.284E-33	0.305E-33 0.305E-33			0.1016E-30
	6.98 mb	15.1	4.90	1.92	.875	3.43×10^{-1} mb	1.34×10^{-1}	4.91×10^{-2}		
					$\pi^+ \frac{d\sigma}{dx}\Delta x$					
I	0.341E-29 ±0.264E-30	0.914E-30 0.634E-31	0.301E-30 0.305E-31	0.122E-30 0.182E-31	0.561E-31 0.139E-31	0.214E-31 0.816E-32	0.883E-32 0.627E-32	0.500E-32 0.501E-32		0.4841E-29
II	0.107E-29 ±0.809E-31	0.318E-30 0.240E-31	0.140E-30 0.144E-31	0.752E-31 0.105E-31	0.244E-31 0.614E-32	0.350E-31 0.811E-32	0.327E-31 0.954E-32	0.180E-31 0.812E-32		0.1718E-29
III	0.154E-29 ±0.118E-30	0.500E-30 0.323E-31	0.269E-30 0.200E-31	0.175E-30 0.157E-31	0.122E-30 0.129E-31	0.877E-31 0.115E-31	0.967E-31 0.142E-31	0.346E-31 0.106E-31	0.167E-31 0.973E-32	0.2841E-29

IV	0.266E-30	0.109E-30	0.528E-31	0.324E-31	0.227E-31	0.124E-31	0.193E-31	0.120E-31		0.5261E-30
	±0.387E-31	0.140E-31	0.835E-32	0.640E-32	0.539E-32	0.414E-32	0.584E-32	0.602E-32		
V	0.487E-31	0.197E-31	0.115E-31	0.117E-32	0.402E-32	0.128E-32	0.152E-32			0.8790E-31
	±0.138E-31	0.548E-32	0.385E-32	0.117E-32	0.232E-32	0.128E-32	0.152E-32			
	11.9 μb ±9 Auger	3.49±.2	1.44±.4	0.76±.08	.4±.1	.3±.1	.3±.1			

$\pi^- \frac{d\sigma}{dx}\Delta x$

I	0.357E-29	0.774E-30	0.251E-30	0.127E-30	0.501E-31	0.213E-31	0.961E-32	0.101E-31	0.620E-32	0.4818E-29
	±0.246E-30	0.400E-31	0.156E-31	0.103E-31	0.630E-32	0.442E-32	0.326E-32	0.514E-32	0.444E-32	
II	0.106E-29	0.252E-30	0.101E-30	0.600E-31	0.358E-31	0.266E-31	0.193E-31	0.178E-31	0.390E-32	0.1579E-29
	±0.613E-31	0.117E-31	0.609E-32	0.455E-32	0.356E-32	0.332E-32	0.341E-32	0.445E-32	0.278E-32	
III	0.135E-29	0.447E-30	0.250E-30	0.164E-30	0.108E-30	0.832E-31	0.609E-31	0.547E-31	0.368E-31	0.2555E-29
	±0.812E-31	0.188E-31	0.107E-31	0.793E-32	0.614E-32	0.562E-32	0.559E-32	0.692E-32	0.717E-32	
IV	0.248E-30	0.733E-31	0.350E-31	0.229E-31	0.125E-31	0.870E-32	0.620E-32	0.295E-32	0.785E-32	0.4174E-30
	±0.205E-31	0.568E-32	0.329E-32	0.254E-32	0.189E-32	0.163E-32	0.156E-32	0.121E-32	0.252E-32	
V	0.615E-31	0.204E-31	0.920E-32	0.418E-32	0.477E-32	0.233E-32	0.993E-33	0.129E-32	0.280E-32	0.1075E-30
	±0.794E-32	0.273E-32	0.159E-32	0.105E-32	0.113E-32	0.827E-33	0.574E-33	0.747E-33	0.141E-32	
	11.8	3.3	1.2	.7	.39	.25	.20	.16		

Shown are the cross sections, per interval, observed in the 225 GeV/c data. The interaction type is shown at the top of each section. Cross sections are given in the first line and the restricted errors are shown in the next line. All cross sections are per nucleus. The quantities, binned in x_F, are per bin 0.10 units wide and are for bins extending over $0.07 < x_F < 0.17$, $0.17 < x_F < 0.27$, etc. "Total" is the total cross section across all x_F measured. All x_F cross sections are integrated across $0 \leq p_T \leq 3.0$ GeV/c. Cross sections are given in units of cm^2. Thus, for example, in the proton data we observe 4566 nb (±12 per cent--see text) for $0.07 \leq x_F < 1.0$, $0.0 < p_T < 3.0$ GeV/c, and $0.21 < M \leq 0.45$ GeV/c^2 and we observe 3670 nb (±25 per cent nb restricted) for $0.07 \leq x_F \leq 0.17$, 0.0 $p_T \leq 3.0$ GeV/c and $0.21 < M \leq 0.45$ GeV/c^2.

TABLE 3

CROSS SECTIONS BINNED IN x_F AND WEIGHTED BY E

Region	0.12	0.22	0.32	0.42	0.52 $\langle x_F \rangle$	0.62	0.72	0.82	0.92	Total ($0.07 \leq x_F$)
					Proton $E\frac{d\sigma}{dx}\Delta x$					
I	0.457E-29 ±0.315E-30	0.152E-29 0.803E-31	0.526E-30 0.376E-31	0.176E-30 0.215E-31	0.506E-31 0.137E-31	0.925E-32 0.535E-32				0.6854E-29
II	0.169E-29 ±0.987E-31	0.569E-30 0.271E-31	0.323E-30 0.200E-31	0.149E-30 0.148E-31	0.730E-31 0.116E-31	0.287E-31 0.872E-32	0.159E-31 0.800E-32	0.283E-32 0.283E-32		0.2854E-29
III	0.253E-29 ±0.153E-30	0.119E-29 0.495E-31	0.669E-30 0.314E-31	0.441E-30 0.262E-31	0.302E-30 0.231E-31	0.175E-30 0.193E-31	0.765E-31 0.162E-31	0.395E-31 0.150E-31		0.5420E-29
IV	0.468E-30 ±0.391E-31	0.187E-30 0.146E-31	0.990E-31 0.104E-31	0.522E-31 0.816E-32	0.330E-31 0.724E-32	0.573E-32 0.331E-32	0.581E-32 0.411E-32			0.8507E-30
V	0.144E-30 ±0.184E-31	0.454E-31 0.707E-32	0.186E-31 0.453E-32	0.154E-31 0.427E-32	0.110E-31 0.416E-32	0.000E-00 0.157E-32	0.239E-32 0.240E-32			0.2366E-30
		3.56 mb.								
					π^+ $E\frac{d\sigma}{dx}\Delta x$					
I	0.429E-29 ±0.332E-30	0.211E-29 0.146E-30	0.100E-29 0.101E-30	0.529E-30 0.787E-31	0.296E-30 0.734E-31	0.138E-20 0.526E-31	0.667E-31 0.473E-31	0.417E-31 0.418E-31		0.8477E-29
II	0.145E-29 ±0.109E-30	0.751E-30 0.566E-31	0.467E-30 0.479E-31	0.325E-30 0.456E-31	0.132E-30 0.333E-31	0.224E-30 0.519E-31	0.242E-30 0.707E-31	0.151E-30 0.679E-31		0.3741E-29
III	0.228E-29 ±0.175E-30	0.122E-29 0.787E-31	0.924E-30 0.690E-31	0.771E-30 0.690E-31	0.658E-30 0.696E-31	0.566E-30 0.742E-31	0.725E-30 0.107E-30	0.287E-30 0.876E-31	0.154E-30 0.897E-31	0.7588E-29

IV	0.434E-30	0.273E-30	0.183E-30	0.145E-30	0.124E-30	0.790E-31	0.144E-30	0.102E-30		0.1485E-29
	±0.631E-31	0.352E-31	0.290E-31	0.287E-31	0.294E-31	0.264E-31	0.428E-31	0.514E-31		
V	0.989E-31	0.558E-31	0.414E-31	0.540E-32	0.233E-31	0.822E-32	0.109E-31			0.2439E-30
	±0.279E-31	0.156E-31	0.128E-31	0.540E-32	0.135E-31	0.822E-32	0.109E-31			

π^- $E\frac{d\sigma}{dx}\Delta x_F$

I	0.442E-29	0.173E-29	0.826E-30	0.547E-30	0.270E-30	0.138E-30	0.710E-31	0.873E-31	0.576E-31	0.8150E-29
	±0.305E-30	0.895E-31	0.512E-31	0.445E-31	0.339E-31	0.286E-31	0.241E-31	0.445E-31	0.413E-31	
II	0.142E-29	0.585E-30	0.338E-30	0.260E-30	0.191E-30	0.170E-30	0.144E-30	0.151E-30	0.374E-31	0.3296E-29
	±0.828E-31	0.272E-31	0.203E-31	0.197E-31	0.191E-31	0.212E-31	0.254E-31	0.377E-31	0.267E-31	
III	0.285E-29	0.108E-29	0.855E-30	0.727E-30	0.583E-30	0.539E-30	0.455E-30	0.461E-30	0.347E-30	0.7103E-29
	±0.123E-30	0.455E-31	0.364E-31	0.352E-31	0.332E-31	0.364E-31	0.418E-31	0.584E-31	0.676E-31	
IV	0.418E-30	0.185E-30	0.124E-30	0.102E-30	0.690E-31	0.559E-31	0.473E-31	0.252E-31	0.742E-31	0.1100E-29
	±0.345E-31	0.144E-31	0.116E-31	0.113E-31	0.104E-31	0.105E-31	0.119E-31	0.103E-31	0.238E-31	
V	0.119E-30	0.559E-31	0.340E-31	0.189E-31	0.264E-31	0.157E-31	0.756E-32	0.106E-31	0.270E-31	0.3153E-30
	±0.154E-31	0.747E-32	0.588E-32	0.476E-32	0.626E-32	0.556E-32	0.437E-32	0.615E-32	0.136E-31	

Shown are the cross sections, per interval, observed in the 225 GeV/c data. The interaction type is shown at the top of each section. Cross sections are given in the first line and the restricted errors are shown in the next line. All cross sections are per nucleus. The quantities, binned in x_F, are per bin 0.10 units wide and are for bins extending over $0.07 < x_F < 0.17$, $0.17 < x_F < 0.27$, etc. "Total" is the total cross section,also weighted by E, across all x_F measured. All x_F cross sections are integrated across $0.0 \leq p_T \leq 3.0$ GeV/c. Cross sections are given in units of cm^2 GeV/c^2.

TABLE 4

CROSS SECTIONS BINNED IN p_T AND WEIGHTED BY $1/p_T$

Region	and	$\frac{100}{1700}$	$\frac{300}{1900}$	$\frac{500}{2100}$	$\frac{700}{2300}$	$\langle p_T \rangle$ $\frac{900}{2500}$	$\frac{1100}{2700}$	$\frac{1300}{2900}$	1500	Total ($0.0 < p_T < 3.0$ GeV/c)
					Proton $\frac{1}{p_T}\frac{d\sigma}{dp_T}\Delta p_T$					
I		0.124E-28	0.529E-29	0.215E-29	0.770E-30	0.271E-30	0.117E-30	0.375E-31	0.976E-32	
		±0.845E-31	0.971E-31	0.685E-31	0.384E-31	0.207E-31	0.135E-31	0.811E-32	0.361E-32	
	and	0.645E-32	0.402E-33	0.128E-32	0.000E-00	0.000E-00	0.272E-33			0.2102E-28
		±0.497E-32	0.765E-33	0.131E-32	0.655E-33	0.655E-33	0.718E-33			
II		0.271E-29	0.183E-29	0.863E-30	0.354E-30	0.126E-30	0.599E-31	0.134E-31	0.763E-32	
		±0.165E-31	0.297E-31	0.239E-31	0.162E-31	0.920E-32	0.717E-32	0.326E-32	0.298E-32	
	and	0.453E-32	0.711E-33	0.169E-33	0.498E-33					0.5972E-29
		±0.291E-32	0.133E-32	0.344E-33	0.110E-32					
III		0.289E-29	0.223E-29	0.126E-29	0.656E-30	0.301E-30	0.139E-30	0.617E-31	0.174E-31	
		±0.174E-31	0.336E-31	0.317E-31	0.251E-31	0.170E-31	0.113E-31	0.804E-32	0.387E-32	
	and	0.848E-32	0.550E-32	0.309E-32	0.600E-33	0.146E-33	0.304E-33	0.328E-33		0.7579E-29
		±0.267E-32	0.292E-32	0.189E-32	0.784E-33	0.352E-33	0.588E-33	0.663E-33		
III		0.457E-30	0.342E-30	0.201E-30	0.103E-30	0.593E-31	0.225E-31	0.592E-32	0.451E-32	
		±0.423E-32	0.926E-32	0.910E-32	0.725E-32	0.642E-32	0.385E-32	0.192E-32	0.235E-32	
	and	0.295E-32	0.139E-32	0.000E-00	0.157E-33					0.1200E-29
		±0.196E-32	0.132E-32	0.658E-33	0.360E-33					
V		0.149E-30	0.558E-31	0.369E-31	0.329E-31	0.976E-32	0.784E-32	0.430E-32	0.531E-32	
		±0.287E-32	0.337E-32	0.349E-32	0.393E-32	0.201E-32	0.253E-32	0.160E-32	0.348E-32	
	and	0.387E-33	0.175E-33	0.145E-33	0.116E-32					0.3025E-30
		±0.451E-33	0.334E-33	0.305E-33	0.258E-32					
					$\pi^+ \frac{1}{p_T}\frac{d\sigma}{dp_T}\Delta p_T$					
I		0.128E-28	0.565E-29	0.220E-29	0.835E-30	0.213E-30	0.797E-31	0.311E-31	0.426E-31	
		±0.114E-30	0.121E-30	0.843E-31	0.593E-31	0.284E-31	0.201E-31	0.126E-31	0.243E-31	
	and	0.332E-32	0.138E-31	0.000E-00	0.111E-32					0.2188E-28
		±0.417E-32	0.252E-31	0.240E-31	0.256E-32					

II		0.214E-29	0.212E-29	0.057E-30	0.379E-30	0.936E-31	0.487E-31	0.286E-31	0.760E-32	
		±0.253E-31	0.455E-31	0.356E-31	0.270E-31	0.132E-31	0.122E-31	0.942E-32	0.435E-32	
	and	0.000E-00	0.900E-33	0.000E-00	0.113E-32					0.5677E-29
		±0.164E-32	0.160E-32	0.167E-32	0.252E-32					
III		0.387E-29	0.276E-29	0.149E-29	0.760E-30	0.301E-30	0.113E-30	0.651E-31	0.195E-31	
		±0.272E-31	0.553E-31	0.495E-31	0.411E-31	0.261E-31	0.160E-31	0.159E-31	0.677E-32	
	and	0.809E-32	0.232E-32							0.8592E-29
		±0.524E-37	0.259E-32							
IV		0.988E-30	0.455E-30	0.226E-30	0.138E-30	0.668E-31	0.347E-31	0.391E-32	0.145E-31	
		±0.847E-32	0.184E-31	0.152E-31	0.171E-31	0.118E-31	0.957E-32	0.282E-32	0.722E-32	
	and	0.350E-32	0.000E-00	0.000E-00	0.000E-00	0.503E-33				0.1931E-29
		±0.344E-32	0.198E-32	0.198E-32	0.198E-32	0.127E-32				

$$\pi^- \quad \frac{1}{p_T} \frac{d\sigma}{dp_T} \Delta p_T$$

I		0.127E-28	0.610E-29	0.217E-29	0.794E-30	0.239E-30	0.753E-31	0.359E-31	0.119E-31	
		±0.771E-31	0.109E-30	0.666E-31	0.377E-31	0.183E-31	0.982E-32	0.758E-32	0.479E-32	
	and	0.229E-32	0.244E-32	0.892E-33	0.356E-33	0.248E-33				0.2216E-28
		±0.158E-32	0.264E-32	0.132E-32	0.805E-33	0.628E-33				
II		0.252E-29	0.188E-29	0.818E-30	0.306E-30	0.135E-30	0.415E-31	0.134E-31	0.500E-32	
		±0.145E-31	0.287E-31	0.215E-31	0.134E-31	0.972E-32	0.508E-32	0.299E-32	0.195E-32	
	and	0.189E-32	0.201E-33	0.322E-33						0.5722E-29
		±0.119E-32	0.371E-33	0.471E-33						
III		0.313E-29	0.221E-29	0.134E-29	0.613E-30	0.296E-30	0.135E-30	0.499E-31	0.192E-31	
		±0.163E-31	0.309E-31	0.312E-31	0.219E-31	0.156E-31	0.104E-31	0.571E-32	0.368E-32	
	and	0.738E-32	0.390E-32	0.121E-32	0.125E-32	0.538E-33	0.000E-00	0.390E-33		0.7802E-29
		±0.243E-32	0.235E-32	0.102E-32	0.100E-32	0.764E-33	0.440E-33	0.816E-33		
IV		0.404E-30	0.324E-30	0.212E-30	0.104E-30	0.575E-31	0.194E-31	0.169E-31	0.746E-32	
		±0.534E-32	0.826E-32	0.858E-32	0.669E-32	0.545E-32	0.315E-32	0.371E-32	0.273E-32	
	and	0.138E-32	0.799E-33	0.155E-32	0.452E-33	0.244E-33				0.1150E-29
		±0.382E-33	0.738E-33	0.188E-32	0.595E-33	0.602E-33				

TABLE 4--continued

Region	$\frac{100}{1700}$	$\frac{300}{1900}$	$\frac{500}{2100}$	$\frac{700}{2300}$ $\langle p_T \rangle$	$\frac{900}{2500}$	$\frac{1100}{2700}$	$\frac{1300}{2900}$	1500	Total ($0.0 < p_T < 3.0$ GeV/c
V	0.673E-31	0.704E-31	0.402E-31	0.256E-31	0.241E-31	0.578E-32	0.288E-32	0.227E-32	
	±0.206E-32	0.317E-32	0.372E-32	0.313E-32	0.353E-32	0.153E-32	0.112E-32	0.112E-32	
and	0.695E-33	0.157E-32	0.000E-00	0.000E-00	0.115E-33				0.2490E-30
	±0.864E-33	0.206E-32	0.145E-32	0.145E-32	0.293E-33				

Shown are the cross sections, per interval, observed in the 225 GeV/c data. The interaction type is shown at the top of each section. Cross sections are given in the first line and the restricted errors are shown in the next line. All cross sections are per nucleus. The quantities, binned in p_T, are per bin 200 MeV/c wide and are for bins extending over $0.0 \leq p_T < 200$ MeV/c, $200 \leq p_T < 400$ MeV/c, etc. "Total" is the total cross section also weighted by $1/p_T$ across all p_T measured. All p_T cross sections are integrated across $0.07 \leq x_F$. Cross sections are given in units of $cm^2\ c^2/GeV^2$.

TABLE 5

CROSS SECTIONS AND PARAMETRIZATIONS--pC, 225 GeV/c[a]

Region	Mass (GeV/c^2)	Source	A ($nb/GeV^2/c$)	b $(Gev/c)^{-1}$	c	Fit χ^2/D.O.F.		Cross Section (x_F>0.07) /nucleus /nucleon (nb)		Adep. used
						p_T	x_F			
I	0.21-0.45	Cont	$(6.64\pm.80)\times10^4$	5.15±.22	11.18± .32	5.7/10	3.2/4	4566 ± 548	871 ± 104	.67
II	0.45-0.65	Cont	$(1.39\pm.17)\times10^4$	4.78±.11	7.18± .28	7.7/ 8	21. /6	1671 ± 200	319 ± 38	.67
III	0.65-0.93	$\rho+\omega$	$(7.17\pm.86)\times10^3$	3.89±.07	5.28± .17	20. /11	20. /6	1819 ± 218	347 ± 42	.67
		Cont	$(2.97\pm.36)\times10^3$	3.89±.07	5.28± .17	20. /11	20. /6	754 ± 90	144 ± 17	.67
IV	0.93-1.13	ϕ	$(1.47\pm.18)\times10^3$	3.79±.15	7.50± .42	11. / 8	7.2/5	249 ± 30	39 ± 5	.75
		Cont	933±112	3.79±.15	7.50± .42	11. / 8	7.2/5	158 ± 19	24 ± 3	.75
V	1.13-2.00	Cont	622± 80	3.21±.22	9.01±1.07	15. / 8	9.1/5	102 ± 12	12 ± 1.5	.85

[a]Fit to $E(d\sigma^3/dp_T^3) = A\exp(-bp_T)\exp(-cx_F)$ and normalized so that the cross section is correct when integrated over all p_T and over $x_F > .07$ for the 225 GeV/c data and $x_F > .15$ for the 150 GeV/c data. b is fit by excluding points with $p_T < 400$ MeV/c.

TABLE 6

CROSS SECTIONS AND PARAMETRIZATIONS--π^+C, 225 GeV/c

Region	Mass (GeV/c^2)	Source	A ($nb/GeV^2/c$)	b $(GeV/c)^{-1}$	c	Fit χ^2/D.O.F.		Cross Section ($x_F>0.07$) /nucleus (nb)	/nucleon (nb)	Adep. used
						p_T	x_F			
I	0.21-0.45	Cont	$(4.31\pm.52)\times10^4$	5.47±.21	6.94± .38	6.4/ 8	5.8/6	4841 ± 581	923 ± 111	.67
II	0.45-0.65	Cont	$(9.70\pm1.16)\times10^3$	5.02±.20	4.95± .40	12. / 8	18. /6	1718 ± 206	328 ± 39	.67
III	0.65-0.93	$\rho+\omega$	$(5.00\pm.60)\times10^3$	4.15±.12	2.43± .22	8.4/ 6	28. /7	2068 ± 248	394 ± 47	.67
		Cont	$(1.87\pm.22)\times10^3$	4.15±.12	2.43± .22	8.4/ 6	28. /7	773 ± 93	147 ± 18	.67
IV	0.93-1.13	ϕ	922±111	3.89±.09	2.83± .52	15. / 9	6.4/6	370 ± 44	57 ± 7	.75
		Cont	389± 47	3.89±.09	2.83± .52	15. / 9	6.4/6	156 ± 19	24 ± 3	.75
V	1.13-2.00	Cont	223± 27	2.31±.41	7.06±1.52	9.6/10	5.9/5	88 ± 11	11 ± 1.3	.85

TABLE 7

CROSS SECTIONS AND PARAMETRIZATIONS--π^-C, 225 GeV/c

Region	Mass (GeV/c^2)	Source	A ($nb/GeV^2/c$)	b $(GeV/c)^{-1}$	c	Fit χ^2/D.O.F.		Cross Section ($x_F>0.07$) (nb)		Adep. used
						p_T	x_F	/nucleus	/nucleon	
I	0.21-0.45	Cont	$(4.08\pm.48)\times10^4$	5.43±.18	6.71±.28	5.5/ 9	19./6	4818 ± 578	919 ±110	.67
II	0.45-0.65	Cont	$(7.57\pm.91)\times10^3$	4.96±.11	4.22±.27	8.3/ 7	70./7	1579 ± 190	301 ± 36	.67
III	0.65-0.93	$\rho+\omega$	$(3.82\pm.46)\times10^3$	4.04±.07	1.98±.13	11. /11	43./7	1868 ± 224	357 ± 43	.67
		Cont	$(1.40\pm.17)\times10^3$	4.04±.07	1.98±.13	11. /11	43./7	687 ± 82	131 ± 16	.67
IV	0.93-1.13	ϕ	762±91	3.69±.13	3.67±.33	9.6/ 9	25./7	278 ± 33	43 ± 5	.75
		Cont	381±46	3.69±.13	3.67±.33	9.6/ 9	25./7	139 ± 17	22 ± 3	.75
V	1.13-2.00	Cont	312±38	3.23±.23	4.45±.67	11. / 9	13./7	108 ± 13	13.1± 1.6	.85

TABLE 8

CROSS SECTIONS AND PARAMETRIZATIONS--pBe, 150 GeV/c

Region	Mass (GeV/c^2)	Source	A ($nb/GeV^2/c$)	b $(GeV/c)^{-1}$	c	Fit χ^2/D.O.F. p_T	Fit χ^2/D.O.F. x_F	Cross Section (x_F>0.15) /nucleus (nb)	Cross Section (x_F>0.15) /nucleon (nb)	Adep. used
I	0.21-0.45	Cont	$(1.06\pm.13)\times10^5$	5.28±.14	10.62±.38	4.6/6	1.0/5	1992 ± 239	460 ±55	.67
II	0.45-0.65	Cont	$(1.97\pm.24)\times10^4$	4.50±.12	8.58± .25	6.0/6	19. /6	781 ± 94	180 ±22	.67
III	0.65-0.93	$\rho + \omega$	$(1.17\pm.14)\times10^4$	3.86±.08	6.61± .16	11. /6	18. /6	983 ± 117	225 ±27	.67
		Cont	$(4.53\pm.54)\times10^3$	3.86±.08	6.61± .16	11. /6	18. /6	376 ± 45	87 ±10	.67
IV	0.93-1.13	ϕ	$(1.99\pm.24)\times10^3$	3.58±.18	8.48± .54	11. /6	3.8/4	115 ± 14	22 ± 3	.75
		Cont	$(1.03\pm.12)\times10^3$	3.58±.18	8.48± .54	11. /6	3.8/4	60 ± 7	11.5± 1.4	.75
V	1.13-2.00	Cont	$(1.09\pm.13)\times10^3$	3.09±.33	9.85±1.05	13. /6	.72/4	53 ± 6	8.2± 1.0	.85

TABLE 9

CROSS SECTIONS AND PARAMETRIZATIONS--π^+Be, 150 GeV/c

Region	Mass (GeV/c^2)	Source	A (nb/GeV^2c)	b $(GeV/c)^{-1}$	c	Fit χ^2/D.O.F. p_T	Fit χ^2/D.O.F. x_F	Cross Section (x_F>0.15) /nucleus (nb)	Cross Section (x_F>0.15) /nucleon (nb)	Adep. used
I	0.21-0.45	Cont	$(7.10\pm.85)\times10^4$	5.65±.23	6.96± .34	6.2/6	3.0/5	2764 ±332	638 ±77	.67
II	0.45-0.65	Cont	$(7.69\pm.92)\times10^3$	4.76±.17	3.76± .24	16. /6	14. /6	978 ±117	226 ±27	.67
III	0.65-0.93	$\rho+\omega$	$(7.09\pm.85)\times10^3$	4.06±.03	3.77± .14	4.3/6	55. /6	1181 ±142	273 ±33	.67
		Cont	$(3.03\pm.36)\times10^3$	4.06±.03	3.77± .14	4.3/6	55. /6	504 ± 60	116 ±14	.67
IV	0.93-1.13	ϕ	$(1.31\pm.16)\times10^3$	4.04±.30	4.01± .51	11. /6	3.9/6	197 ± 24	38 ± 5	.75
		Cont	393± 47	4.04±.30	4.01± .51	11. /6	3.9/6	59 ± 7	11.4± 1.4	.75
V	1.13-2.00	Cont	871±104	4.29±.65	4.47±1.29	2.1/4	3.9/4	91.2± 10.9	14.1± 1.7	.85

TABLE 10

RESONANCE CROSS SECTIONS $\begin{pmatrix} P \\ \pi^+ \\ \pi^- \end{pmatrix} + \begin{pmatrix} C \\ Be \end{pmatrix} \rightarrow \mu\mu+x$ IN NB PER NUCLEUS

Energy and Beam	Measured						Extrapolated					
	$x_F > 0.15$			$x_F > 0.07$			$x_F > 0.00$ Flat from 0.07**			$x_F > 0.00$ Exponential in $E(d\sigma/dx_F)$		
	ρ	ω	φ	ρ	ω	φ	ρ	ω	φ	ρ	ω	φ
225 GeV/c												
P	270 275*	478 487*	93 100*	657	1162	249	1059	1874	402	1295	2292	544
π^+	383 383*	678 678*	206 225*	747	1321	370	1099	1945	530	1182	2092	575
π^-	352 352*	623 623*	129 141*	674	1194	278	972	1721	410	1028	1820	459
150 GeV/c												
P	351	622	114	---	----	---	1278	2261	462	1650	2920	649
π^+	426	755	197	---	----	---	1131	2002	500	1275	2256	564
Errors	12%						15%					

*Resonance/total signal ratio used for these numbers was that obtained from the $x_F \geq 0.15$ data from the 150 GeV/c sample. Thus, using either ratio (for $x_F \geq 0.07$ or for $x_F \geq 0.15$) the 150 GeV/c cross sections are larger than the 225 GeV/c cross sections for $x_F \geq 0.15$. Pion ratios for the ρ-ω region are not changed due to larger ratio for the 150 GeV/c data.

**For the 225 GeV/c data the differential cross section $E(d\sigma/dx_F)$ was extrapolated flat to x_F=0.00 from x_F = 0.07. For the 150 GeV/c data the differential cross section $E(d/dx_F)$ was extrapolated exponentially to x_F = 0.07 from x_F = 0.15 and then extrapolated flat to x_F = 0.00.

TABLE 11

RESONANCE CROSS SECTIONS $\begin{pmatrix} P \\ \pi^+ \\ \pi^- \end{pmatrix} + \begin{pmatrix} C \\ Be \end{pmatrix} \rightarrow \mu\mu+X$ IN NB PER NUCLEON

Energy and Beam	Measurement						Measurement and Extrapolation					
	$x_F > 0.15$			$x_F > 0.07$			$x_F > 0.00$ Flat from 0.07			$x_F > 0.00$ Exponential in $E(d\sigma/dx_F)$		
	ρ	ω	ϕ	ρ	ω	ϕ	ρ	ω	ϕ	ρ	ω	ϕ
225 GeV/c												
P	52 52*	91 93*	14.4 15.5*	125	222	39	202	357	62	247	437	84
π^+	73 73*	129 129*	32 35*	142	252	57	210	371	82	225	399	89
π^-	67 67*	119 119*	20 22*	129	228	43	185	328	64	196	347	71
150 GeV/c												
P	81	144	22	---	---	--	295	522	89	381	674	125
π^+	98	174	38	---	---	--	261	462	96	294	521	108
Errors	12%						15%					

*See note on Table VIII. $A^{2/3}$ used to convert from nucleus to nucleon in Regions I-III; $A^{\cdot 75}$ in Region IV; and $A^{\cdot 85}$ in Region V.

TABLE 12

CONTINUUM CROSS SECTIONS $\begin{pmatrix} P \\ \pi^+ \\ \pi^- \end{pmatrix} + \begin{pmatrix} C \\ Be \end{pmatrix} \rightarrow \mu\mu+x$ IN NB PER NUCLEUS

Energy and Beam	Measured										Measured and Extrapolated									
	$x_F > 0.15$					$x_F > 0.07$					$x_F > 0.00$ Flat from 0.07					$x_F > 0.00$ Exponential in $E(d\sigma/dx_F)$				
Mass Region	I	II	III	IV	V	I	II	III	IV	V	I	II	III	IV	V	I	II	III	IV	V
225 GeV/c (C)																				
P	1220	502	310 296*	59 52*	35	4570	1670	754	158	102	9490	3060	1220	255	158	18200	4460	1490	345	226
π^+	1780	765	396 396*	87 68*	48	4840	1720	773	156	88	9650	2980	1140	224	132	13800	3670	1220	242	169
π^-	1550	604	359	64	53	4820	1580	687	139	108	9550	2670	990	205	154	13500	3170	1050	230	175
150 GeV/c (Be)																				
P	1990	781	376	60	53	---	--	---	---	---	14100	3930	1370	240	214	25300	5860	1770	337	315
π^+	2760	978	504	59	91	---	---	---	---	---	13700	2900	1340	150	218	19300	3320	1510	169	247
Errors	12%										15%									

*See footnote in Table VIII.

TABLE 13

CONTINUUM CROSS SECTIONS $\begin{pmatrix} p \\ \pi^+ \\ \pi^- \end{pmatrix} + \begin{pmatrix} C \\ Be \end{pmatrix} \rightarrow \mu\mu + x$ IN NB PER NUCLEON

Energy and Beam	Measured										Measured and Extrapolated									
	$x_F > 0.15$					$x_F > 0.07$					$x_F > 0.00$ Flat from 0.07					$x_F > 0.00$ Exponential in $E(d\sigma/dx_F)$				
Mass Region	I	II	III	IV	V	I	II	III	IV	V	I	II	III	IV	V	I	II	III	IV	V
225 GeV/c (C)																				
P	233	96	59 56*	9.1 8.1*	4.2	1050	386	174	24	12	2190	707	281	40	19.1	3470	850	284	53	27
π^+	340	146	76 76*	13.5 10.5*	5.7	1120	397	179	24	10.6	2230	687	263	35	15.9	3200	847	283	38	20
π^-	295	115	68 68*	9.9 8.1*	6.4	1110	365	159	22	13.1	2210	618	229	32	18.6	3120	732	242	36	21
150 GeV/c (Be)																				
P	460	180	87	11.5	8.2	---	---	---	--	---	3260	908	316	46	33	5840	1350	409	65	49
π^+	637	226	116	11.3	14.0	---	---	---	--	---	3160	670	309	29	34	4460	767	349	32	38
Errors	12%										15%									

*See footnote in Table IX.

Fig. 1.--The N1 beam line elements. A 400 GeV/c beam enters from the left and a 225 GeV/c beam exits at the right.

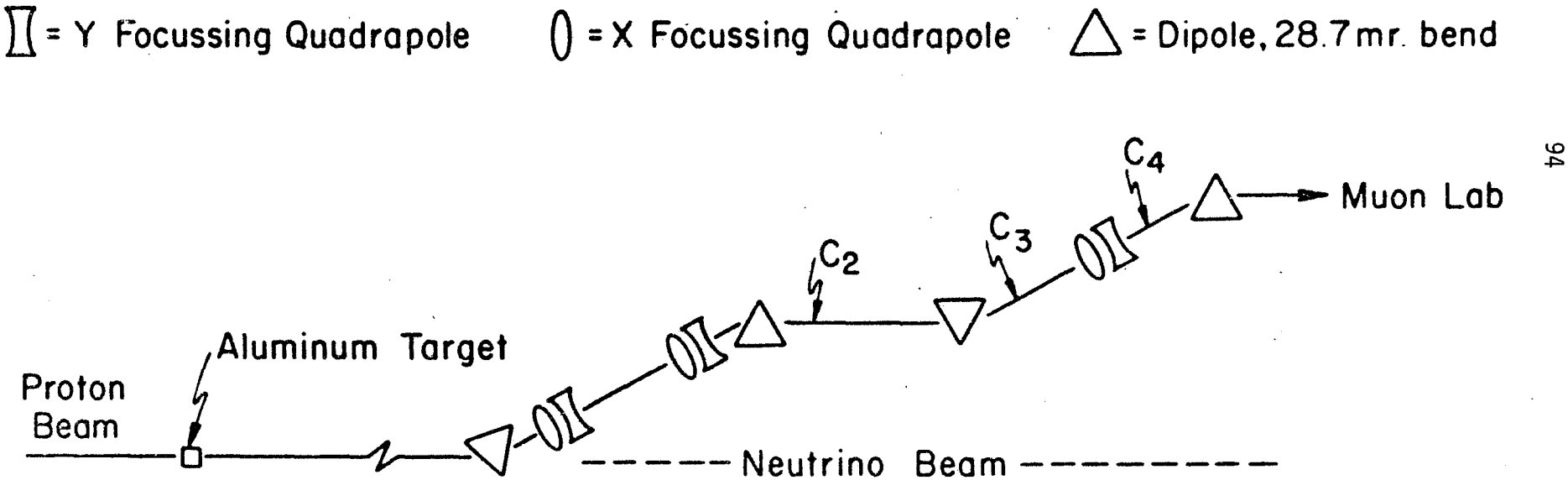
= Y Focussing Quadrapole
= X Focussing Quadrapole
= Dipole, 28.7 mr. bend
C4
Muon Lab
C3
C2
Aluminum Target
Proton Beam
Neutrino Beam

Fig. 2.--The Chicago Cyclotron Spectrometer as modified for low-mass dimuon data taking at 225 GeV/c.

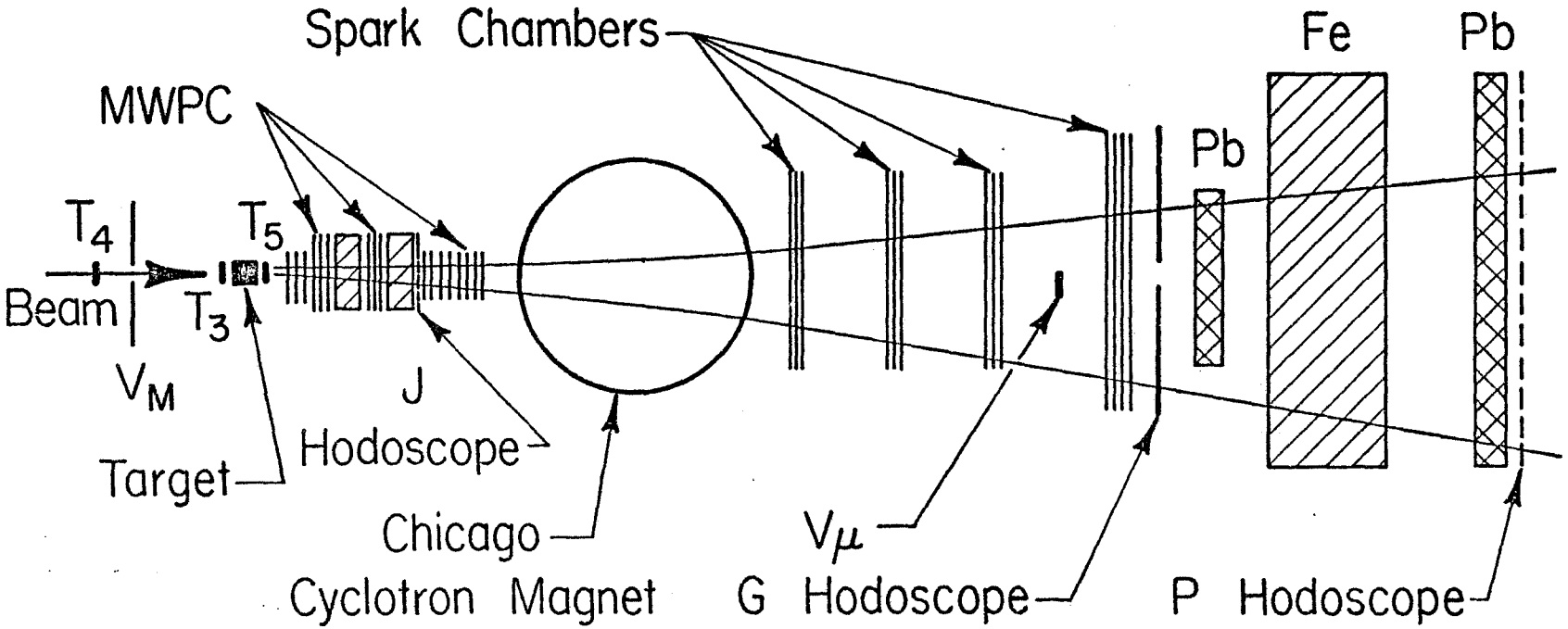
Spark Chambers
Fe
Pb
MWPC
Pb
T4
T5
Beam
T3
VM
J
Hodoscope
Target
Chicago
Cyclotron Magnet
Vμ
G Hodoscope
P Hodoscope

Fig. 3.--Cherenkov plateau curves for C_2. The curve (b) was plateaued at 194 GeV/c during the early portion of the run. When the incominb beam was changed to 225 GeV/c the pressure setting was scaled down by the beam setting and the curve (a) was rerun to check for errors. C_3 and C_4 were set similarly.

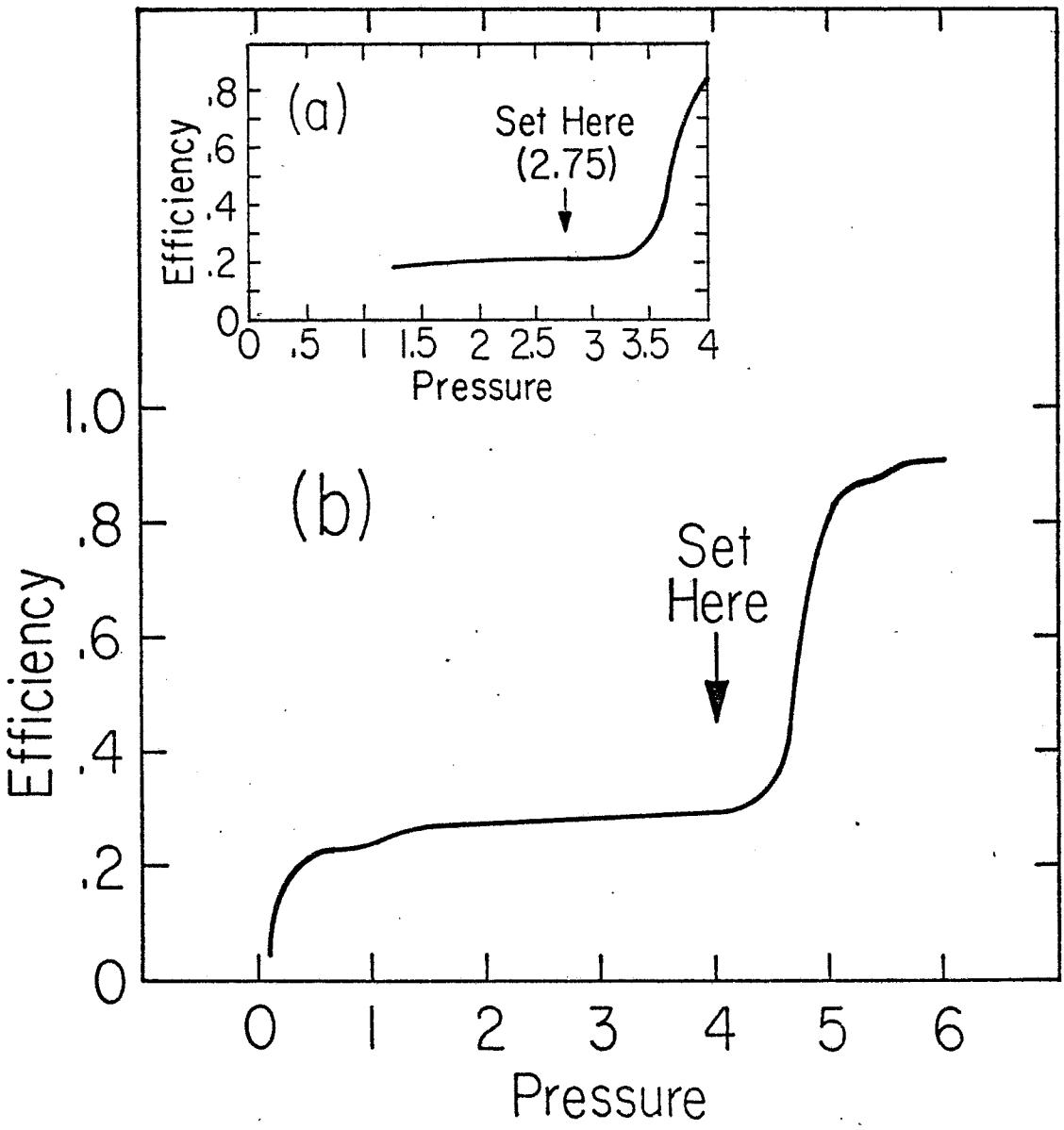
(a)
Set Here
(2.75)
Efficiency
Pressure
(b)
Set
Here
Efficiency
Pressure

Fig. 4.--The single particle pulse height spectra for T_3 and T_4. The multiparticle peaks were cut on the hardware level and hence do not appear in these plots. (a) T_3; (b) T_4.

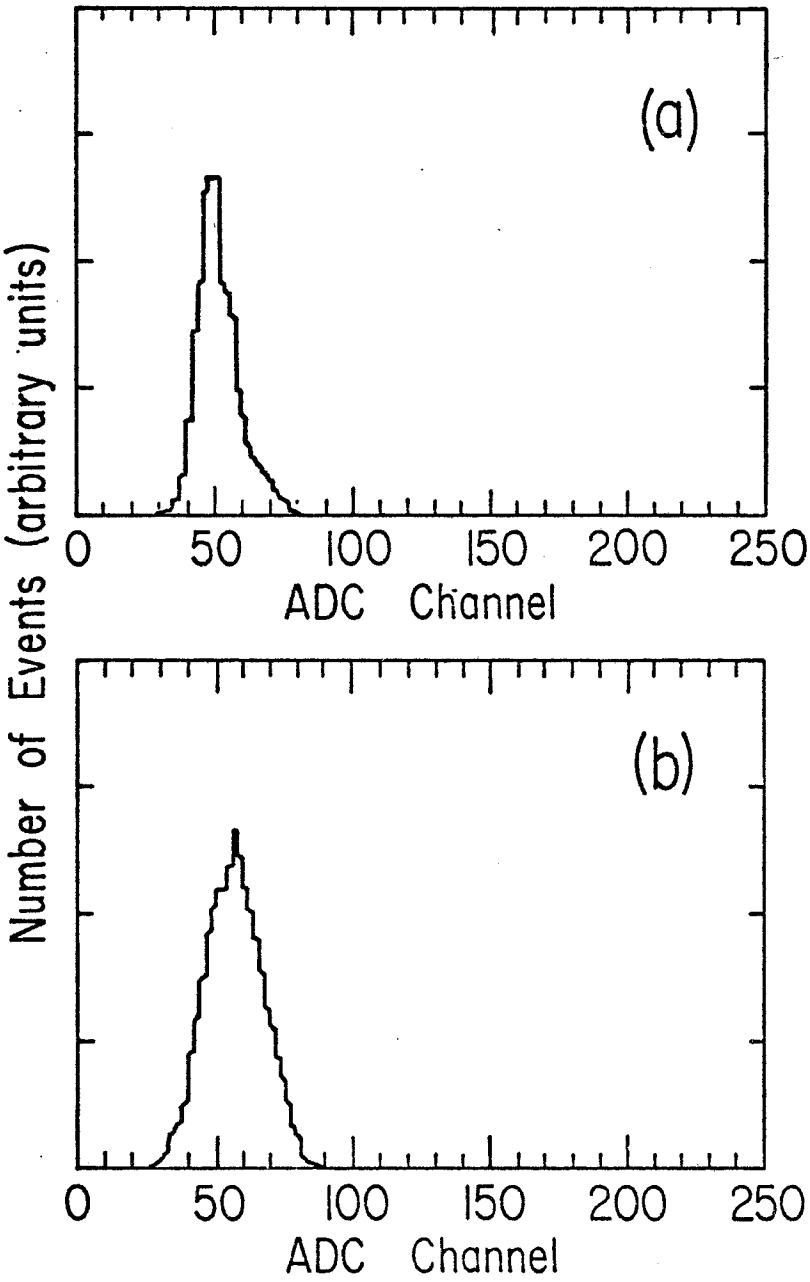
(a)
(b)
Number of Events (arbitrary units)
0
50
100
150
200
250
ADC Channel
ADC Channel

Fig. 5.--The pulse height spectrum for T_5, the interaction counter. (a) shows the spectrum for a muon test beam and shows the single minimum ionizing particle peak, (b) is the spectrum from the hadronic beam, with T_5 downstream of the target, (c) is the T_5 spectrum of the event trigger--the prescaled portion of the trigger can be clearly seen (see Fast Electronics).

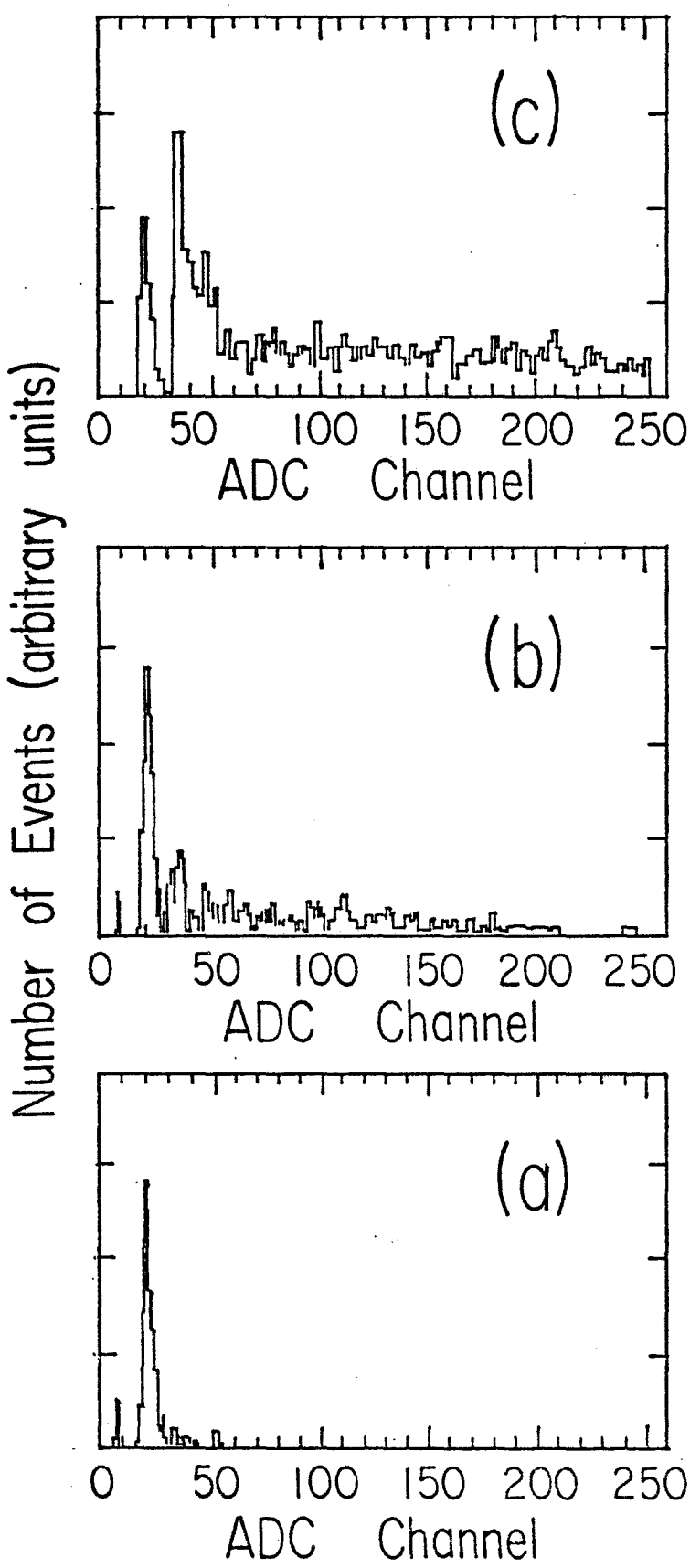
(c)
0 50 100 150 200 250
ADC Channel
(b)
0 50 100 150 200 250
ADC Channel
(a)
0 50 100 150 200 250
ADC Channel
Number of Events (arbitrary units)

Fig. 6.--A close-up of the "upstream" chambers used for the low mass analysis. Shown are the 30 cm, 55 cm and 80 cm MWPCs.

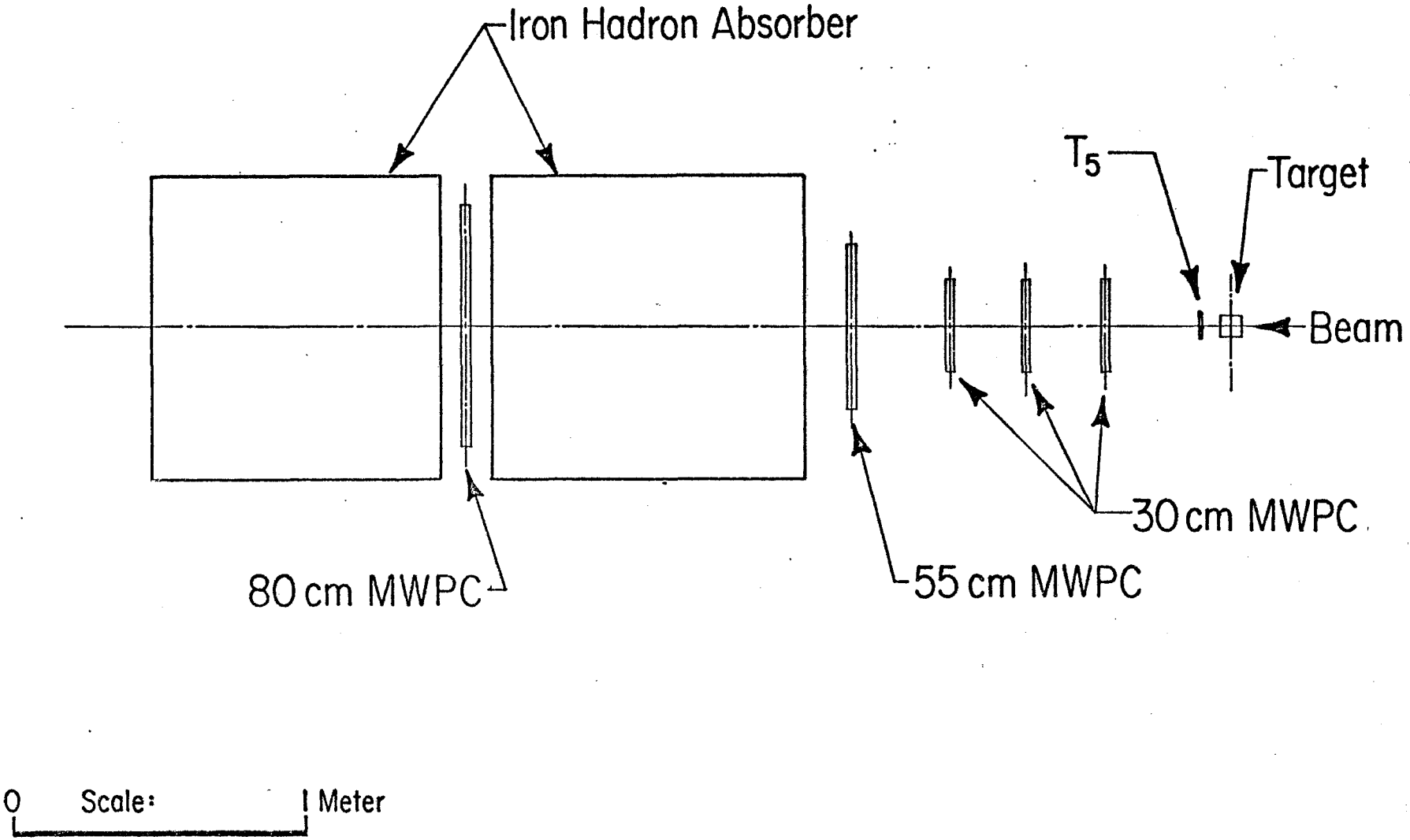
Iron Hadron Absorber
T5
Target
Beam
30 cm MWPC
80 cm MWPC
55 cm MWPC
0
Scale:
1 Meter

Fig. 7.--Arrangement and sizes of the J hodoscope elements.

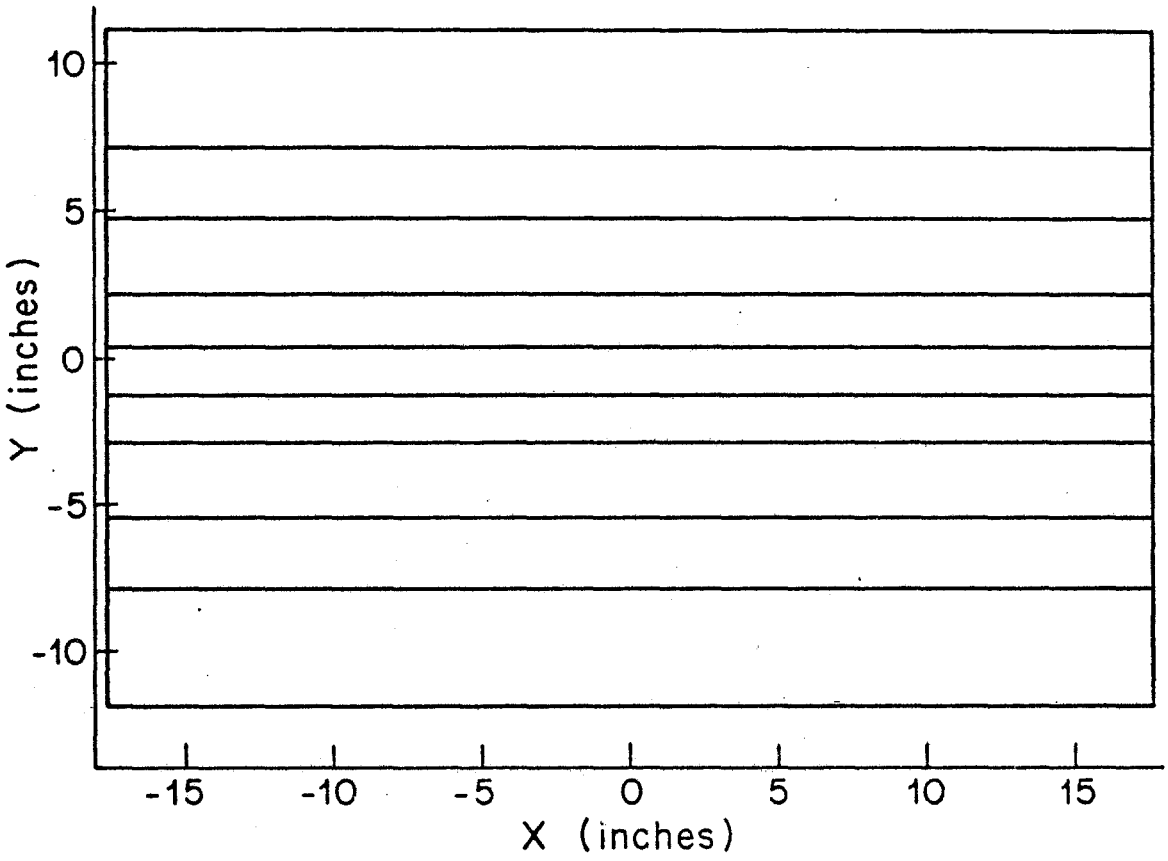
10
5
0
-5
-10
Y (inches)
-15
-10
-5
0
5
10
15
X (inches)

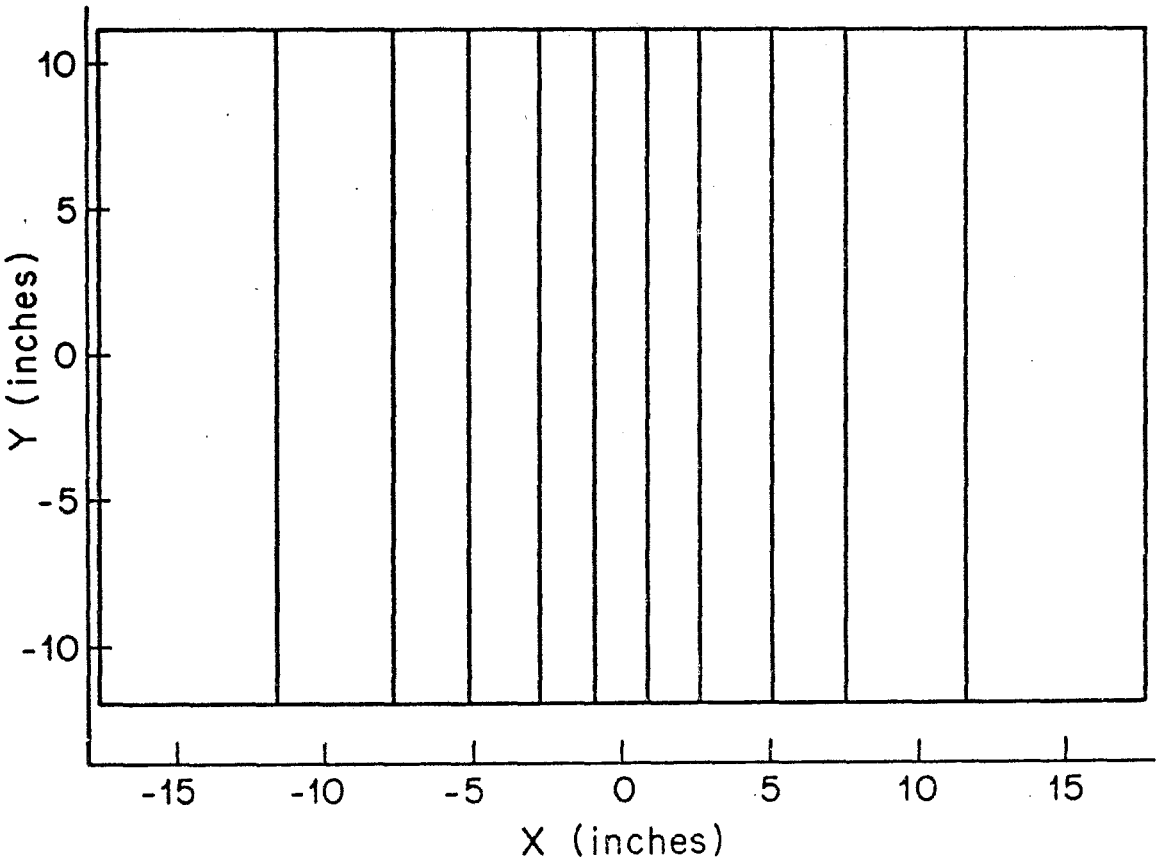
10
5
0
-5
-10
Y (inches)
-15
-10
-5
0
5
10
15
X (inches)

Fig. 8.--Arrangement and sizes of the P hodoscope elements.

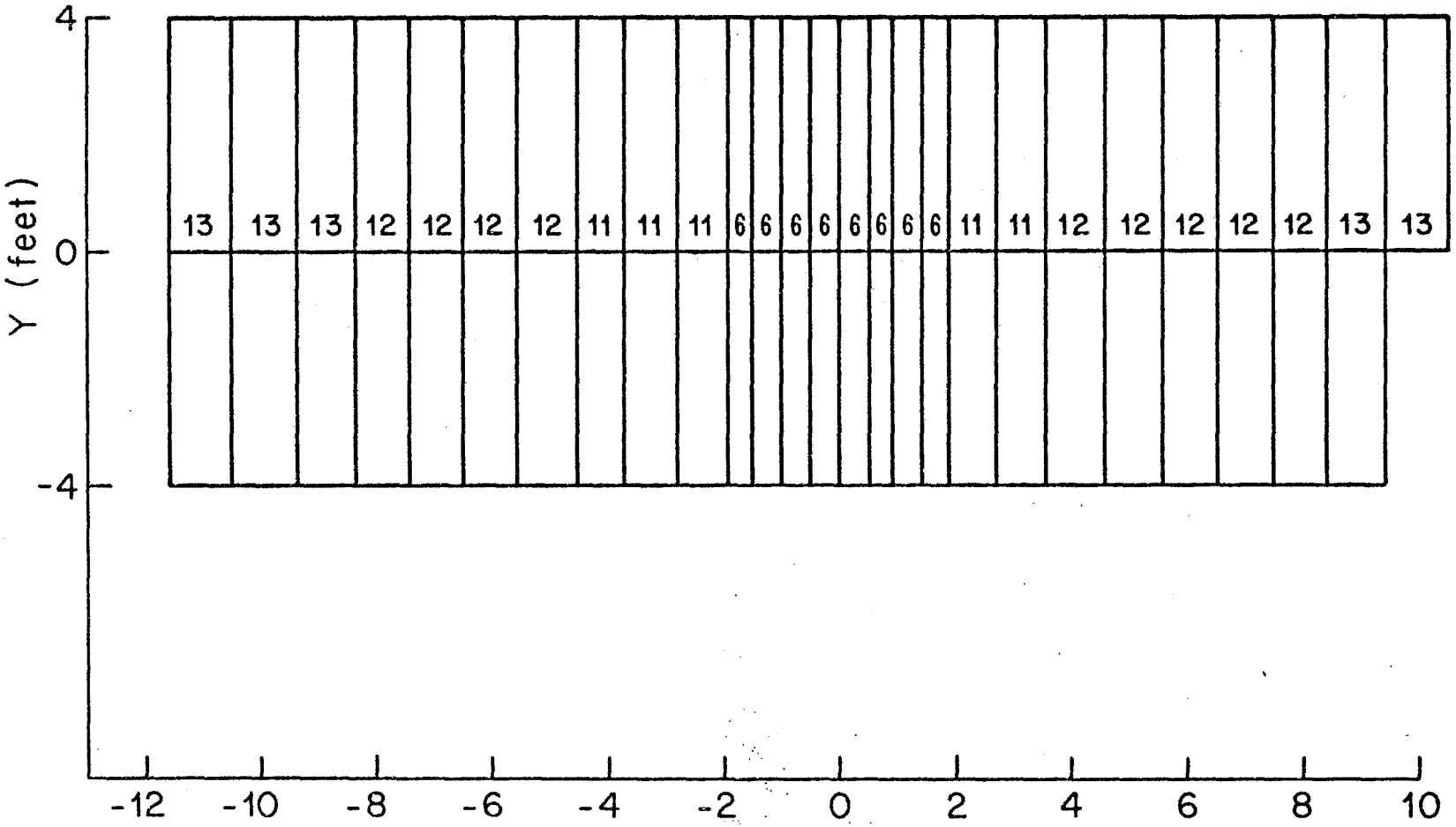

The P Hodoscope

Fig. 9.--Ratio of Monte Carlo hits to real data hits in the P hodoscope versus hodoscope element number.

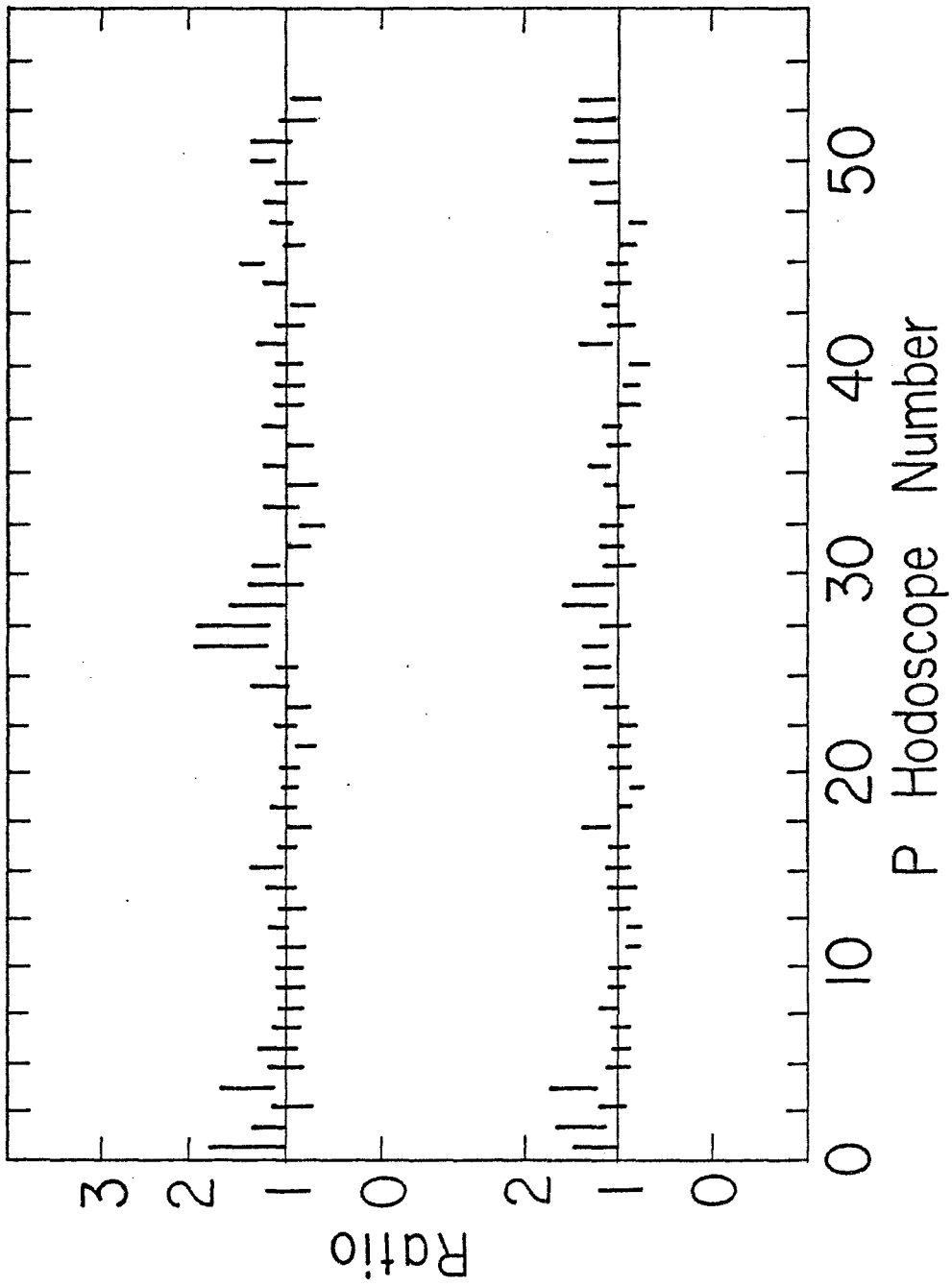
Ratio
3
2
1
0
2
1
0
0
10
20
30
40
50
P Hodoscope Number

Fig. 10.--The logic of the fast electronics.

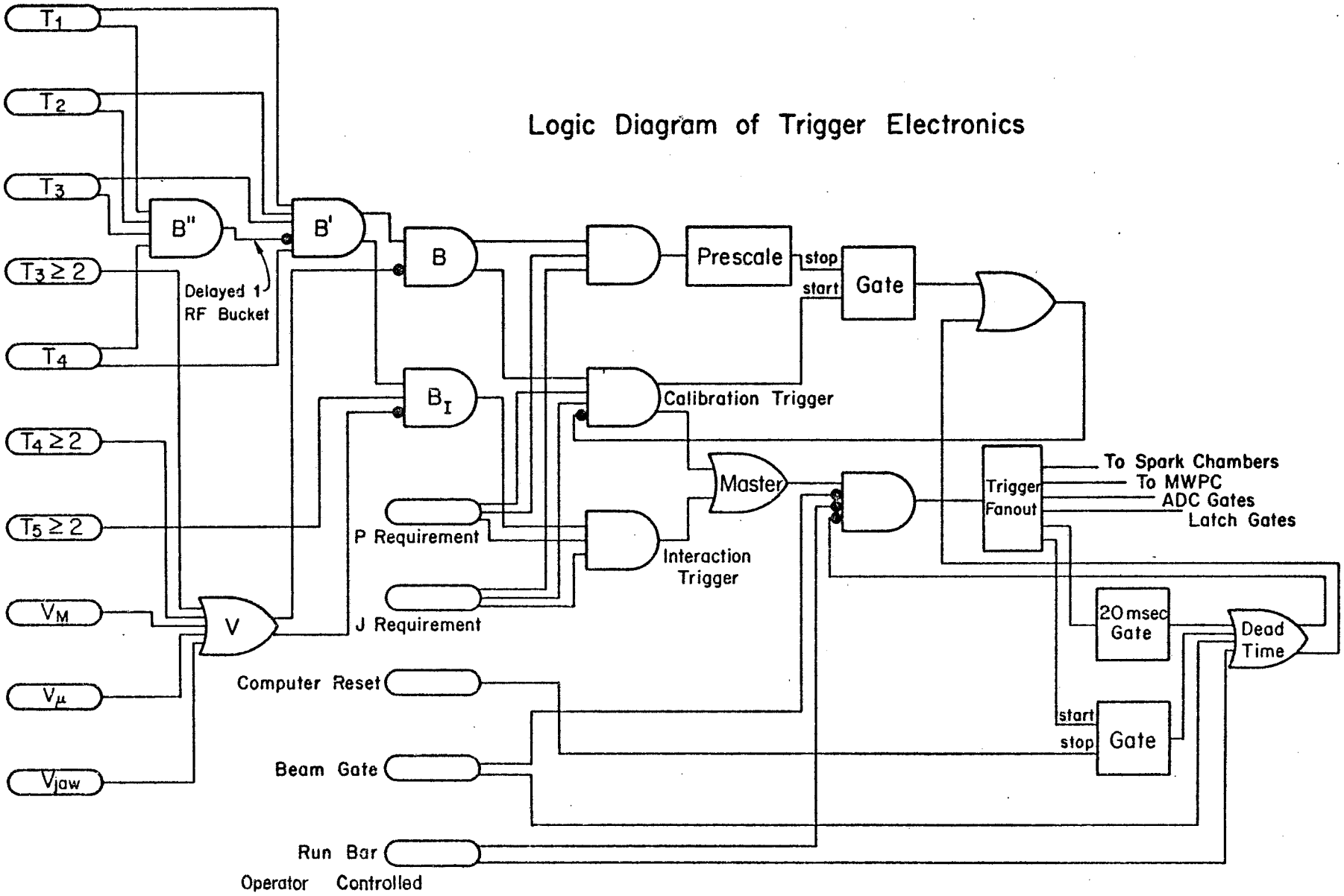
Logic Diagram of Trigger Electronics
T1
T2
T3
T3 ≥ 2
T4
T4 ≥ 2
T5 ≥ 2
VM
Vμ
Vjaw
B"
B'
B
BI
V
Delayed 1 RF Bucket
P Requirement
J Requirement
Computer Reset
Beam Gate
Run Bar
Operator Controlled
Prescale
stop
start
Gate
Calibration Trigger
Master
Interaction Trigger
Trigger Fanout
To Spark Chambers
To MWPC
ADC Gates
Latch Gates
20 msec Gate
Dead Time
start
stop
Gate

Fig. 11.--The difference in slopes measured in radians in y, determined upstream and downstream of the Chicago Cyclotron magnet.

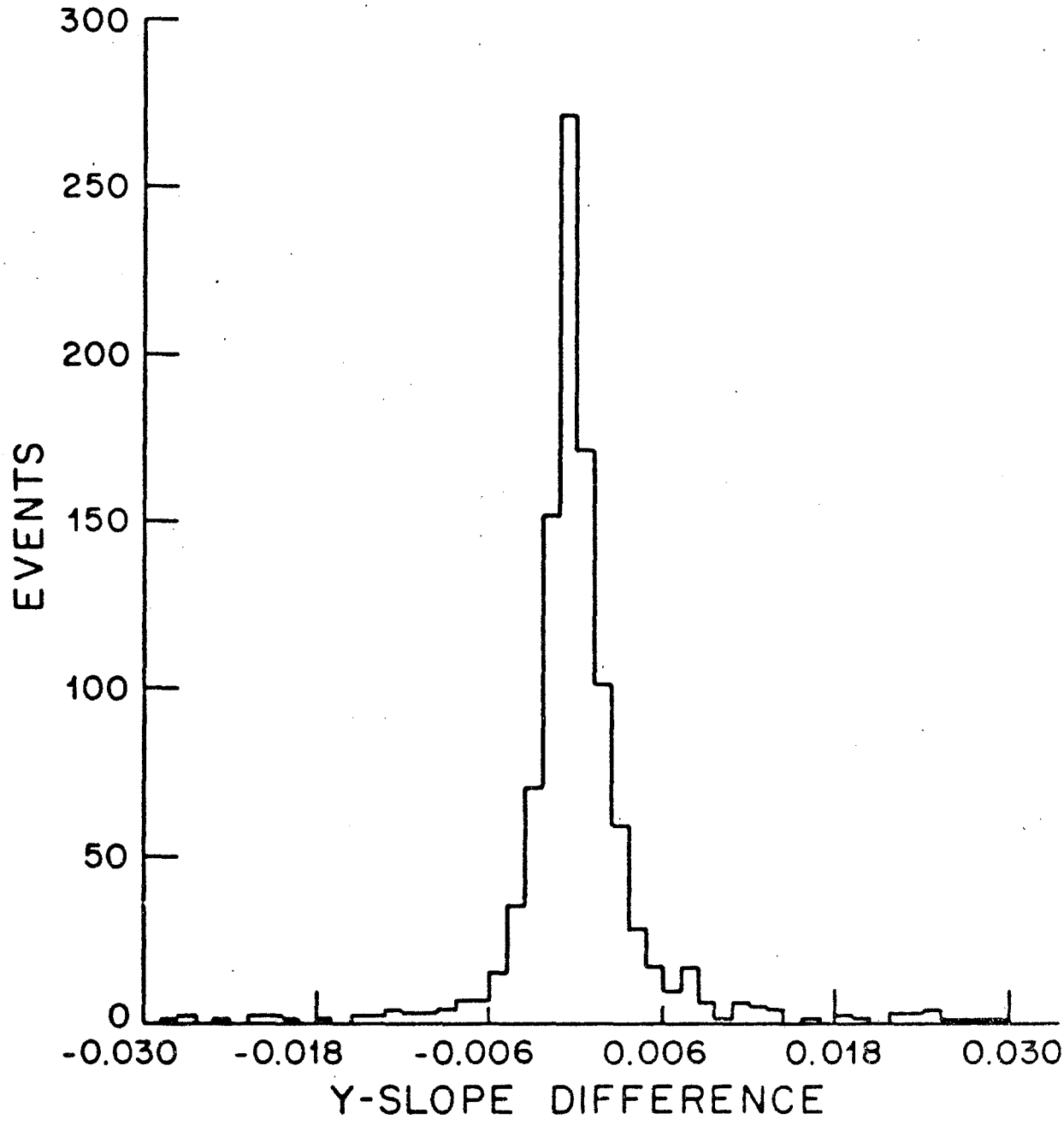
300
250
200
150
100
50
0
EVENTS
-0.030
-0.018
-0.006
0.006
0.018
0.030
Y-SLOPE DIFFERENCE

Fig. 12.--The difference in intercepts measured in mm in y, determined upstream and downstream of the Chicago Cyclotron magnet.

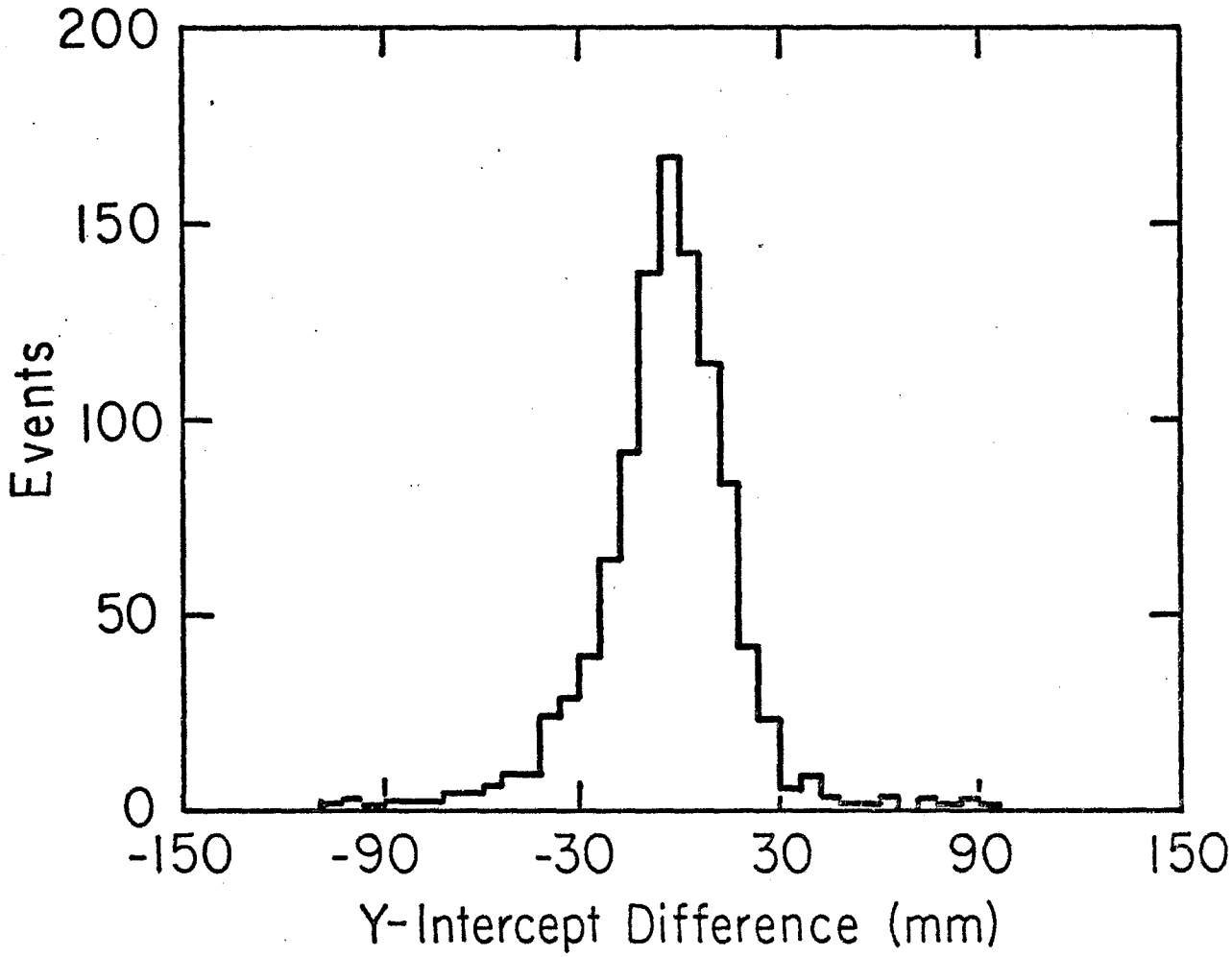
200
150
100
50
0
Events
-150
-90
-30
30
90
150
Y-Intercept Difference (mm)

Fig. 13.--The difference in impact parameters determined upstream and downstream of the Chicago Cyclotron magnet as measured in millimeters.

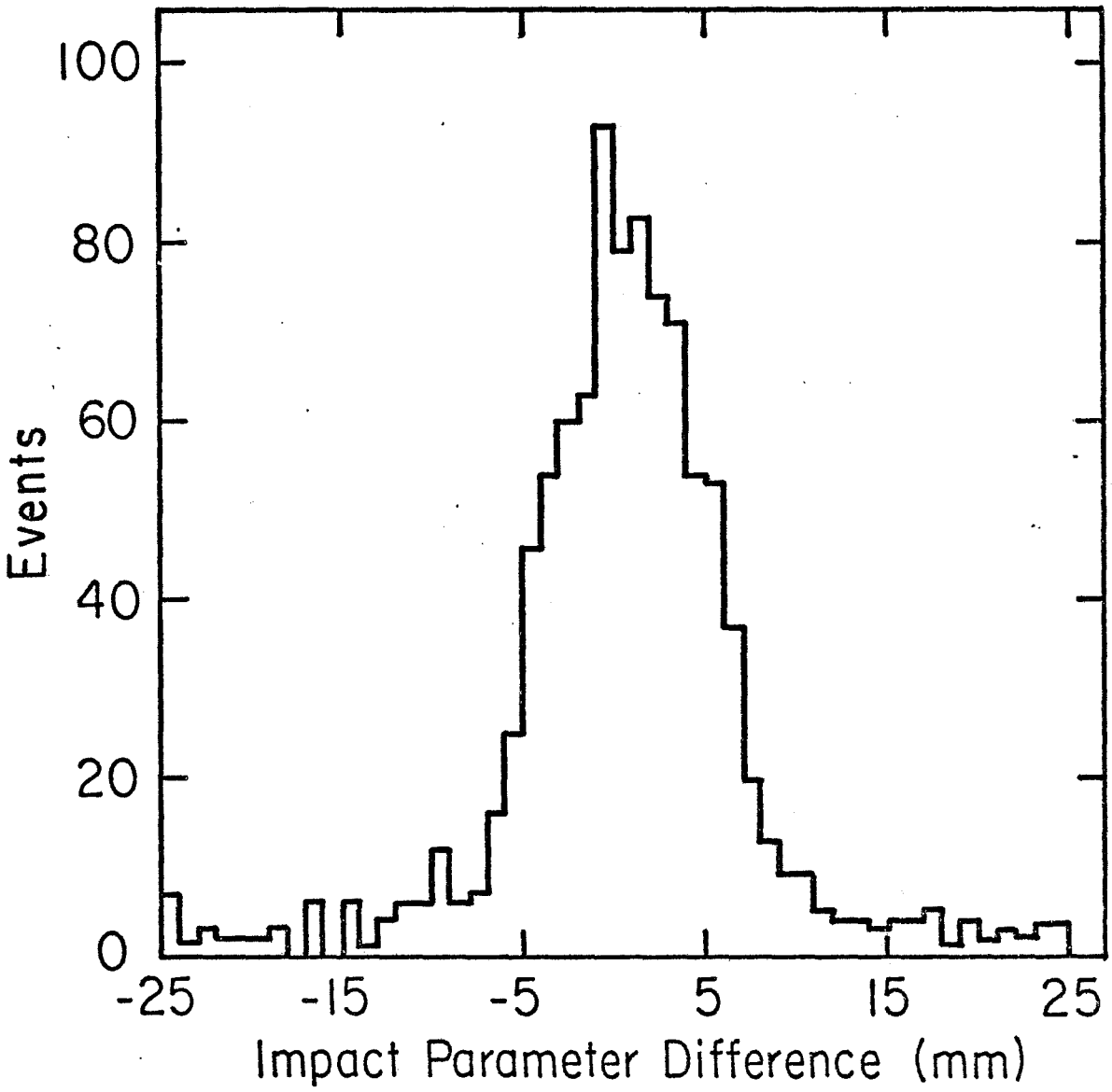
100
80
60
40
20
0
Events
-25
-15
-5
5
15
25
Impact Parameter Difference (mm)

Fig. 14.--The J' trigger rates divided by beam rates, normalized to unity.

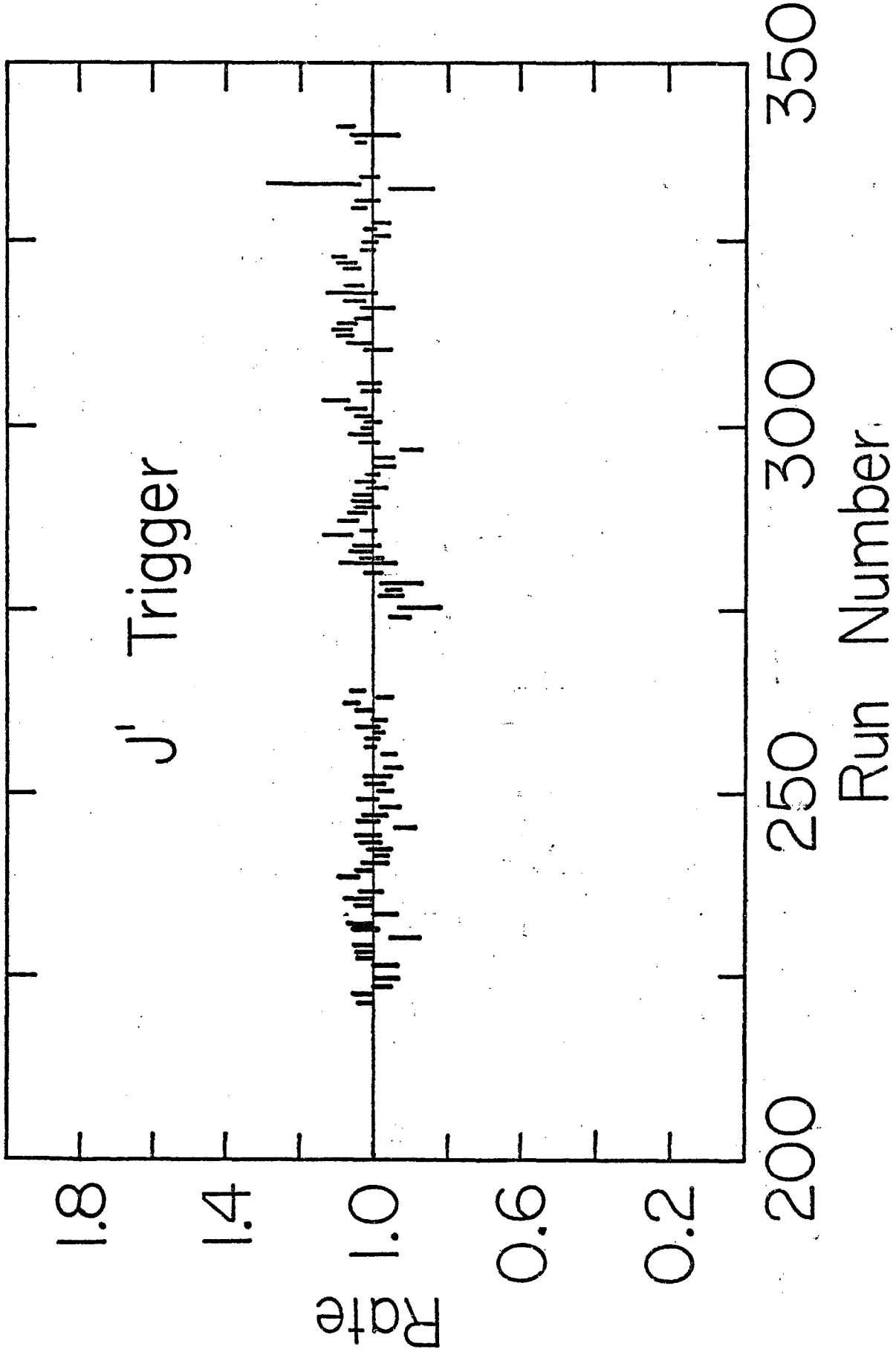
J' Trigger
Rate
1.8
1.4
1.0
0.6
0.2
200
250
300
350
Run Number

Fig. 15.--The calculated resolution in z of the vertex analysis.

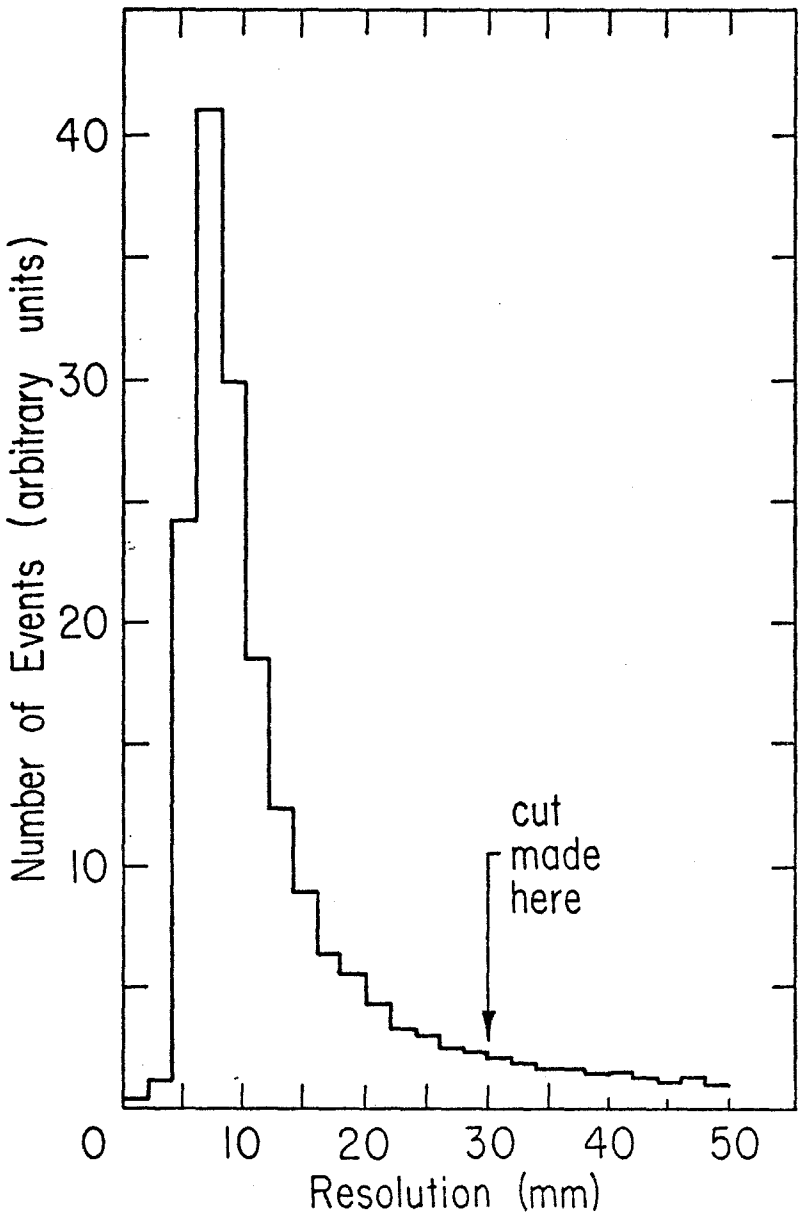
Number of Events (arbitrary units)
40
30
20
10
0
10
20
30
40
50
Resolution (mm)
cut
made
here

Fig. 16.--A diagram of possible secondary production in the target and the extrapolated tracks of all the particles.

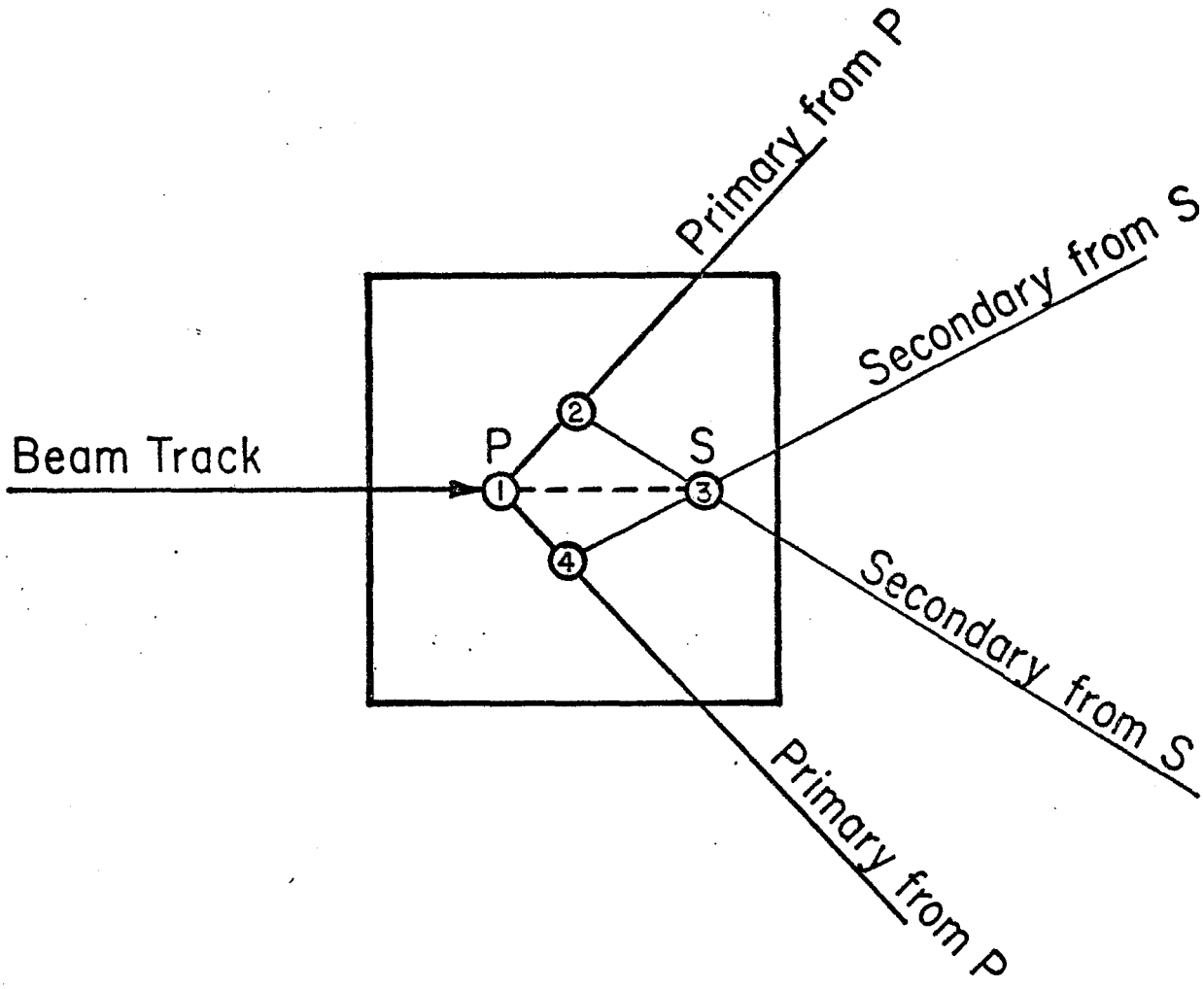
Primary from P
Secondary from S
Beam Track
P
S
1
2
3
4
Secondary from S
Primary from P

Fig. 17.--The distribution in z of the final reconstructed vertex positions. All z distribution plots are for the large C target.

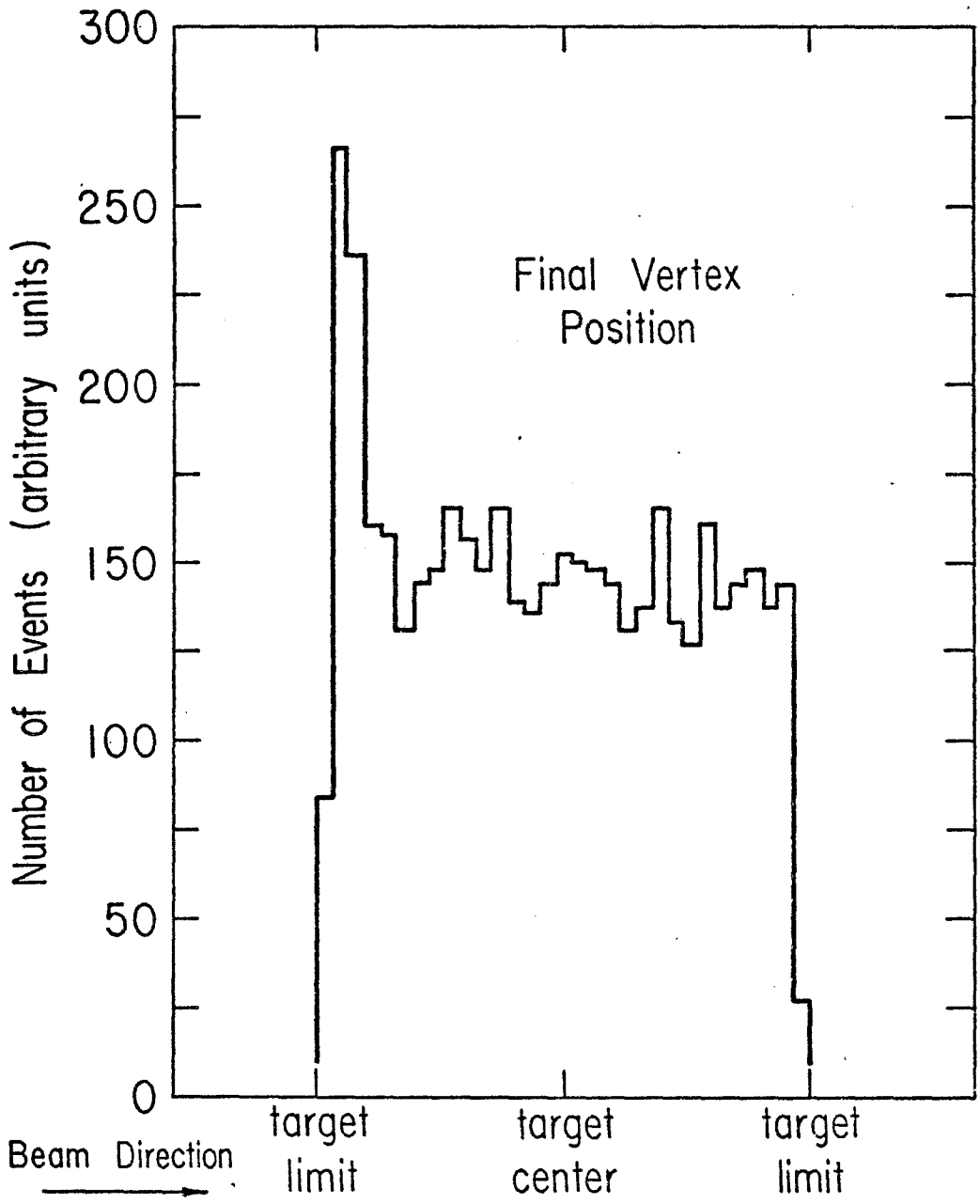
300
250
200
150
100
50
0
Number of Events (arbitrary units)
Final Vertex
Position
Beam Direction
target
limit
target
center
target
limit

Fig. 18.--The distribution in z of the Monte Carloed vertex position, assuming the resolution distribution shown earlier.

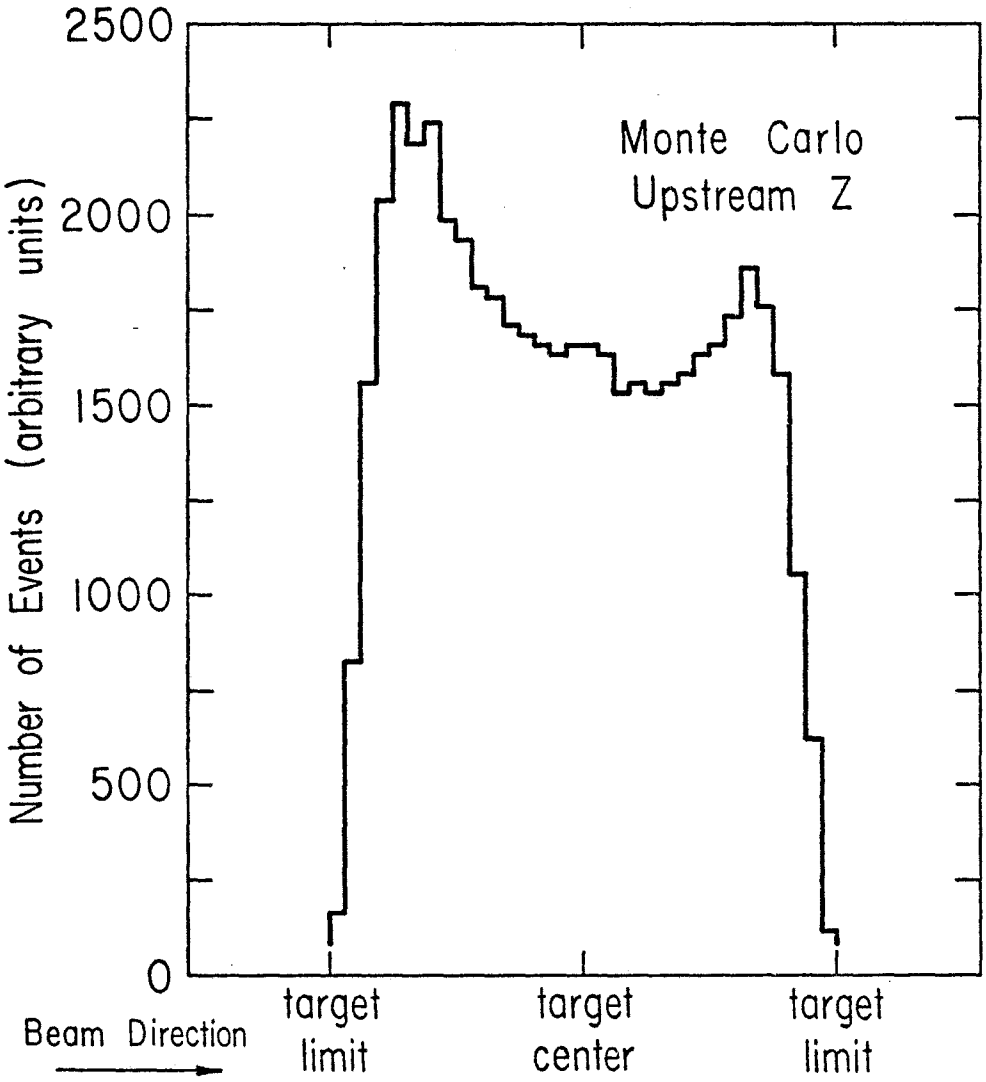
2500
2000
1500
1000
500
0
Number of Events (arbitrary units)
Monte Carlo
Upstream Z
Beam Direction
target
limit
target
center
target
limit

Fig. 19.--The distribution in z of the most downstream vertex positions. Vertices have not been "pulled back" into the target limits for the two "most downstream" plots.

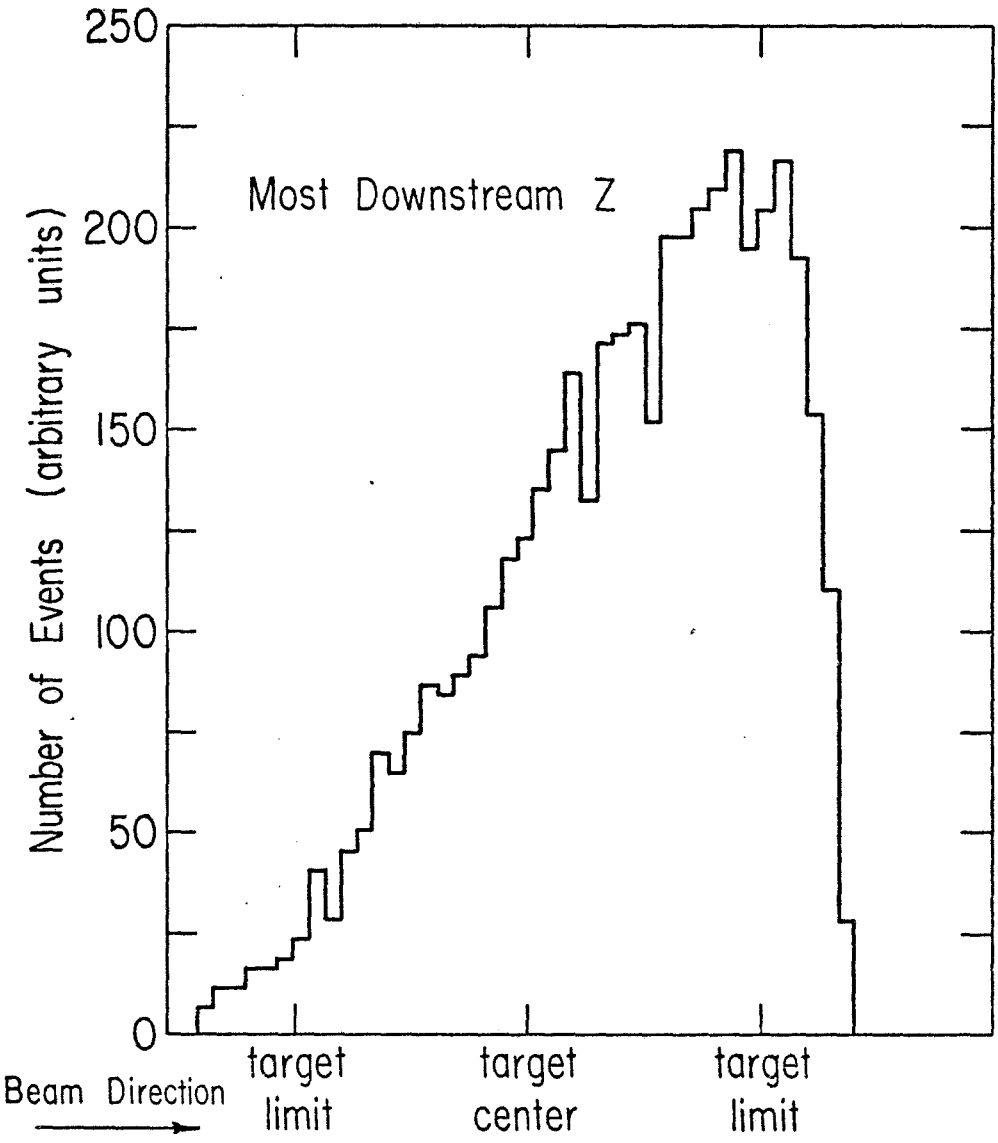
250
200
150
100
50
0
Number of Events (arbitrary units)
Most Downstream Z
Beam Direction
target limit
target center
target limit

Fig. 20.--The distribution of the Monte Carloed most downstream possible vertex position. The resolution distribution shown earlier is assumed, as is a charged particle multiplicity of 8.

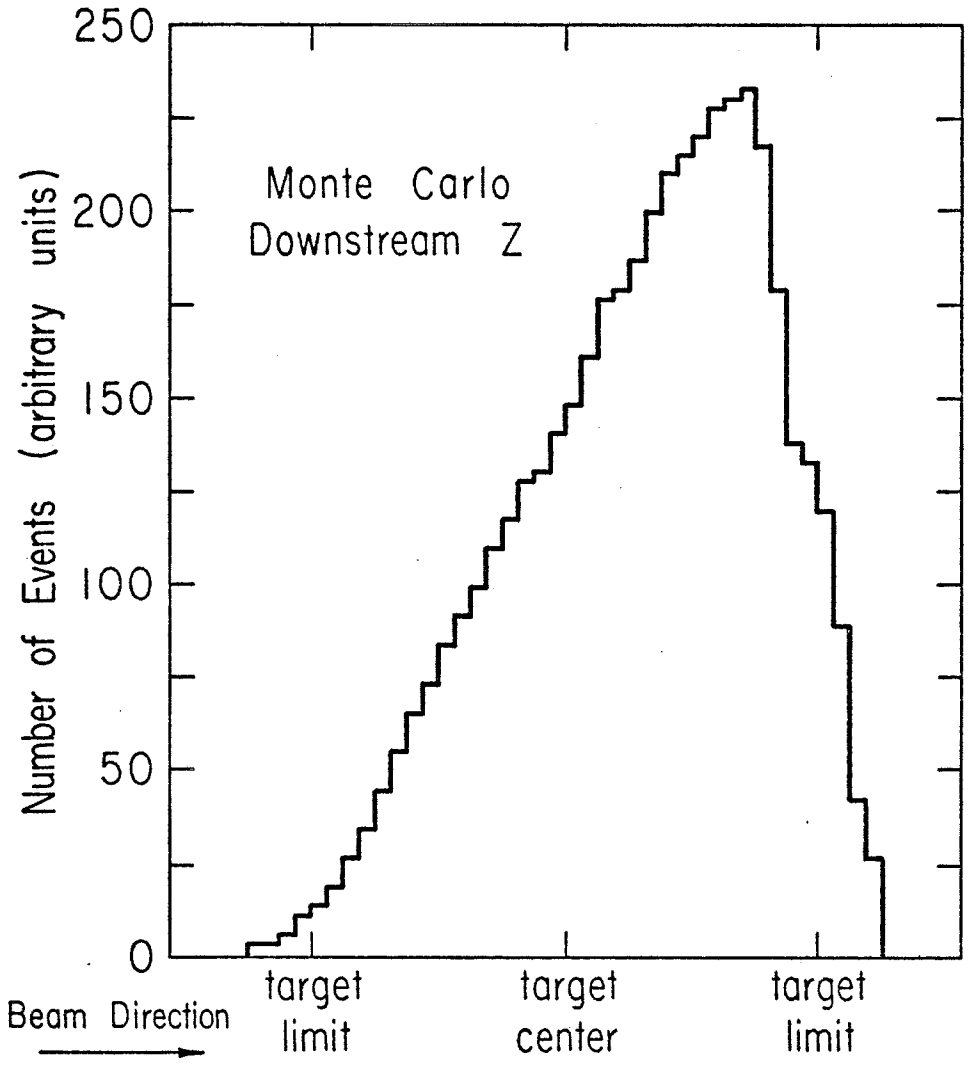
250
200
150
100
50
0
Number of Events (arbitrary units)
Monte Carlo
Downstream Z
Beam Direction
target
limit
target
center
target
limit

Fig. 21.--The ratio of cross sections obtained by the analysis not using the low mass analysis of the long target to the short target as a function of x_F, at the ρ- ω. A ratio greater than one at low x_F would indicate secondary production in the target.

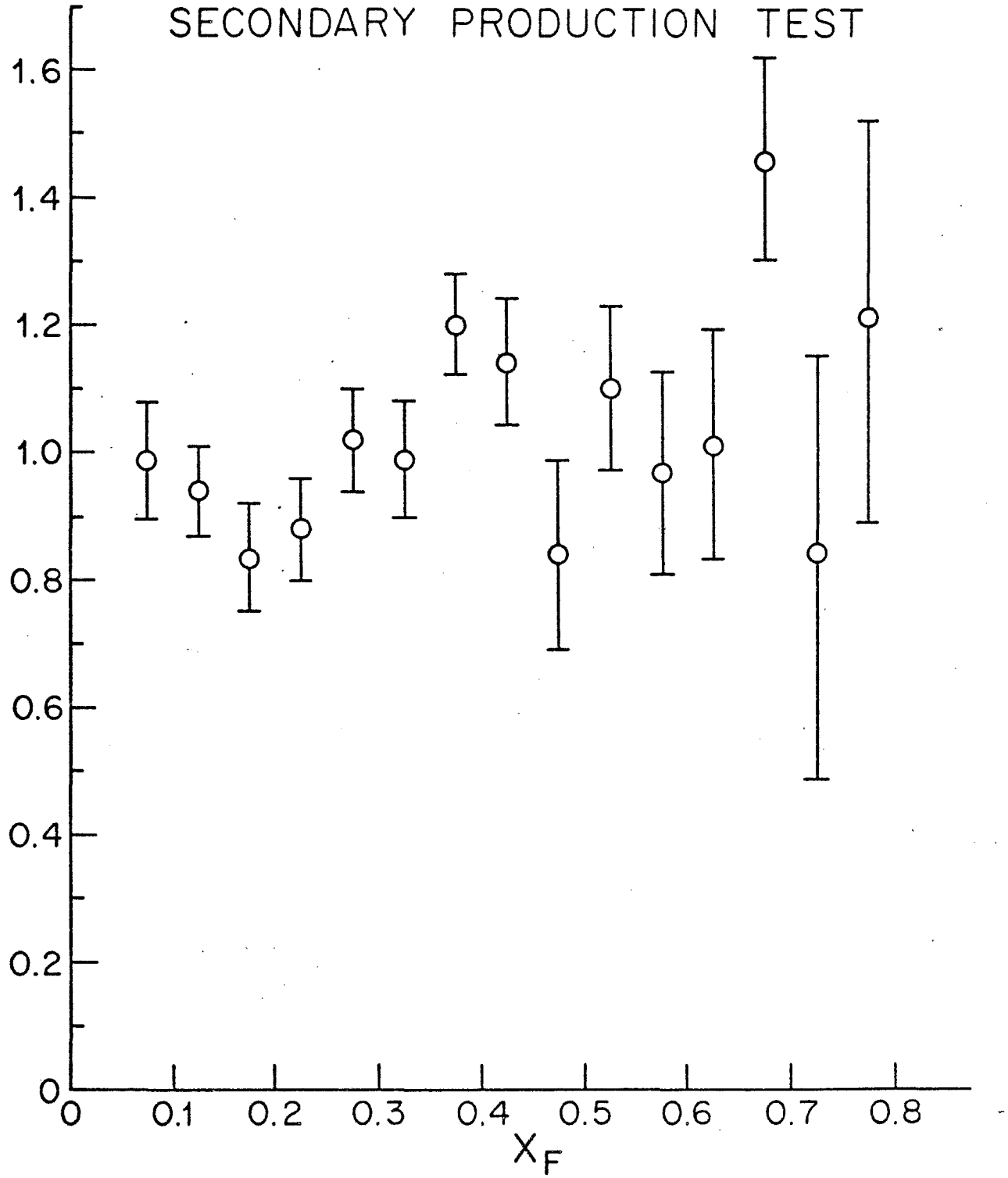
SECONDARY PRODUCTION TEST
1.6
1.4
1.2
1.0
0.8
0.6
0.4
0.2
0
0
0.1
0.2
0.3
0.4
0.5
0.6
0.7
0.8
X_F

Fig. 22.--An example of the computer analysis result of the vertex chamber analysis, in both x and y views. Symbols explained in text.

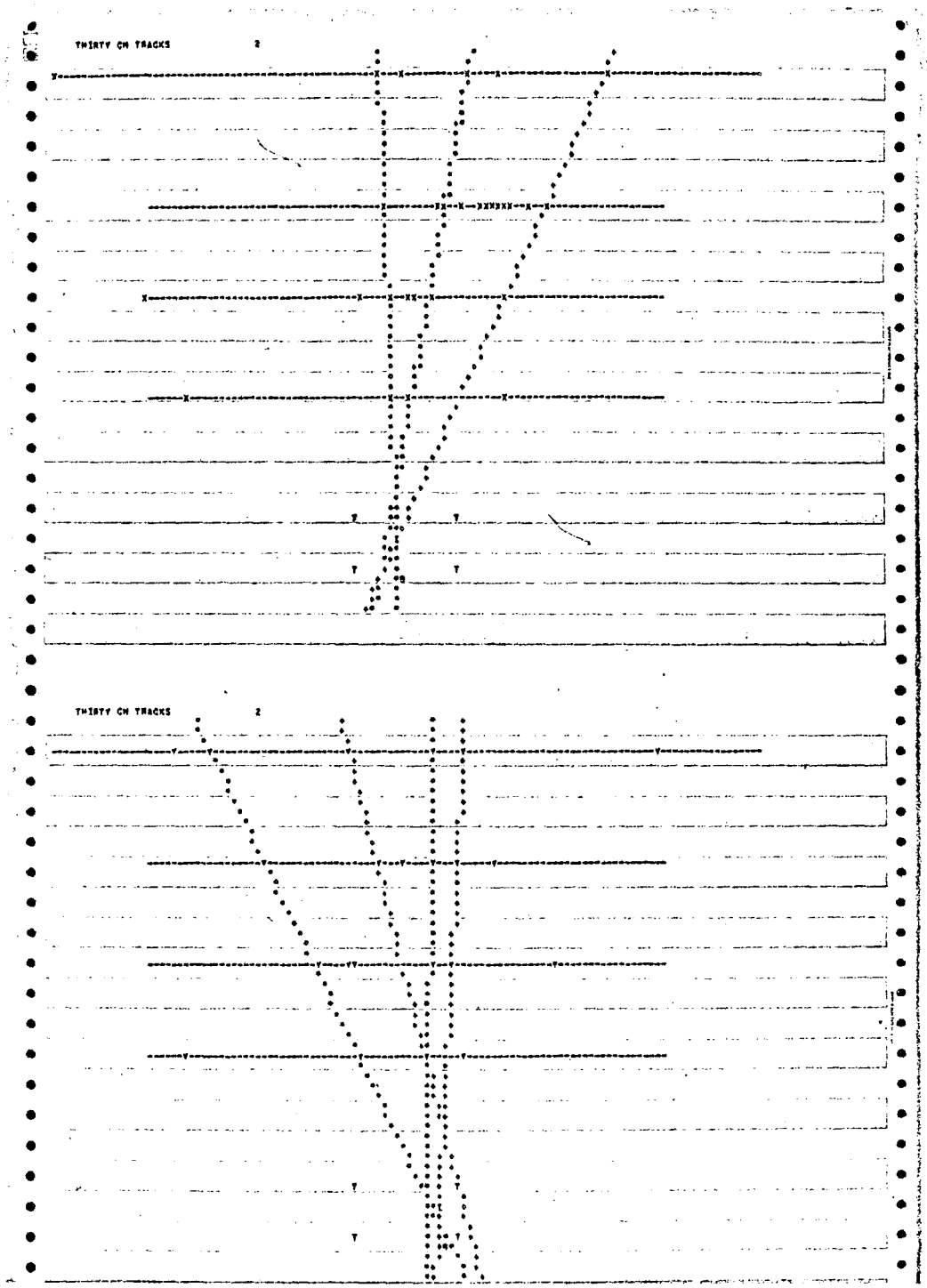
THIRTY CM TRACKS
2
THIRTY CM TRACKS
2

Fig. 23.--A diagram of the upstream apparatus, along with some of the variables used in the mass calculations.

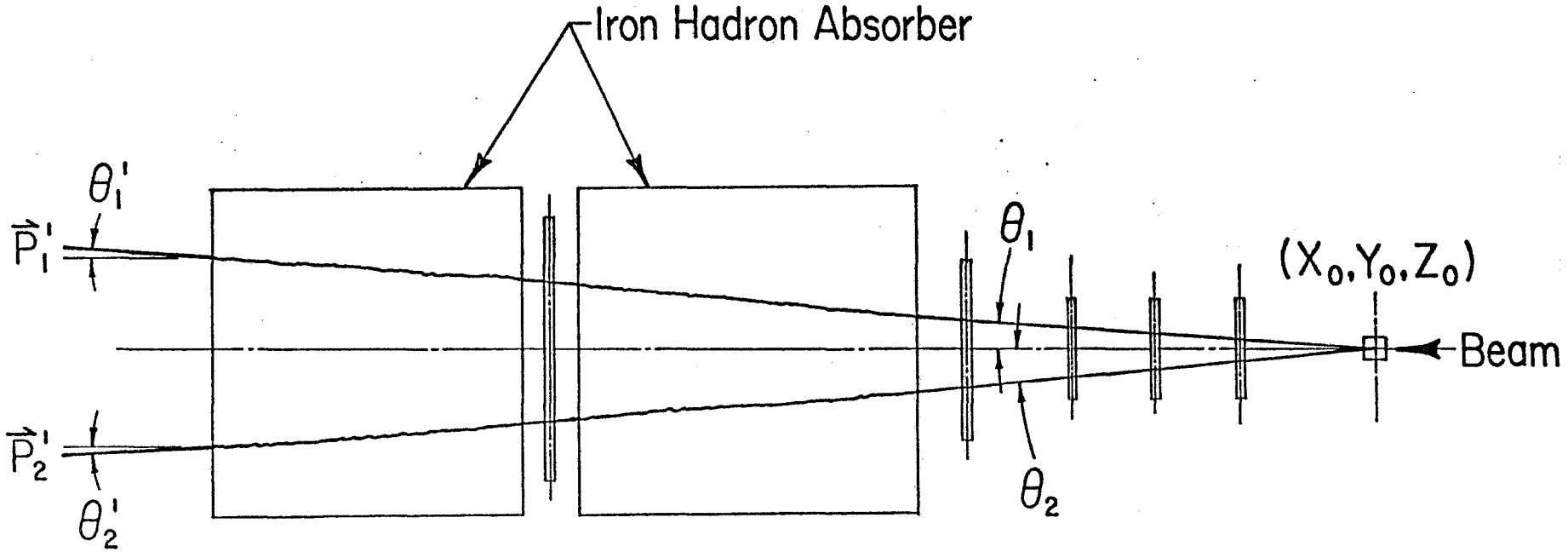

0 Scale: 1 Meter

Fig. 24.--A plot of the distance from extrapolated track positions to all hits in the 55 cm chamber. The distance is weighted by the inverse of the phase space available to the hits (which increases linearly with distance from the track). The number of events is weighted by the inverse of the number of events possible at that distance (which increases linearly with distance). Thus a hit, 5 mm away from a track with associated momentum of 20 GeV/c will register at 1.1 on the plot. The distance scales roughly with inverse of the momentum (a track with double the momentum but still 5 mm from a hit will appear at half the previous distance). Superimposed on the plot is a plot of the distances using the track positions and momenta from the previous event and the hits from the current event ("previous event analysis"). Above the uncorrelated signal distance is thus seen a strong real signal.

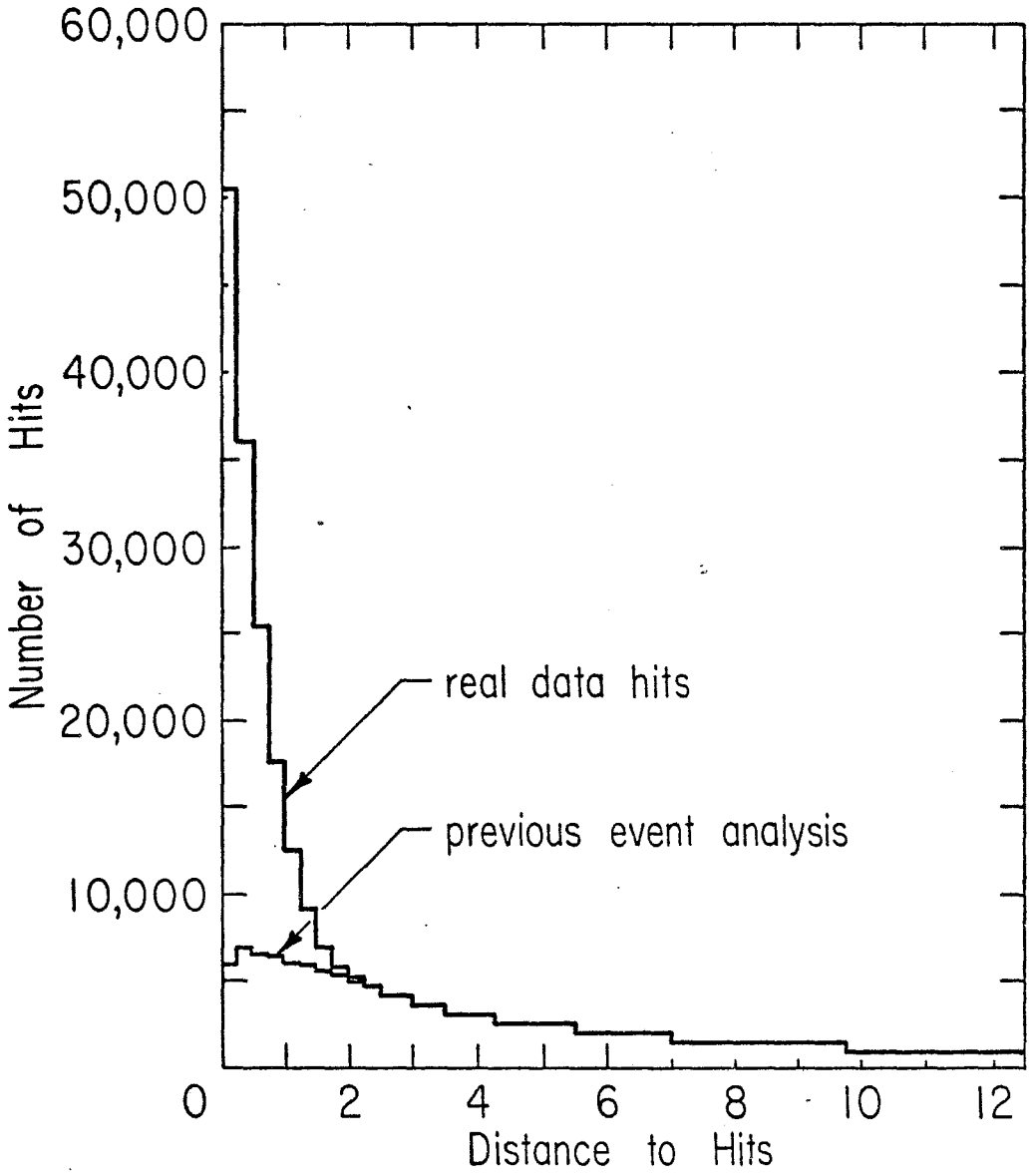
60,000
50,000
40,000
30,000
20,000
10,000
Number of Hits
real data hits
previous event analysis
0
2
4
6
8
10
12
Distance to Hits

Fig. 25.--The calculated masses associated with the analyses from the "previous event" and real-event analyses.

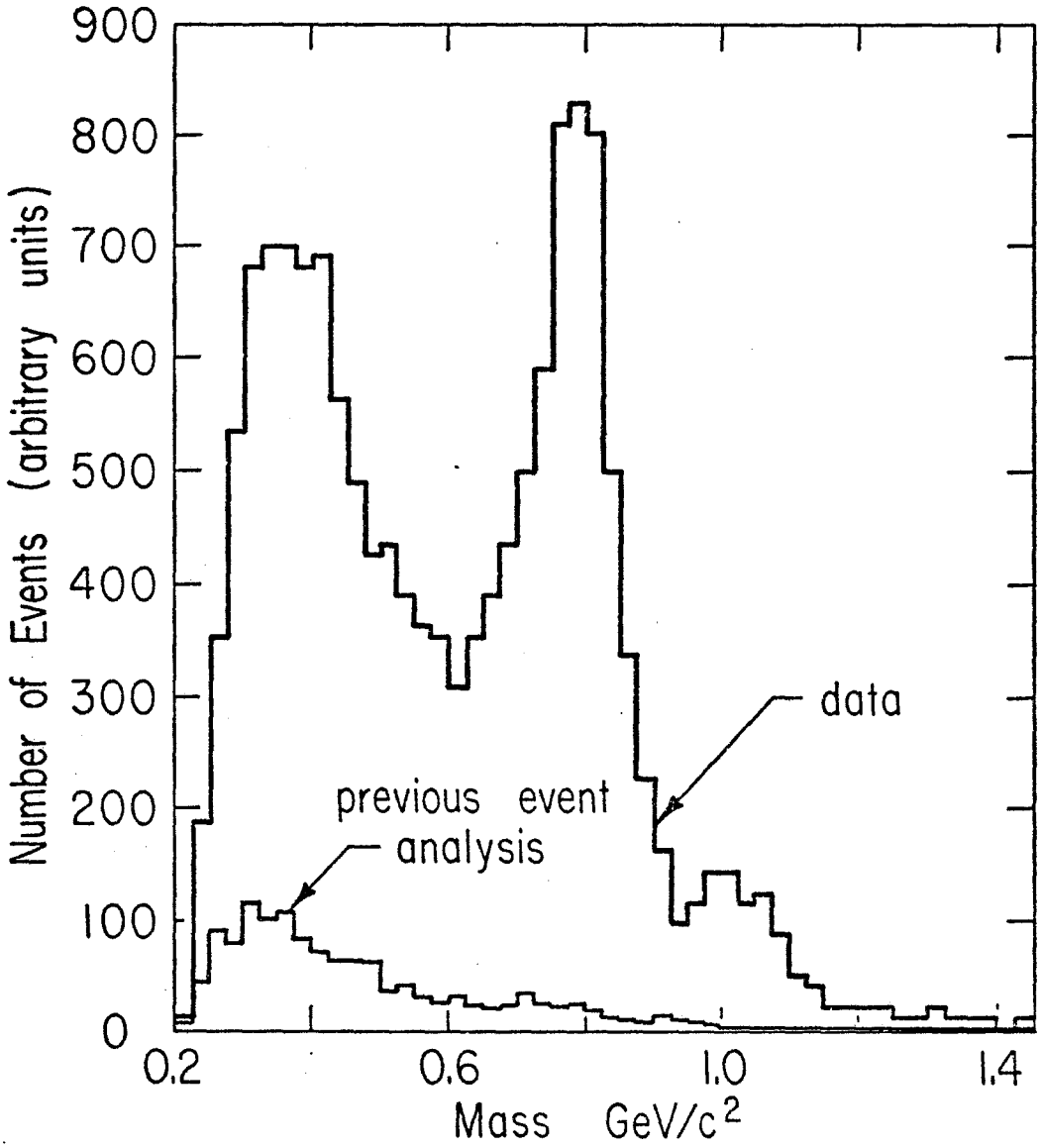
900
800
700
600
500
400
300
200
100
0
Number of Events (arbitrary units)
0.2
0.6
1.0
1.4
Mass GeV/c²
data
previous event
analysis

Fig. 26.--The "fit" mass--the mass calculated without the low mass analysis. The data sample used in the following two figures is identical to this sample.

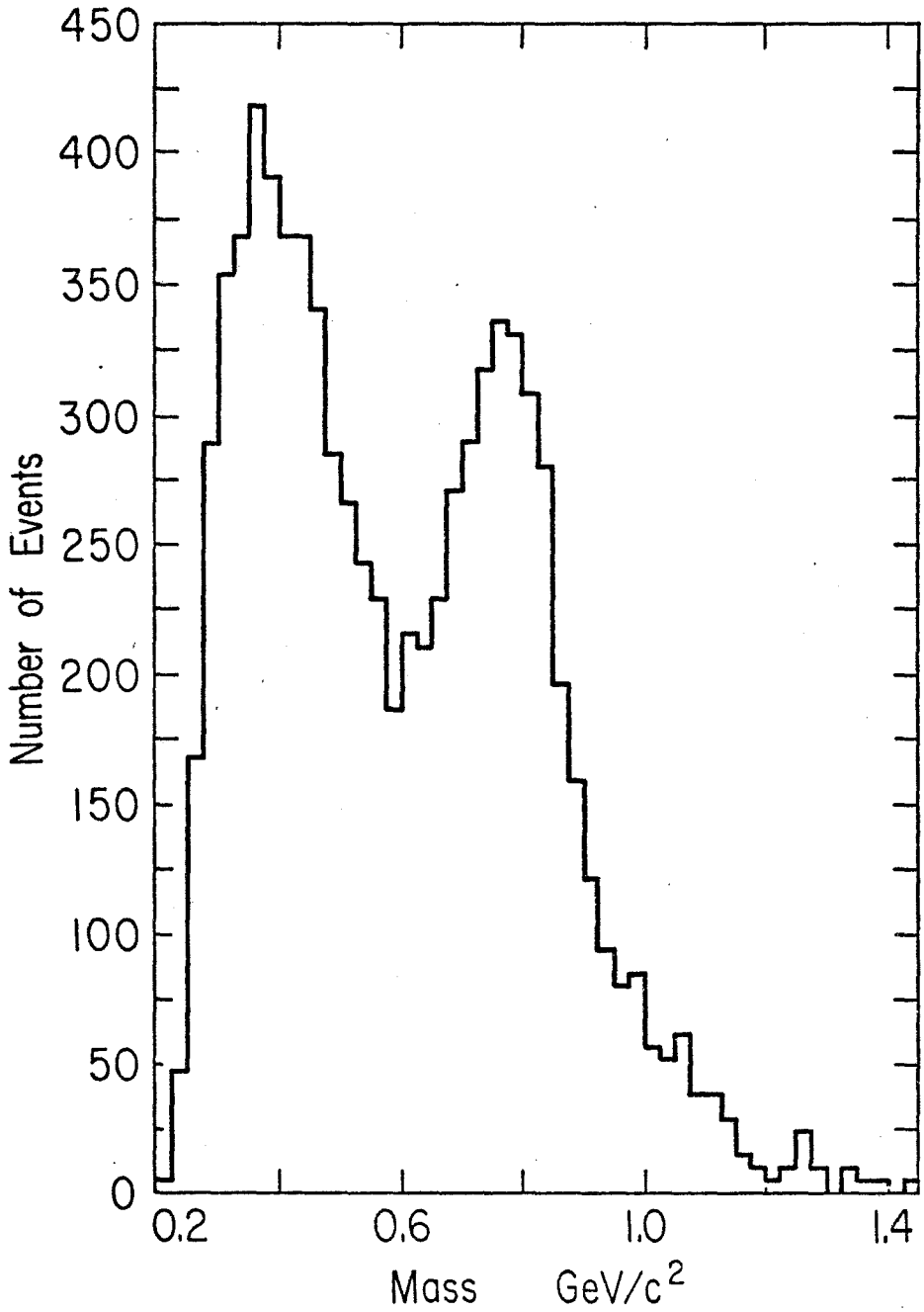
450
400
350
300
250
200
150
100
50
0
Number of Events
0.2
0.6
1.0
1.4
Mass GeV/c²

Fig. 27.--The mass obtained using the low-mass analysis and assuming that the interaction vertex is at the center of the target.

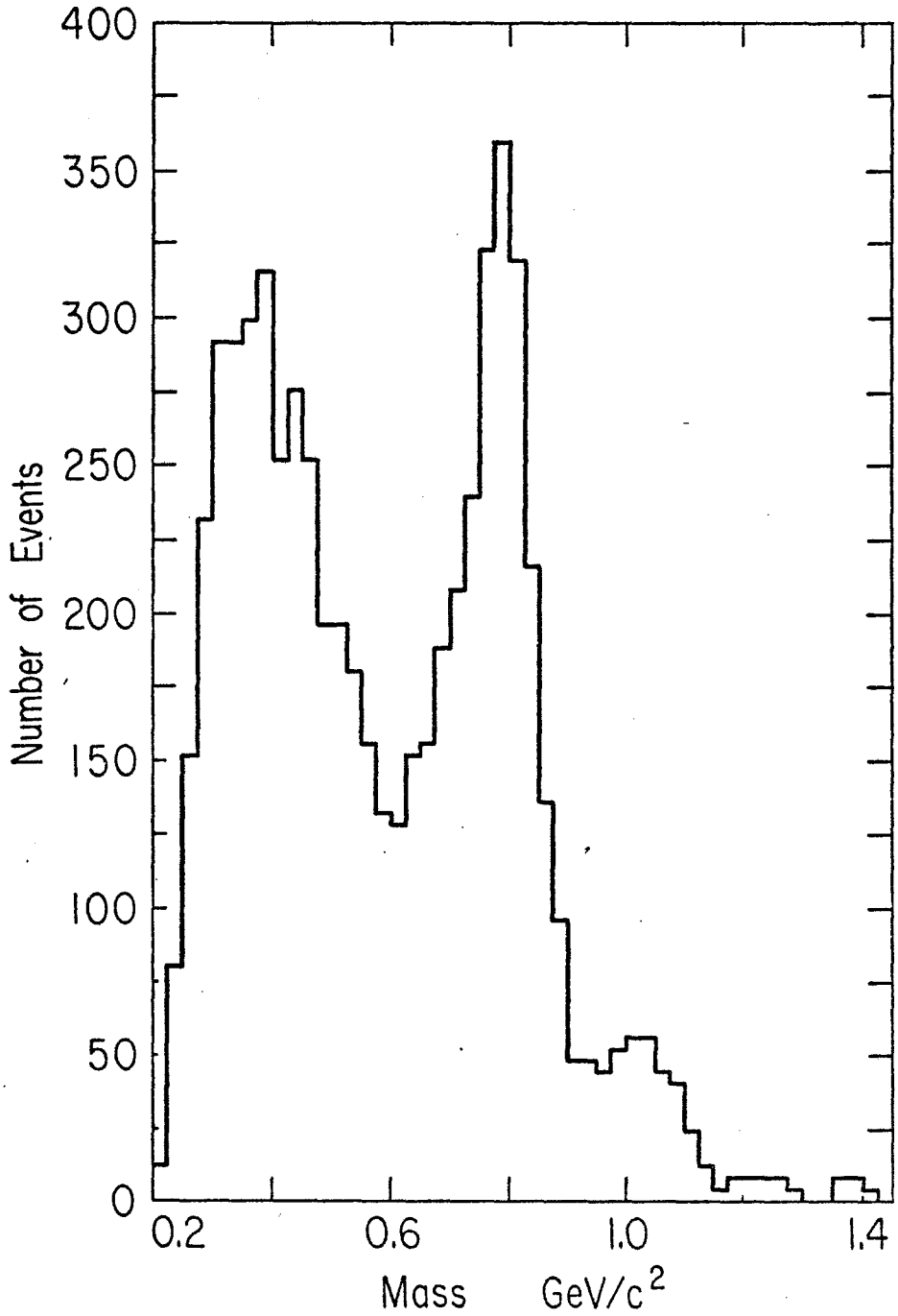
400
350
300
250
200
150
100
50
0
Number of Events
0.2
0.6
1.0
1.4
Mass GeV/c²

Fig. 28.--The mass obtained by using the low-mass analysis and by using the vertex obtained from the vertex analysis.

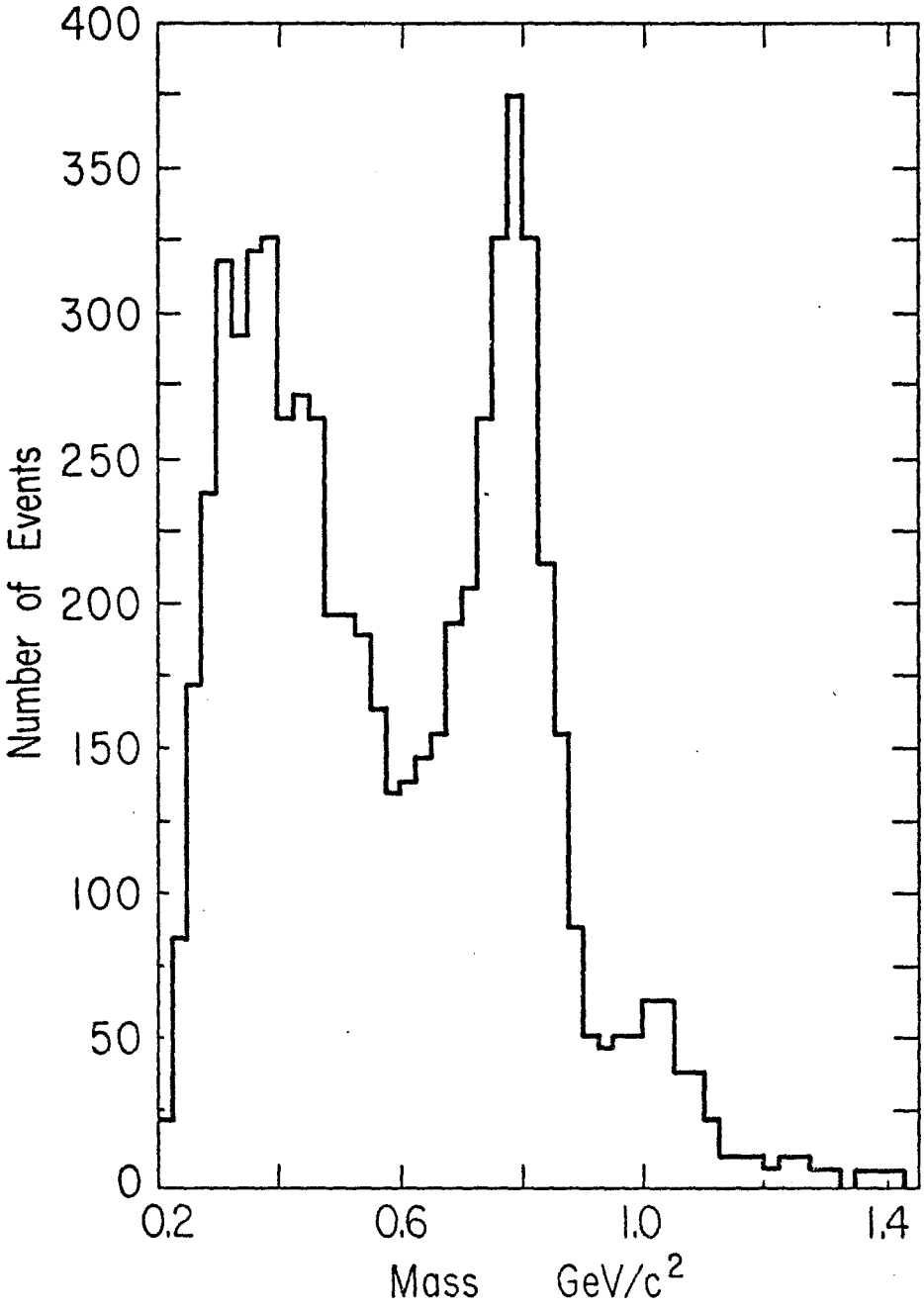
400
350
300
250
200
150
100
50
0
Number of Events
0.2
0.6
1.0
1.4
Mass GeV/c²

Fig. 29.--Mass distributions not weighted for the acceptance or like-sign subtraction: P induced events only.

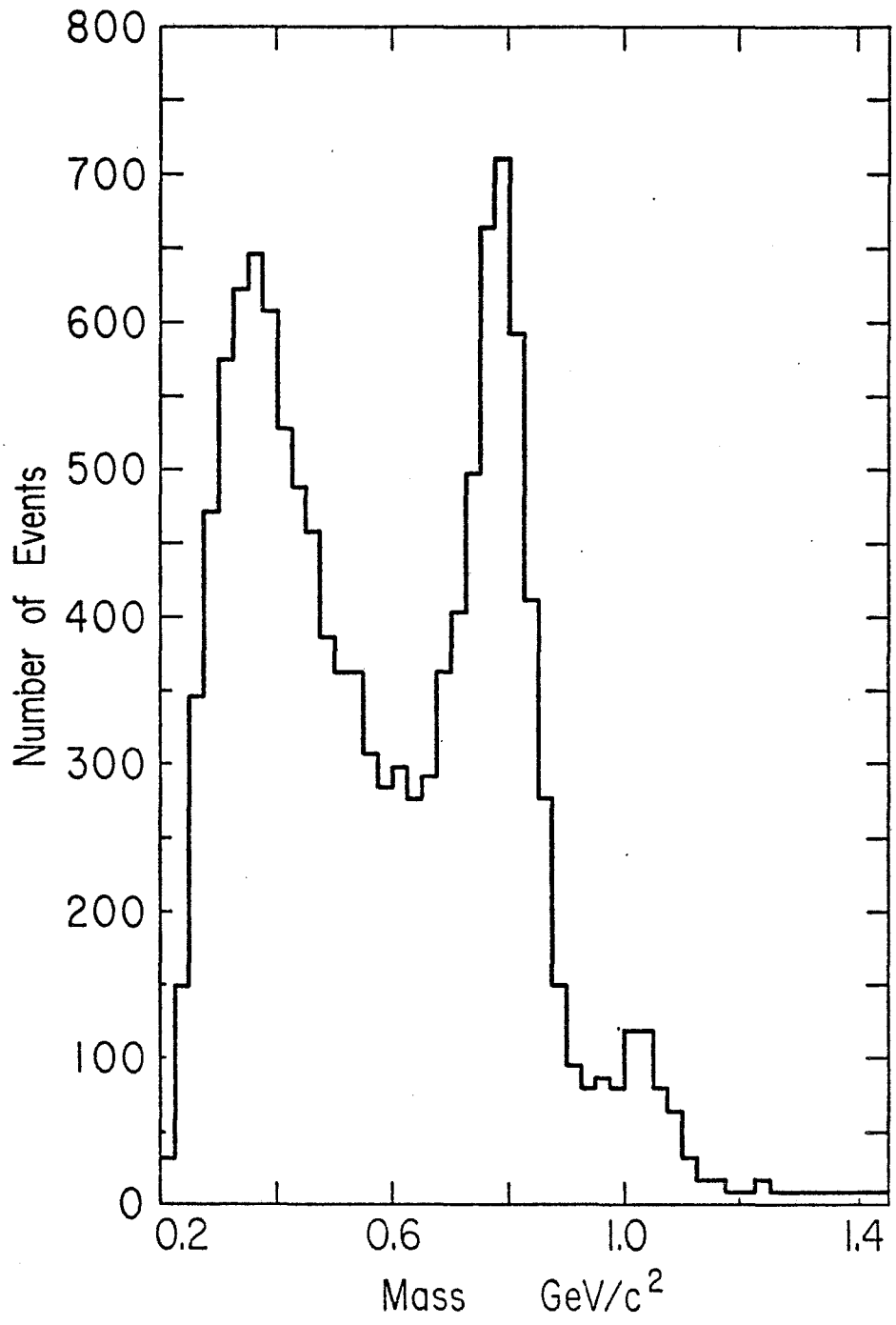
800
700
600
500
400
300
200
100
0
Number of Events
0.2
0.6
1.0
1.4
Mass GeV/c²

Fig. 30.--Mass distributions not weighted for the acceptance or like-sign subtraction: π^+ events only.

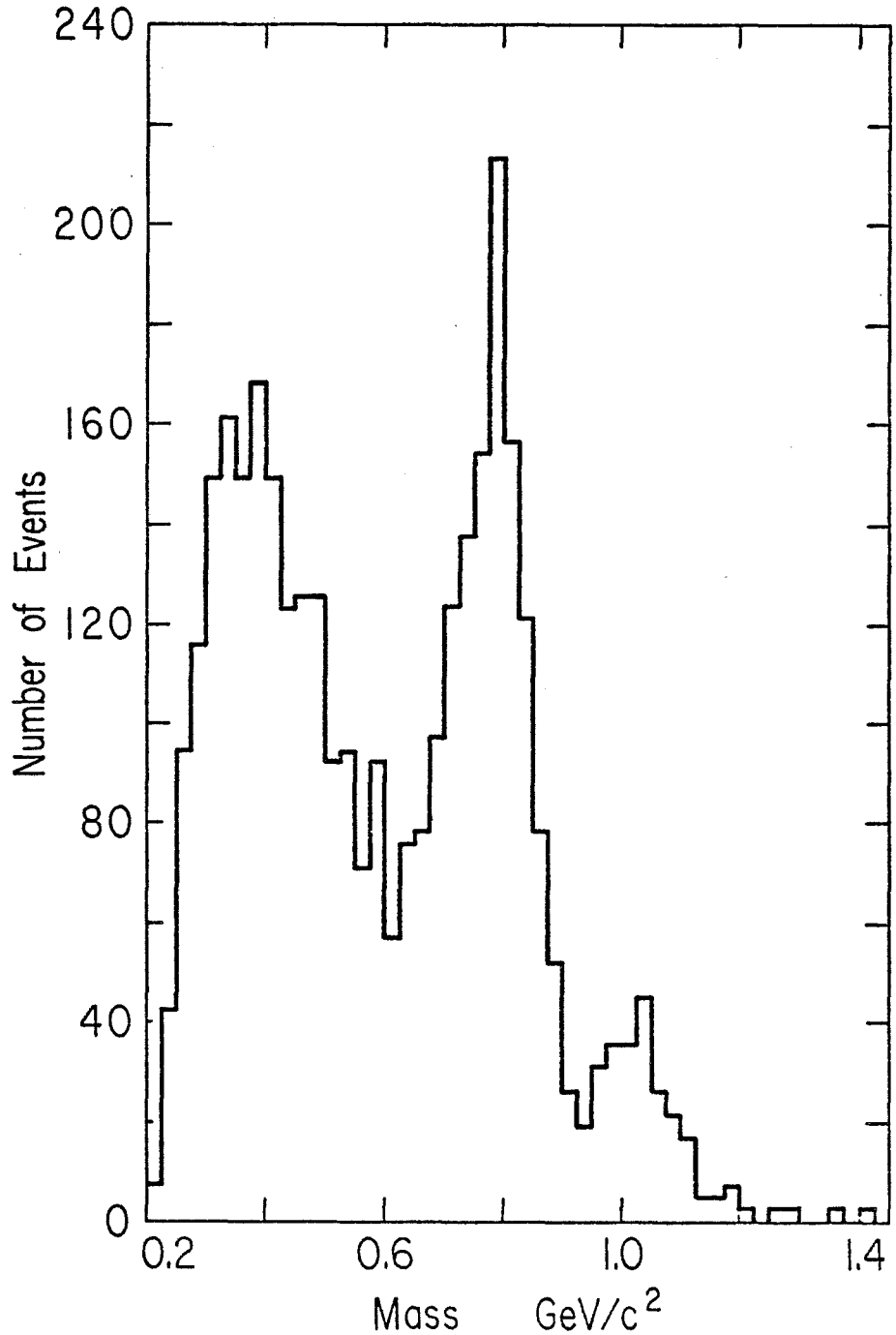
240
200
160
120
80
40
0
Number of Events
0.2
0.6
1.0
1.4
Mass GeV/c 2

Fig. 31.--Mass distributions not weighted for the acceptance or like-sign subtraction: π^- events only.

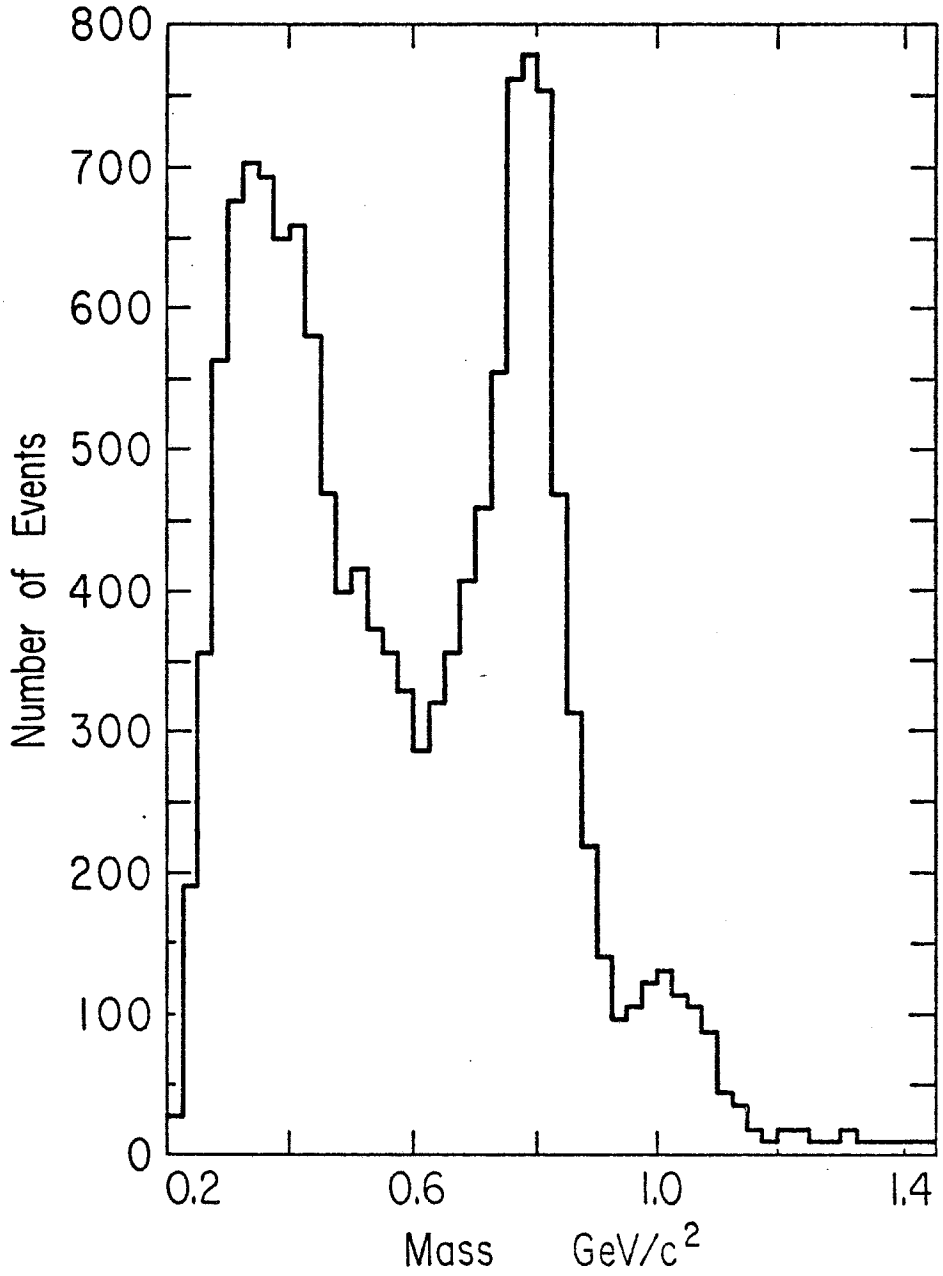
800
700
600
500
400
300
200
100
0
Number of Events
0.2
0.6
1.0
1.4
Mass GeV/c²

Fig. 32.--Mass distributions weighted by the acceptance: p induced events only.

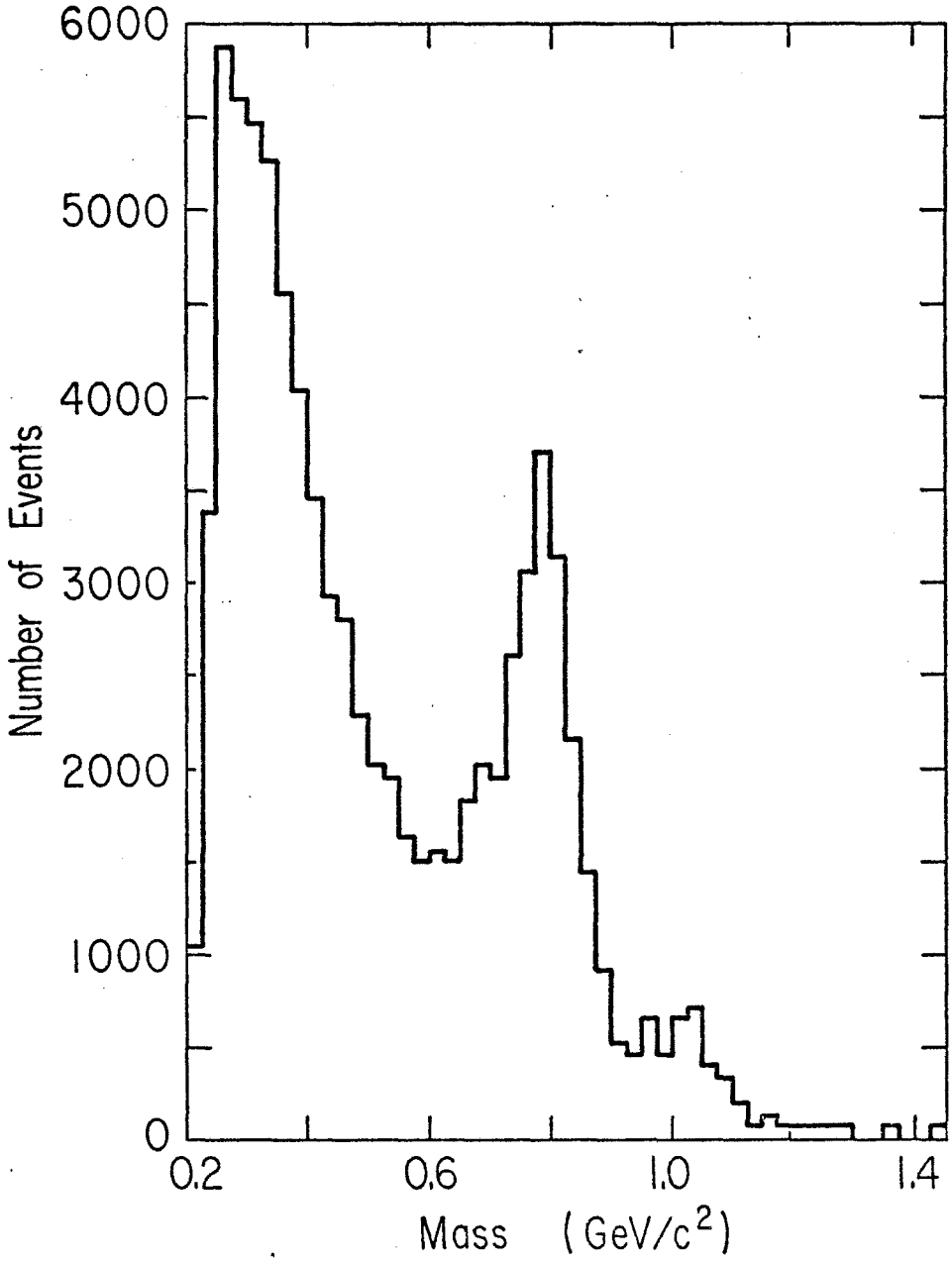
6000
5000
4000
3000
2000
1000
0
Number of Events
0.2
0.6
1.0
1.4
Mass (GeV/c²)

Fig. 33.--Mass distributions weighted by the acceptance: π^+ induced events only.

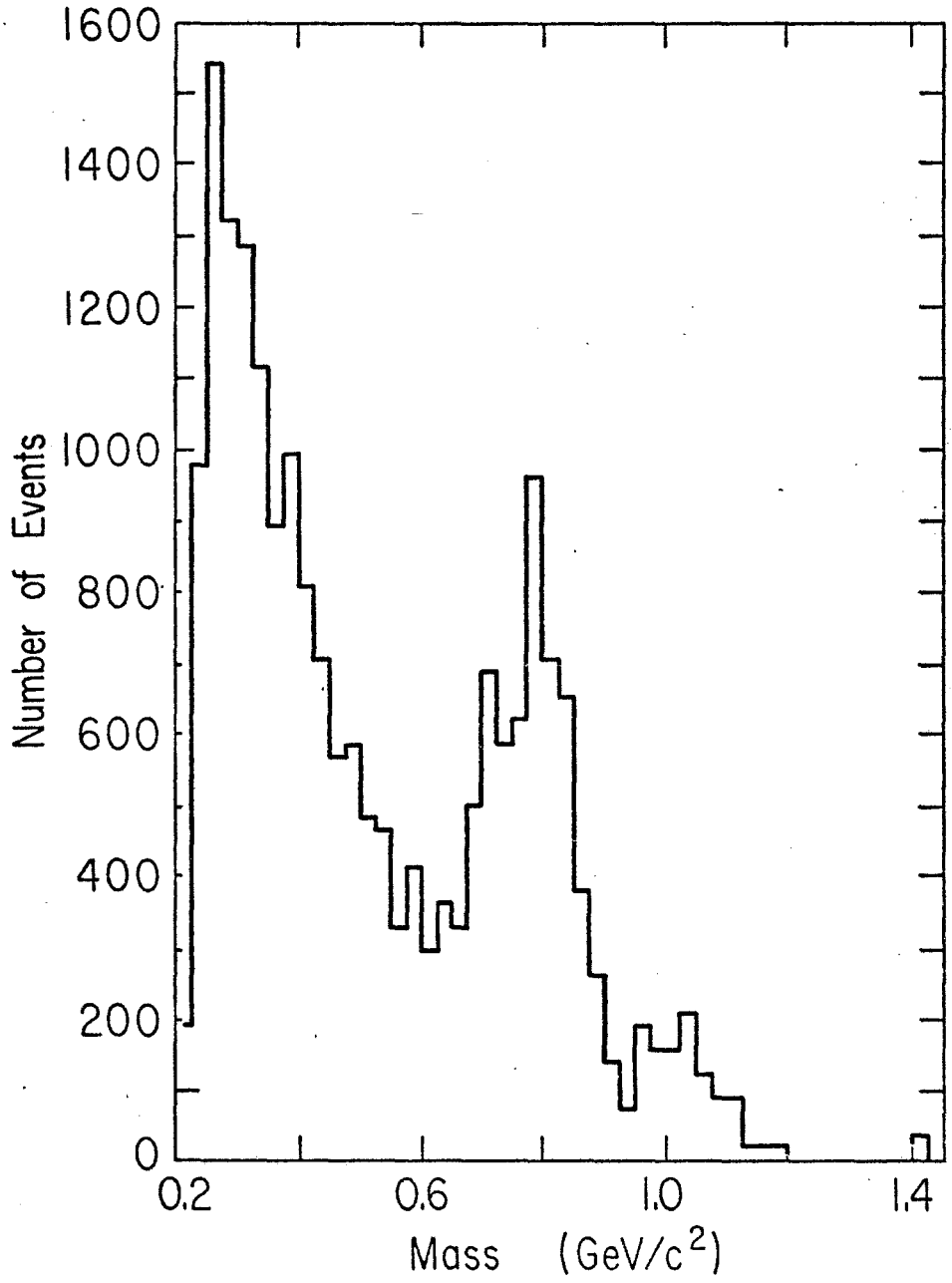
1600
1400
1200
1000
800
600
400
200
0
Number of Events
0.2
0.6
1.0
1.4
Mass (GeV/c²)

Fig. 34.--Mass distributions weighted by the acceptance: π^- induced events only.

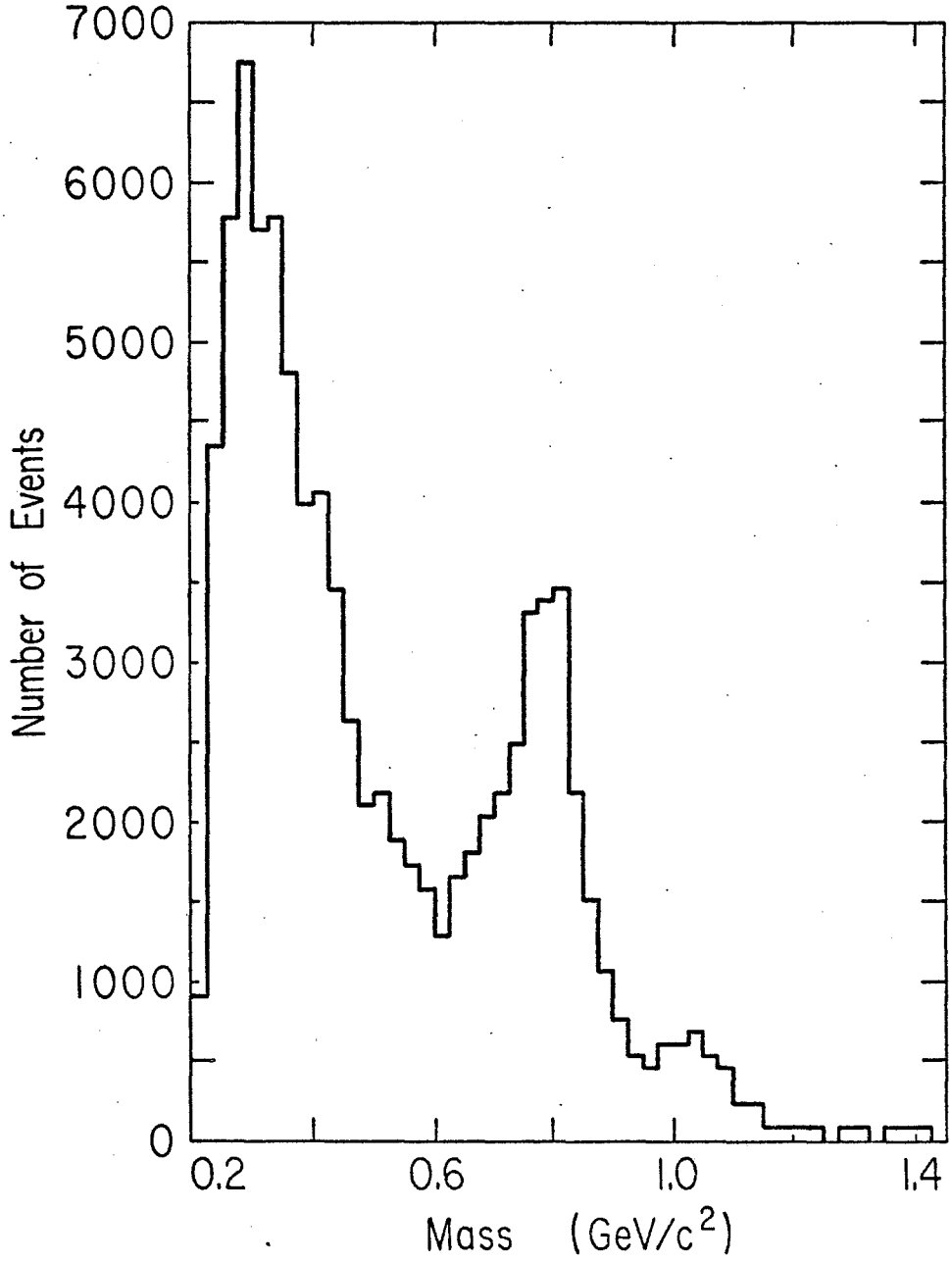
7000
6000
5000
4000
3000
2000
1000
0
Number of Events
0.2
0.6
1.0
1.4
Mass (GeV/c²)

Fig. 35.--The average weighting factors as a function of x_F used for the acceptance correction. The numbers were taken from the pC data at the ρ-ω mass region.

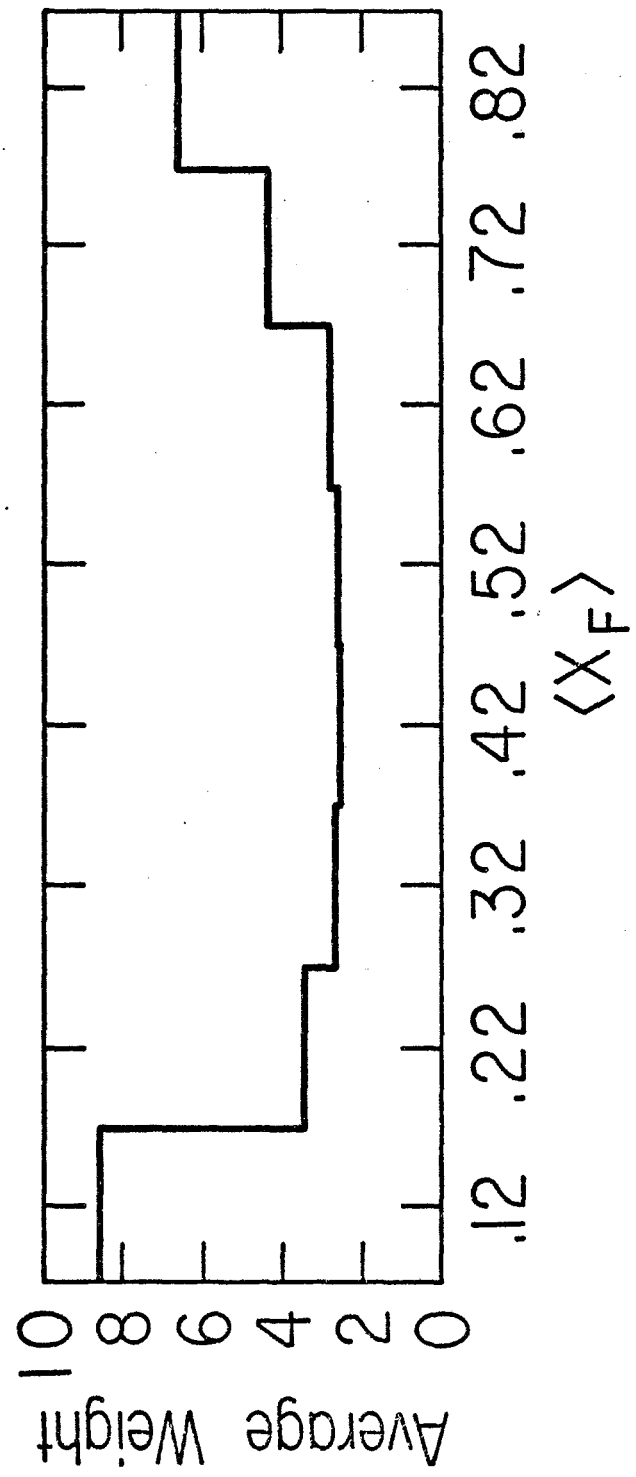
Average Weight
10
8
6
4
2
0
.12
.22
.32
.42
.52
.62
.72
.82
⟨X_F⟩

Fig. 36.--A mass distribution plot of unweighted like-sign events with opposite sign events from the same data sample superimposed.

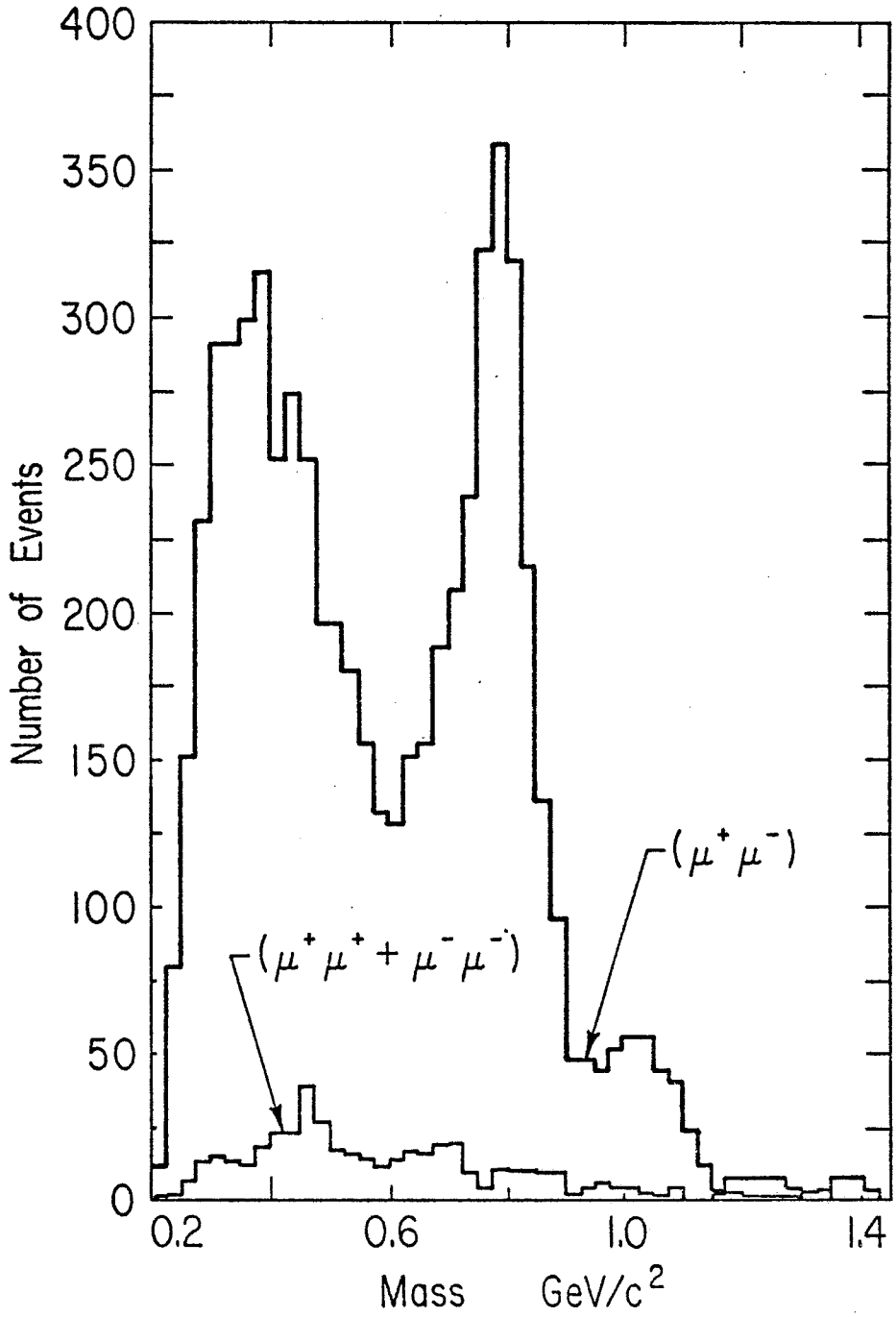
400
350
300
250
200
150
100
50
0
Number of Events
0.2
0.6
1.0
1.4
Mass GeV/c²
(μ⁺μ⁻)
(μ⁺μ⁺ + μ⁻μ⁻)

Fig. 37.--Ratios of number of raw events, in each x_F interval, from the long target to those from the short target. Higher ratios at low x_F than at high x_F would indicate secondary production of dimuons.

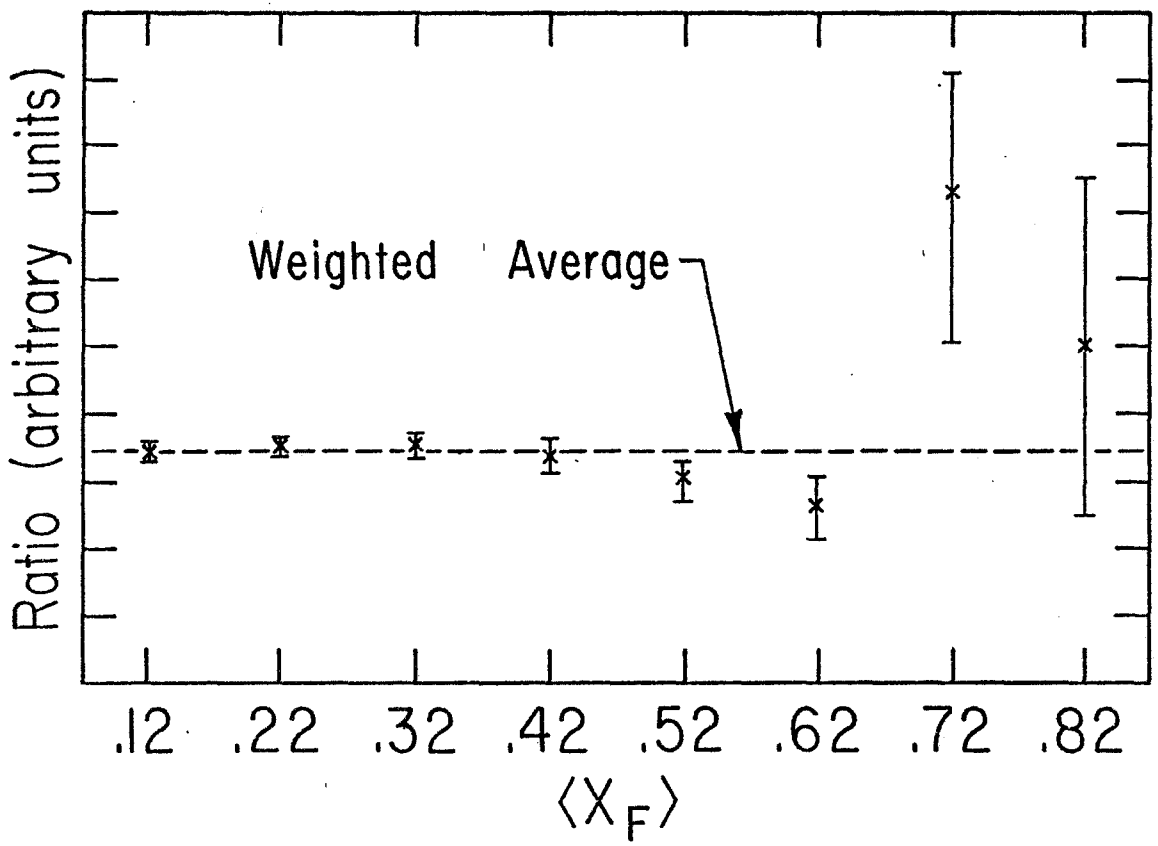
Ratio (arbitrary units)
Weighted Average
.12
.22
.32
.42
.52
.62
.72
.82
⟨X_F⟩

Fig. 38.--$E(d\sigma/dx_F)$ distributions for the proton and changed pion induced events using a carbon target, taken from the ρ-ω mass region. Exponential fits to the data are shown.

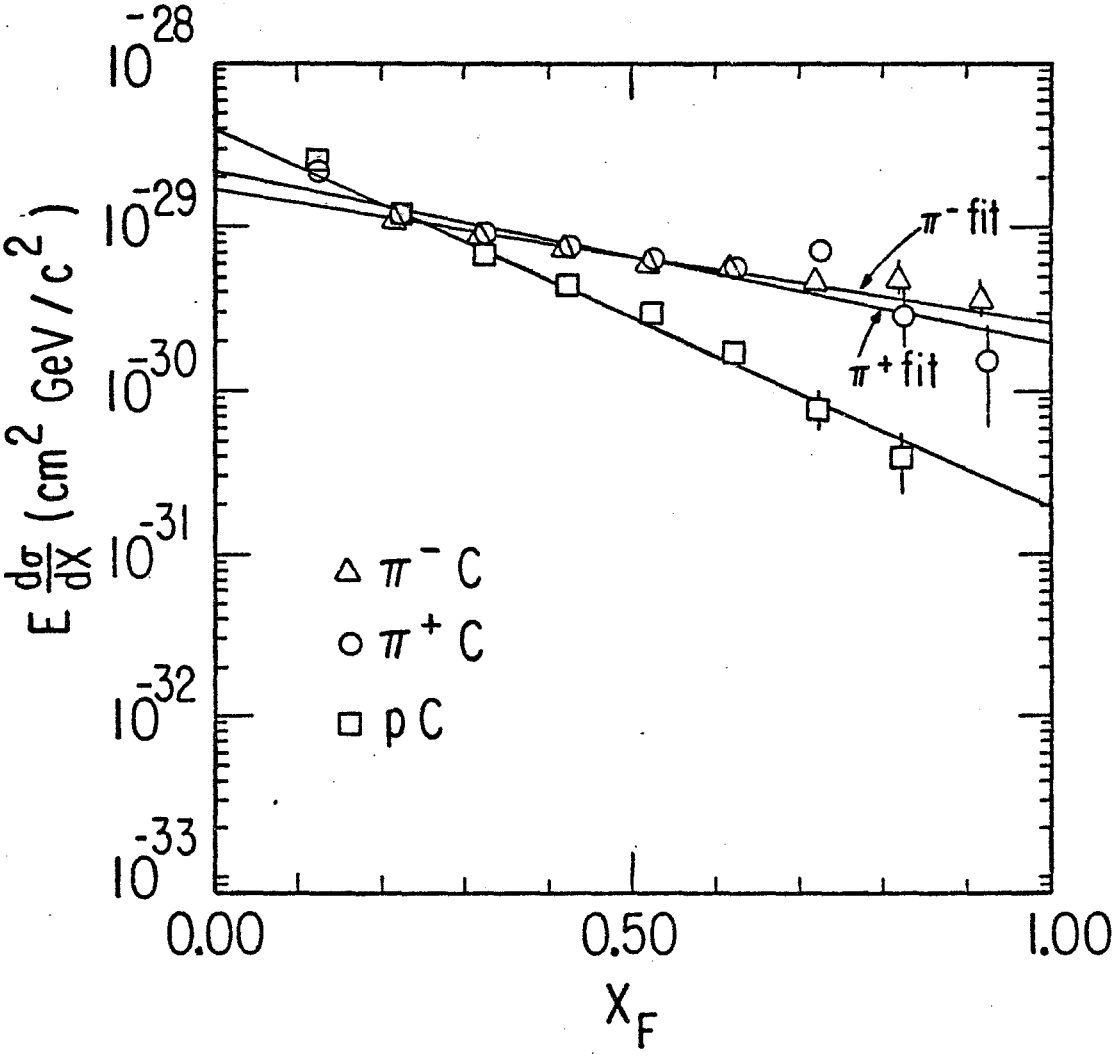
10^{-28}
10^{-29}
10^{-30}
10^{-31}
10^{-32}
10^{-33}
$E\frac{d\sigma}{dX}$ (cm^2 GeV/c^2)
π^- fit
π^+ fit
$\triangle$ π^- C
$\circ$ π^+ C
$\square$ p C
0.00
0.50
1.00
X_F

Fig. 39.--$(1/p_T)/(d\sigma/dp_T)$ distributions for the proton and charged pion induced events using a carbon target taken from the ρ-ω mass region. Exponential fits to the data for $p_T > 400$ MeV/c are shown.

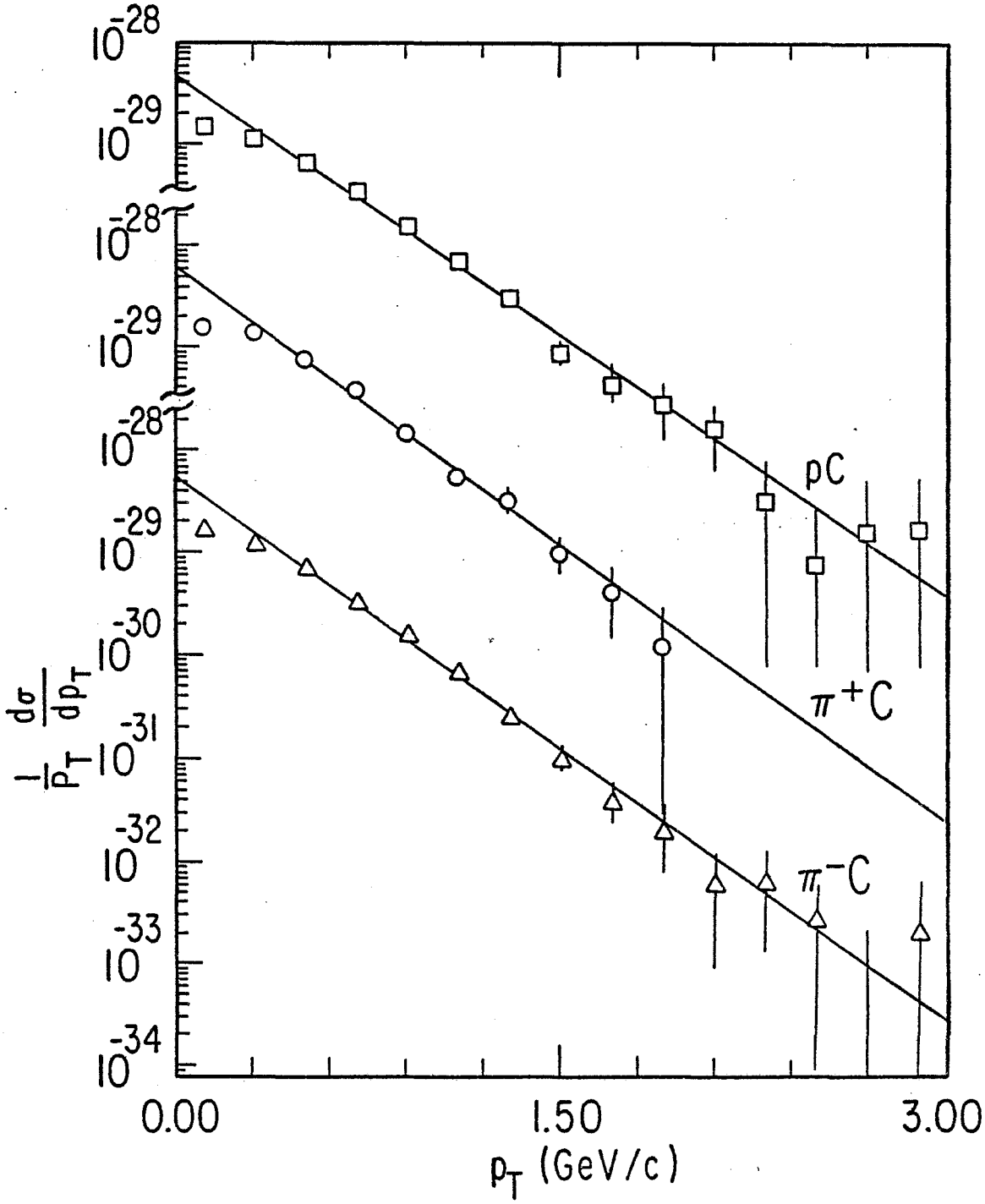
10^{-28}
10^{-29}
10^{-28}
10^{-29}
10^{-28}
10^{-29}
10^{-30}
10^{-31}
10^{-32}
10^{-33}
10^{-34}
$\frac{1}{p_T}\frac{d\sigma}{dp_T}$
pC
π^+C
π^-C
0.00
1.50
3.00
p_T (GeV/c)

Fig. 40.--Empirical fits to the continuum signal for the three incident particle types: p induced.

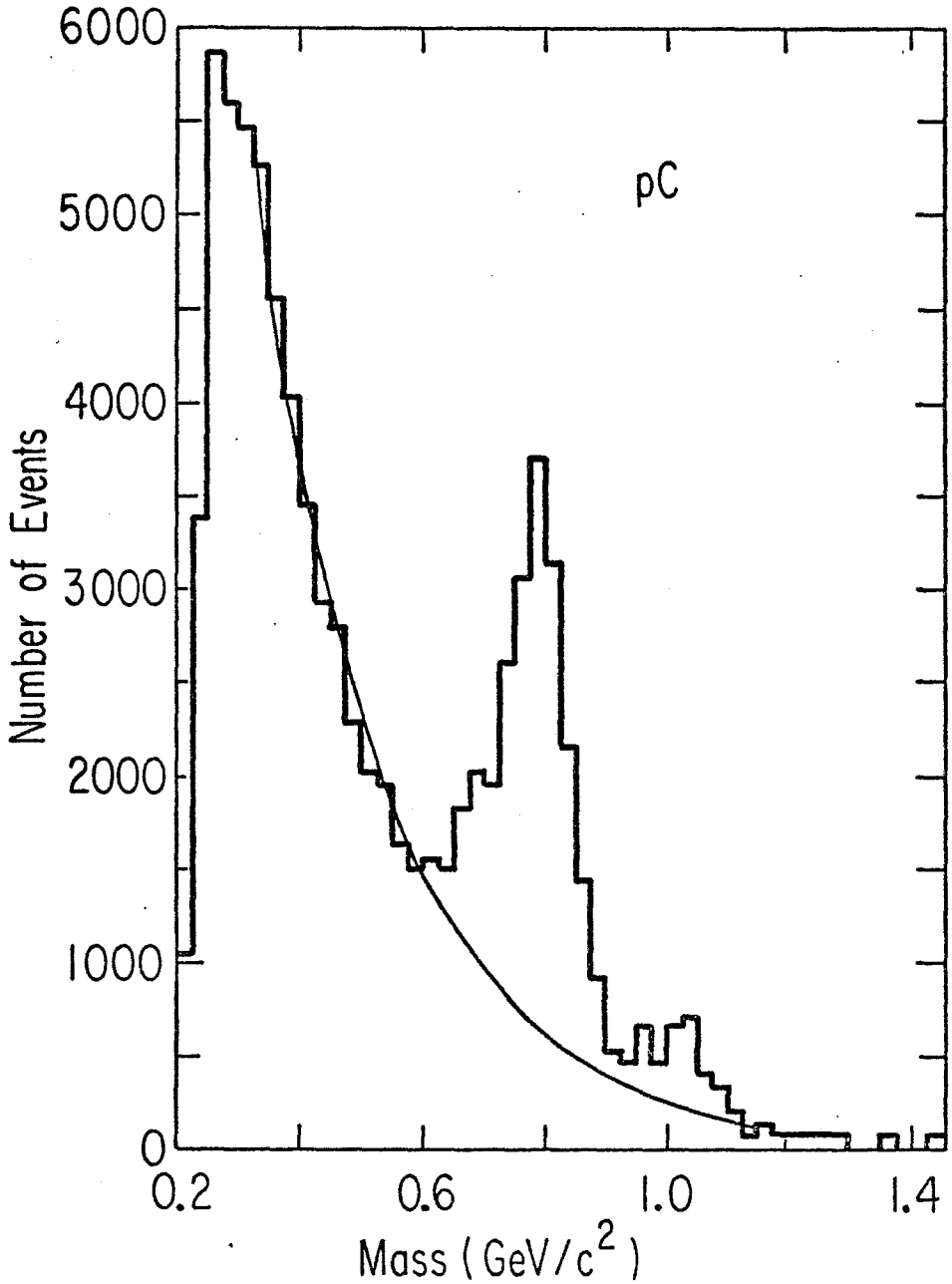
6000
5000
4000
3000
2000
1000
0
Number of Events
pC
0.2
0.6
1.0
1.4
Mass (GeV/c^2)

Fig. 41.--Empirical fits to the continuum signal for the three incident particle types: π^+ induced.

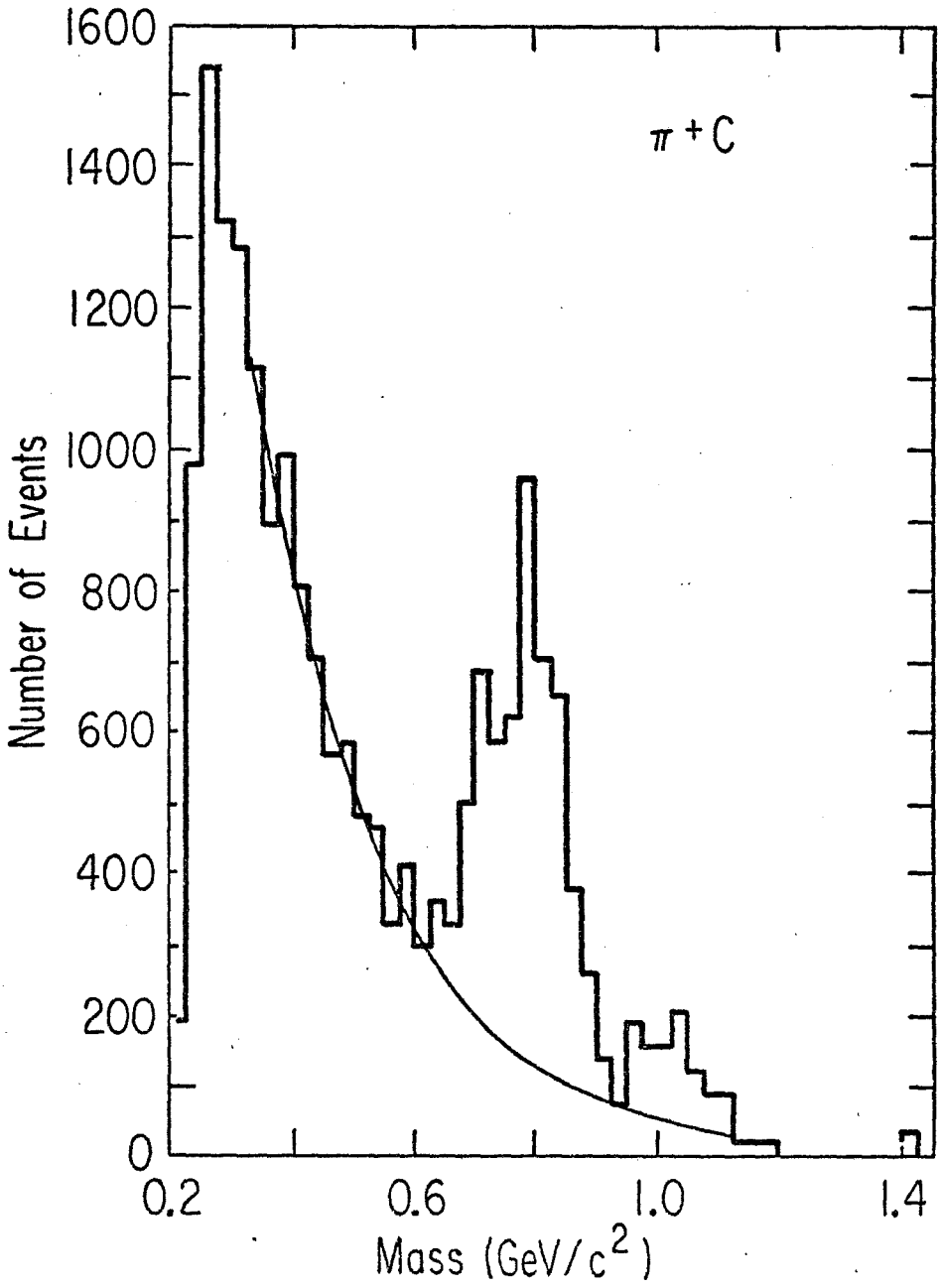
1600
1400
1200
1000
800
600
400
200
0
Number of Events
π + C
0.2
0.6
1.0
1.4
Mass (GeV/c²)

Fig. 42.--Empirical fits to the continuum signal for the three incident particle types: π^- induced.

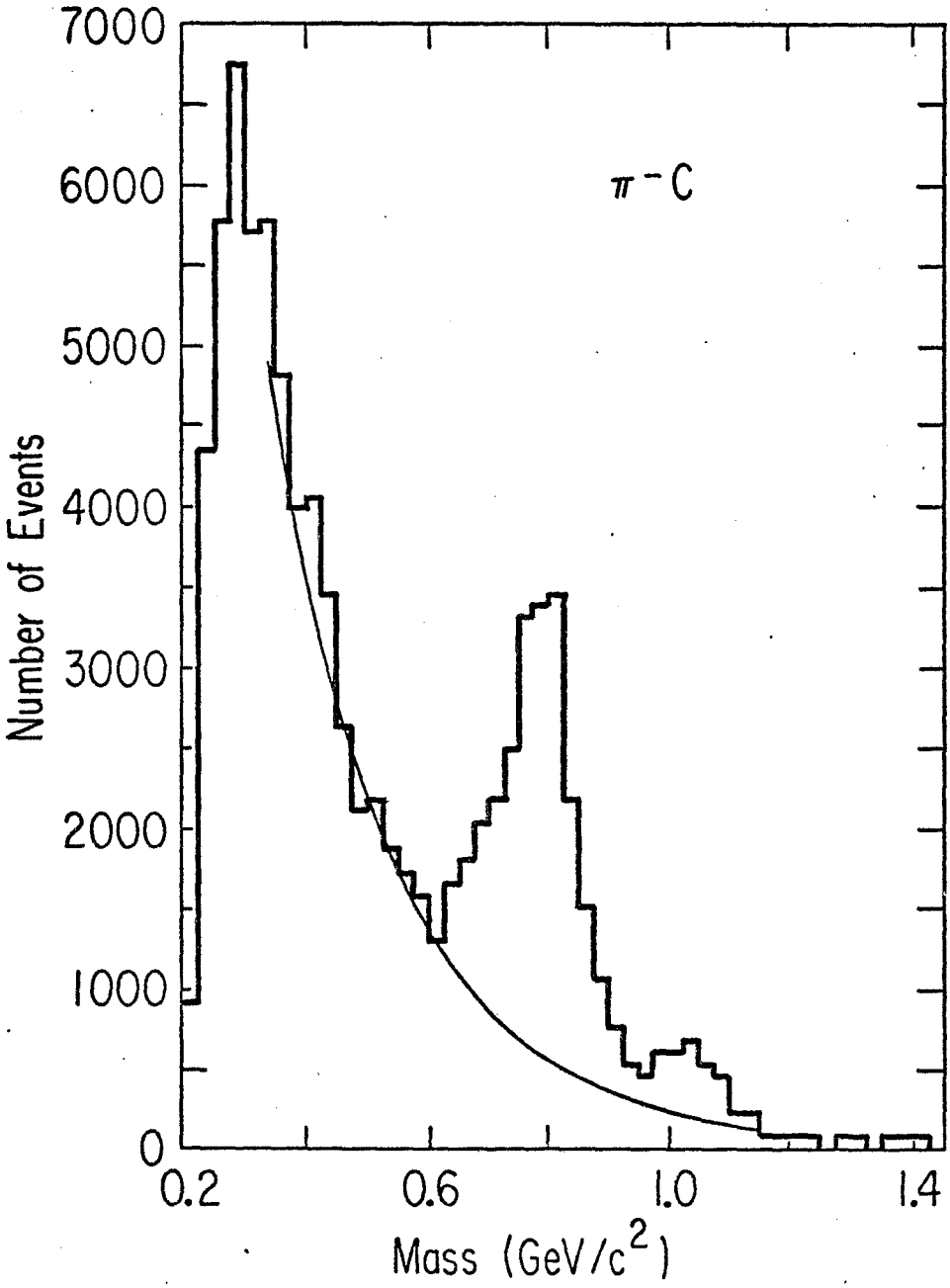
7000
6000
5000
4000
3000
2000
1000
0
Number of Events
π - C
0.2
0.6
1.0
1.4
Mass (GeV/c²)

Fig. 43.--Fit parameters for the transverse momentum fits to the $(1/p_T)/(d\sigma/dp_T)$ shown as a function of mass region.

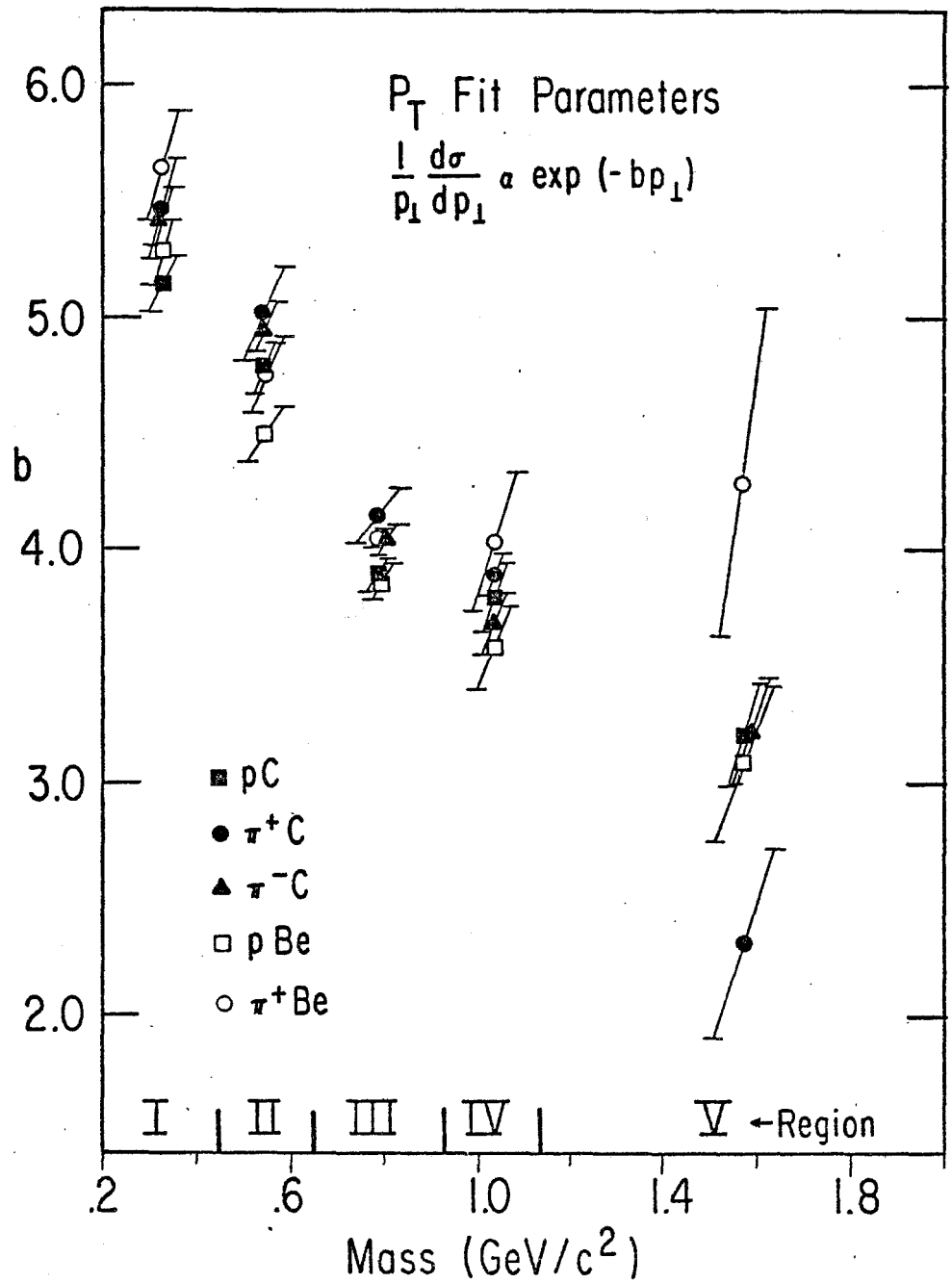
P_T Fit Parameters
$\frac{1}{p_\perp}\frac{d\sigma}{dp_\perp} \propto \exp(-bp_\perp)$
6.0
5.0
4.0
3.0
2.0
b
pC
π^+C
π^-C
p Be
π^+Be
I
II
III
IV
V ←Region
.2
.6
1.0
1.4
1.8
Mass (GeV/c^2)

Fig. 44.--Fit parameters for the $E(d\sigma/dx_F)$ fits shown as a function of mass region.

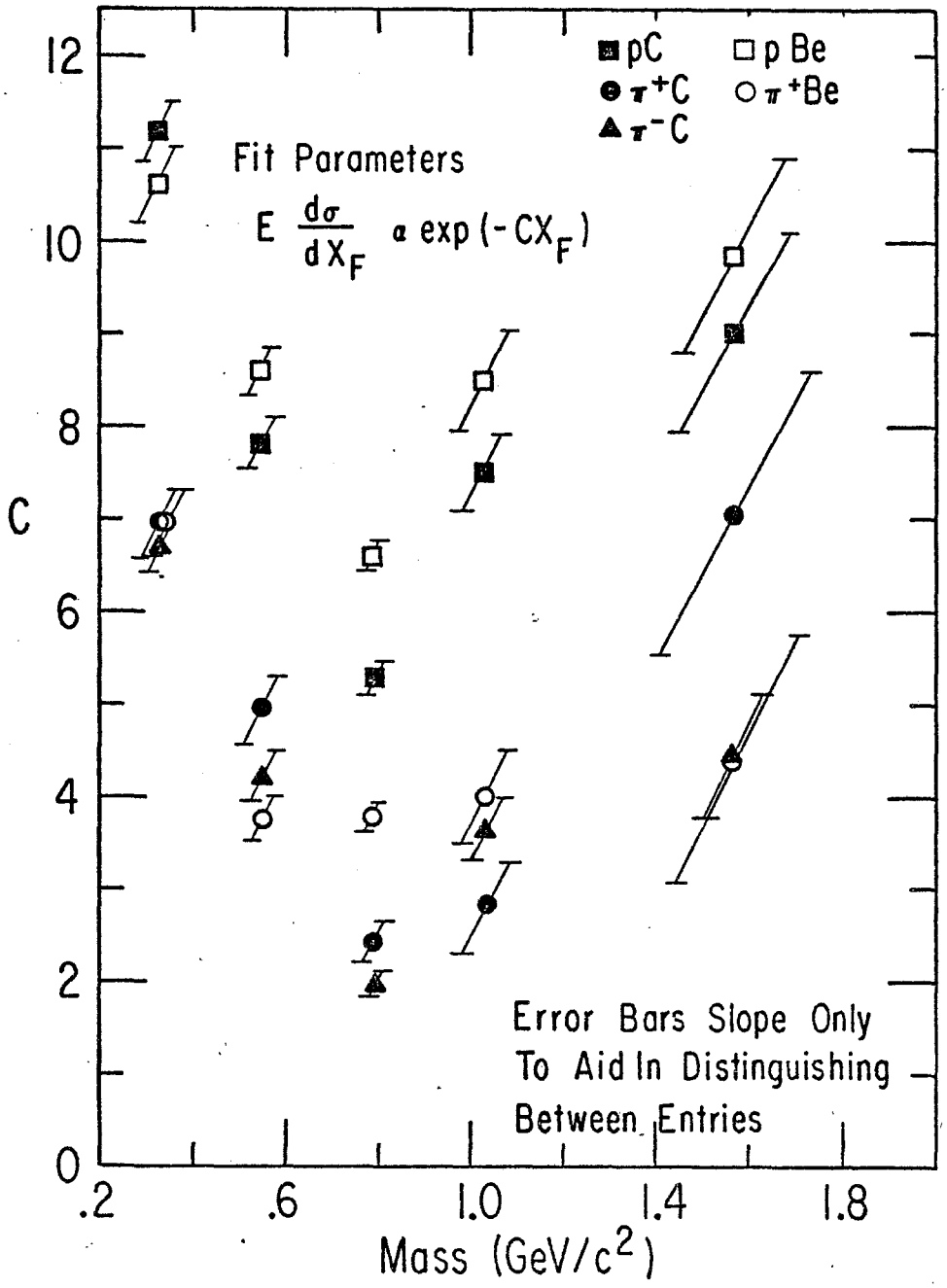
pC
p Be
π+C
π+Be
π−C
Fit Parameters
E dσ/dX_F ∝ exp(−CX_F)
C
Error Bars Slope Only
To Aid In Distinguishing
Between Entries
Mass (GeV/c²)
0
2
4
6
8
10
12
.2
.6
1.0
1.4
1.8

Fig. 45.--Dimuon production diagrams for low mass contributions. (a) the Bethe-Heitler process; (b) the omega Dalitz decay; (c) the eta Dalitz decay.

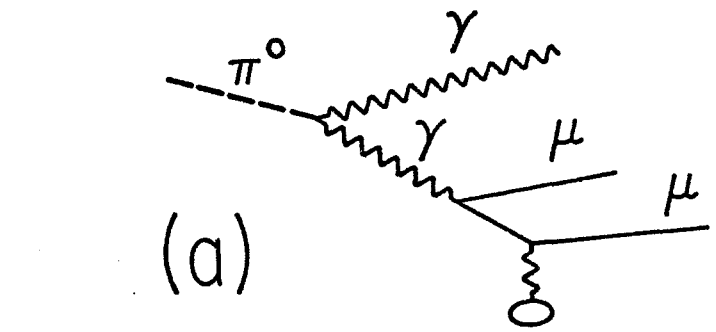

(a)

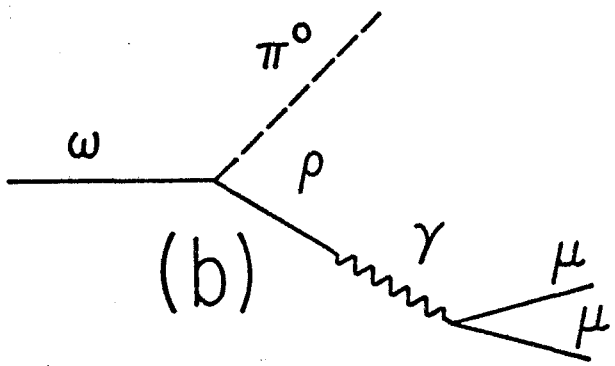

(b)

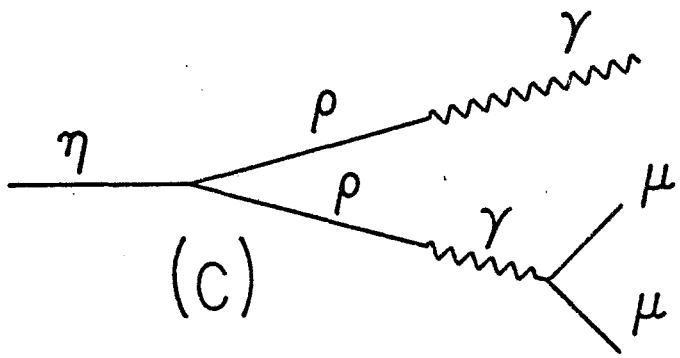

(c)

Fig. 46.--The weighted p induced mass distribution with Bethe-Heitler and ω Dalitz backgrounds superimposed. The η Dalitz signal was then maximized to the remaining events in the $0.25 < M < 0.35$ GeV/c^2 mass interval. The $\eta \rightarrow \mu\mu$ calculated signal is then added.

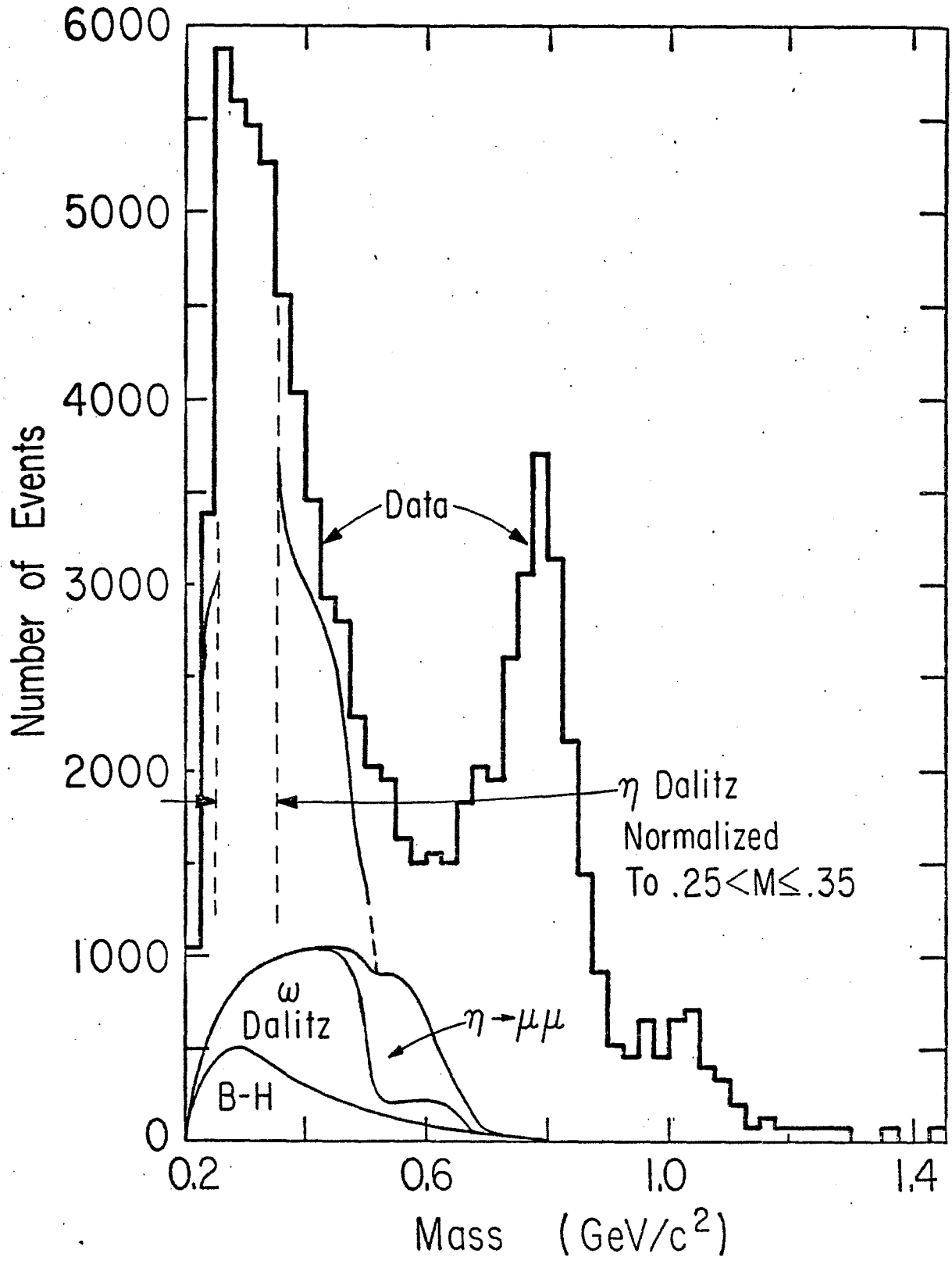
6000
5000
4000
3000
2000
1000
0
Number of Events
Data
η Dalitz
Normalized
To .25<M≤.35
ω
Dalitz
η→μμ
B-H
0.2
0.6
1.0
1.4
Mass (GeV/c²)

Fig. 47.--The eta Dalitz contribution to the low mass signal calculated from the η/ρ cross sections. The calculation is explained in the text. Other low mass contributions are shown. Contributions do not overlap.

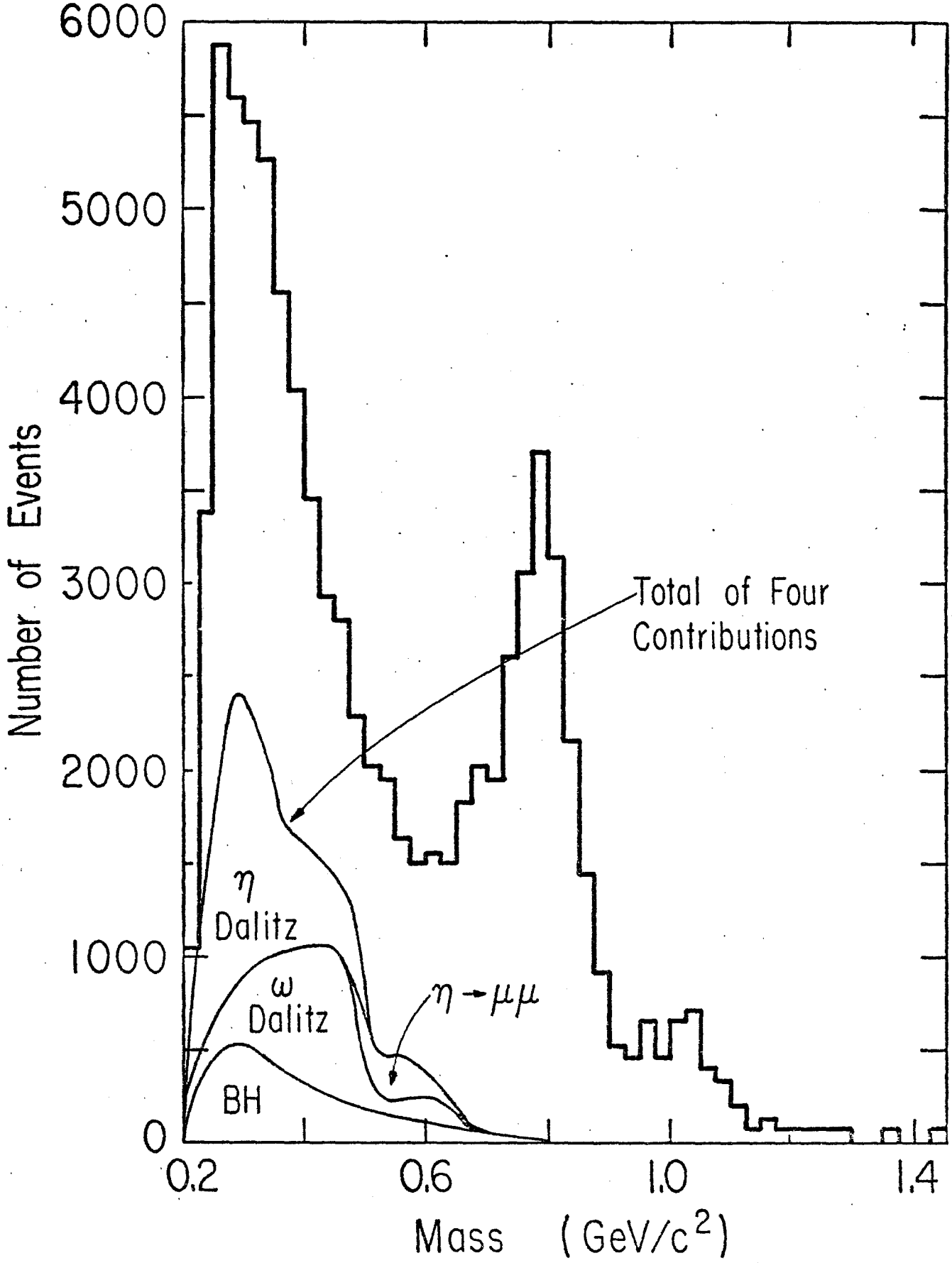
6000
5000
4000
3000
2000
1000
0
Number of Events
Total of Four Contributions
η Dalitz
ω Dalitz
η → μμ
BH
0.2
0.6
1.0
1.4
Mass (GeV/c²)

Fig. 48.--The $(1/p_T)/(d\sigma/dp_T)$ distributions for the data in the mass interval $0.21 \leq M < 0.45$ GeV/c^2. Superimposed is the expected p_T distribution assuming that 20 per cent of the signal is due to the eta Dalitz decay.

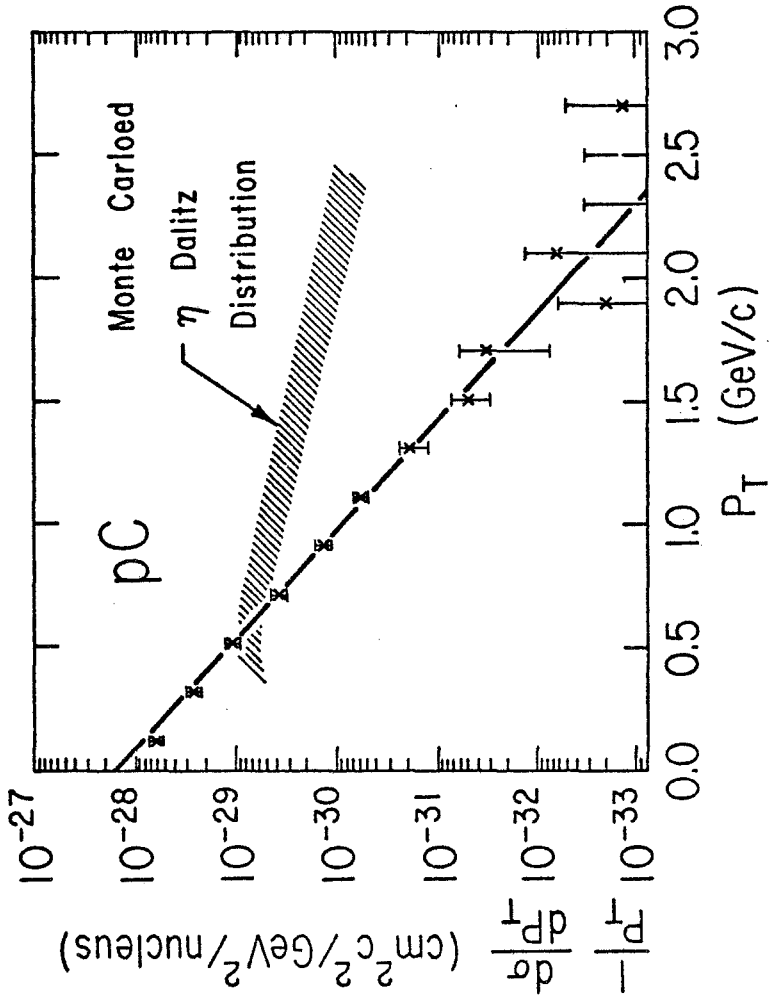
pC
Monte Carloed
η Dalitz
Distribution
P_T (GeV/c)
$\frac{P_T}{} \frac{d\sigma}{dP_T}$ (cm²c²/GeV²/nucleus)
10⁻²⁷
10⁻²⁸
10⁻²⁹
10⁻³⁰
10⁻³¹
10⁻³²
10⁻³³
0.0
0.5
1.0
1.5
2.0
2.5
3.0

Fig. 49.--The bremsstrahlung model contribution added to the other "expected" low mass contributions and superimposed on the data.

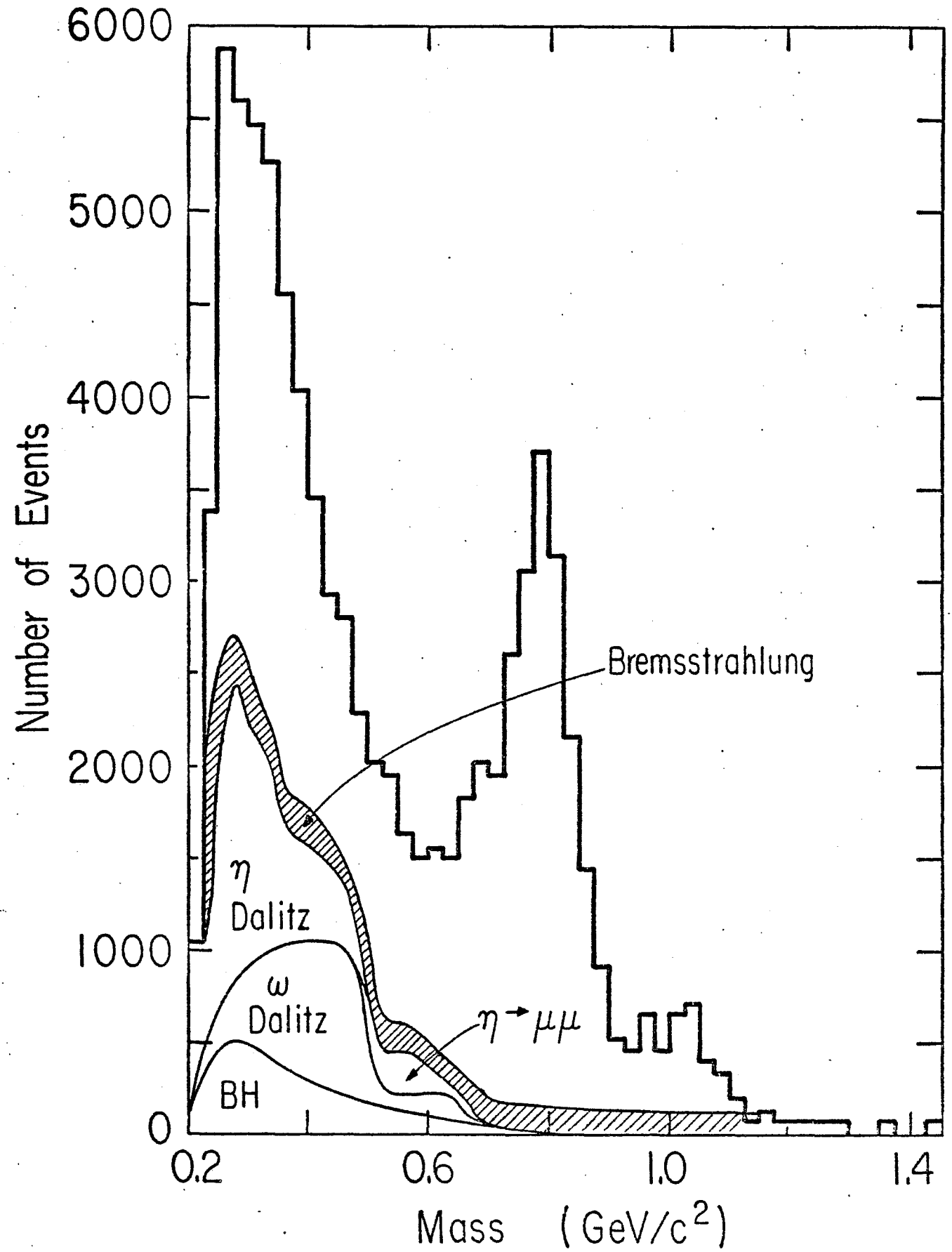
6000
5000
4000
3000
2000
1000
0
Number of Events
0.2
0.6
1.0
1.4
Mass (GeV/c²)
Bremsstrahlung
η
Dalitz
ω
Dalitz
BH
η → μμ

Fig. 50.--$d\sigma/dx_F$ distributions integrated over $p_T < 600$ MeV/c for the pion spectrum obtained from Ref. 53, and the single muon yield obtained from the pC data. The vector meson contribution and the total dimuon contribution are shown.

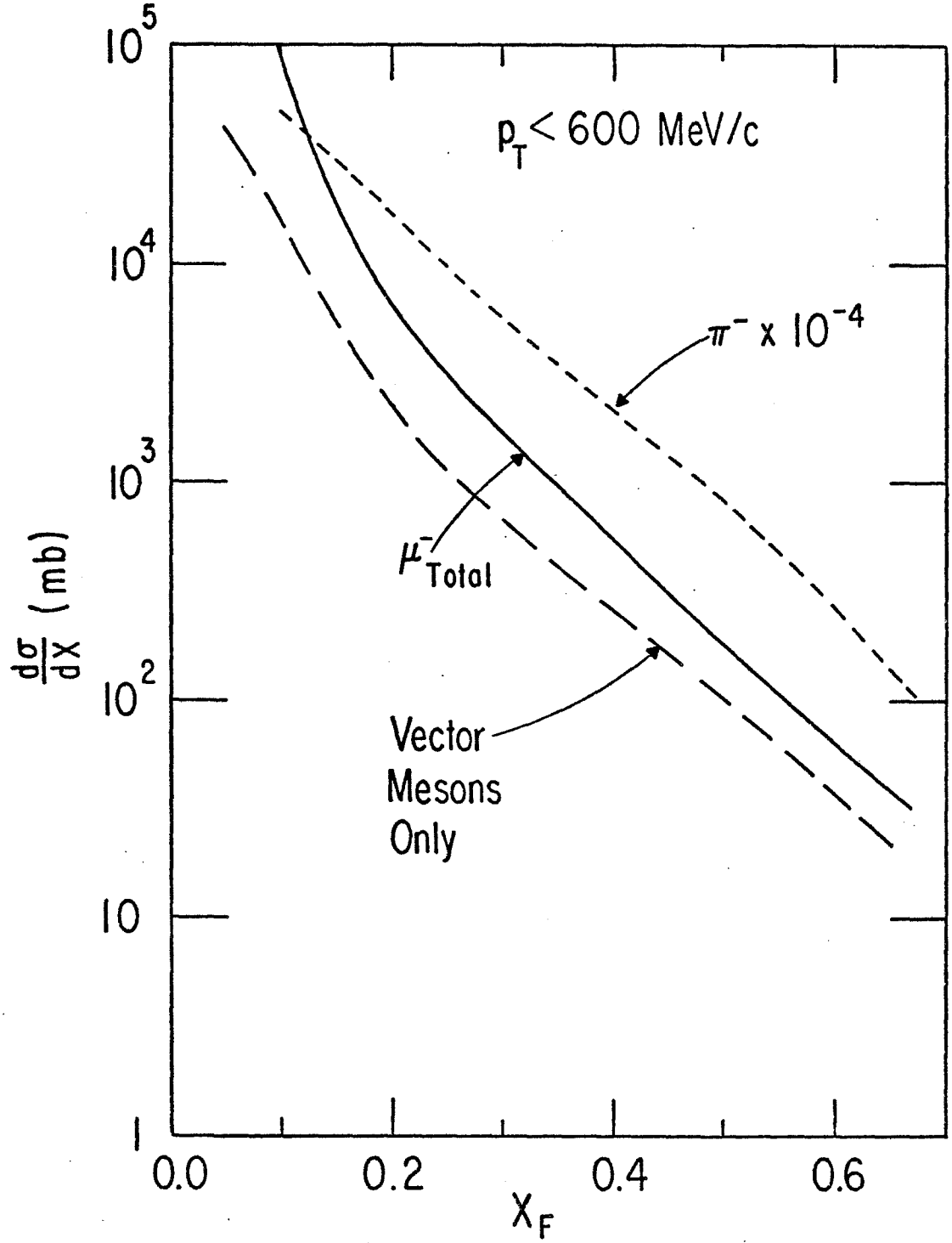
10^5
10^4
10^3
10^2
10
1
$\frac{d\sigma}{dx}$ (mb)
$p_T < 600$ MeV/c
$\pi^- \times 10^{-4}$
μ^-_{Total}
Vector
Mesons
Only
0.0
0.2
0.4
0.6
X_F

Fig. 51.--The μ^-/π^- ratios obtained from the previous figure. Vector meson and total contributions are shown. Errors are about ±20 per cent of the signals. Shown also are results from single muon experiments.

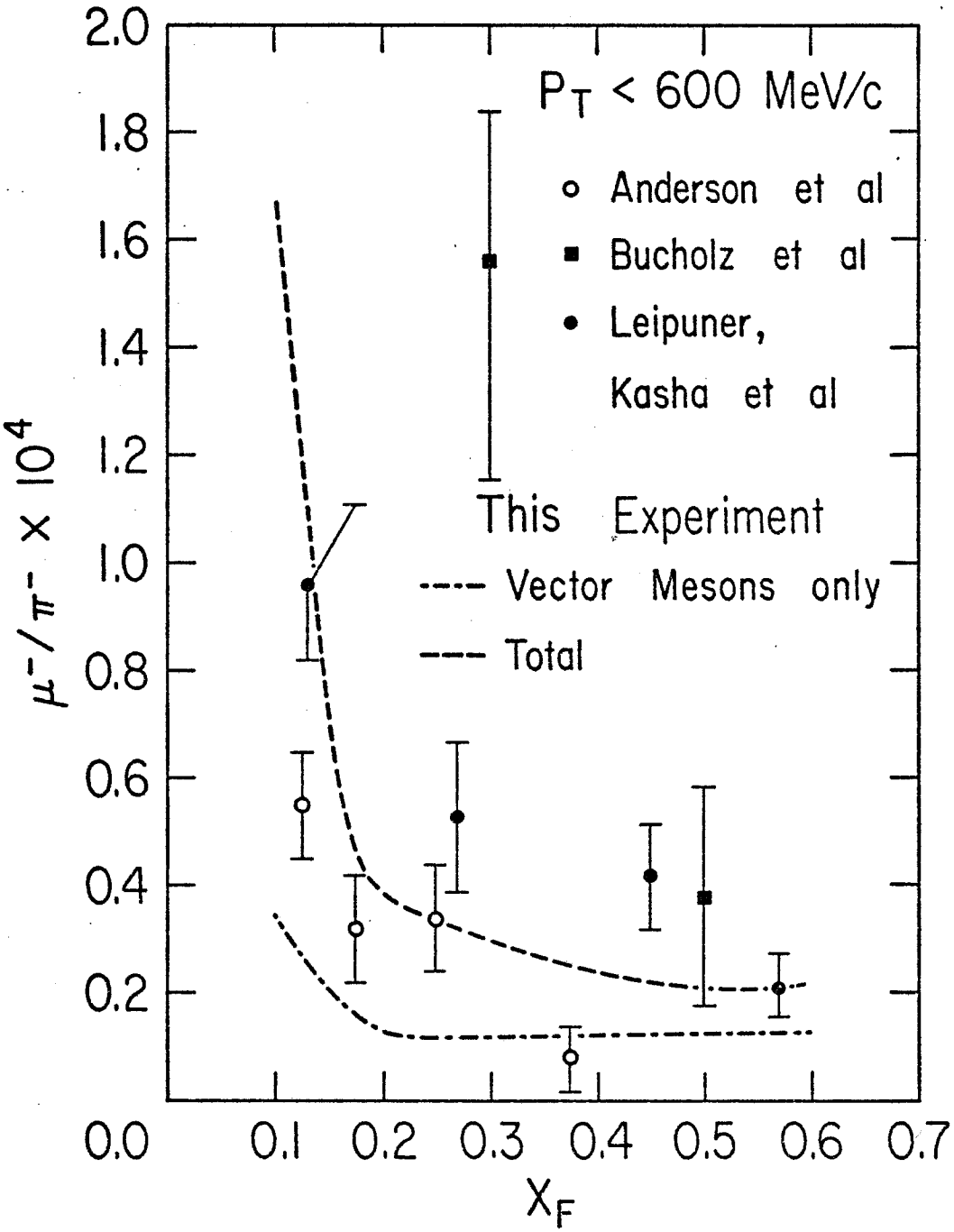
P_T < 600 MeV/c
Anderson et al
Bucholz et al
Leipuner, Kasha et al
This Experiment
Vector Mesons only
Total
$\mu^-/\pi^- \times 10^4$
X_F
2.0
1.8
1.6
1.4
1.2
1.0
0.8
0.6
0.4
0.2
0.0
0.1
0.2
0.3
0.4
0.5
0.6
0.7

Fig. 52.--Differential cross sections evaluated at $x_F = 0.0$ for the pion spectrum obtained from Ref. 57, and the single muon yield obtained from the pC data. Extrapolations, in $E(d\sigma/dx_F)$, of the dimuon signal to $x_F = 0.0$ were done as explained in the text. Both flat ane exponential extrapolations [in $E(d\sigma/dx_F)$] are shown. The ψ and total vector meson contributions for the flat extrapolations are shown, as well as totals for both extrapolations.

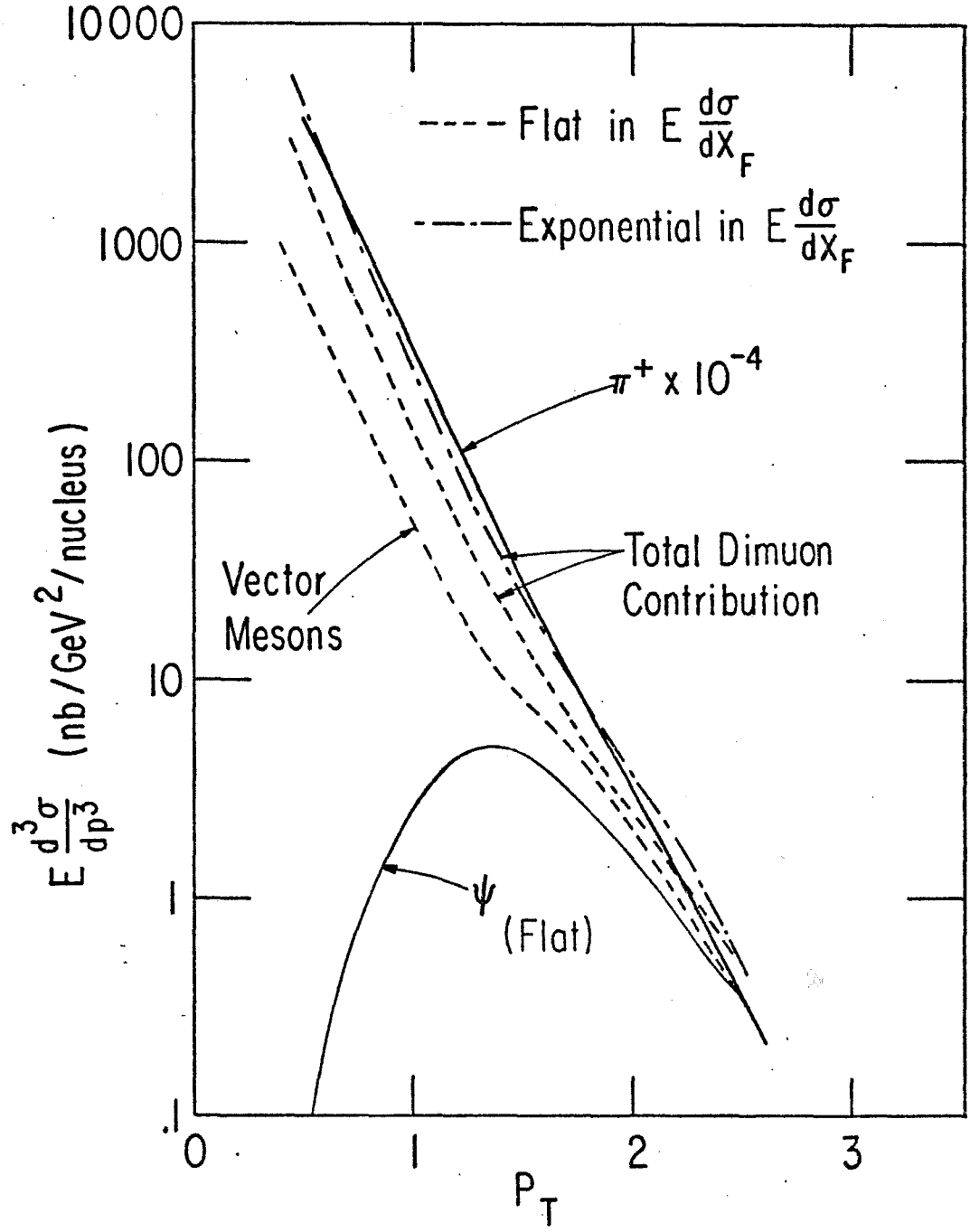
10000
1000
100
10
1
.1
0
1
2
3
P_T
$E\frac{d^3\sigma}{dp^3}$ (nb/GeV^2/nucleus)
---- Flat in $E\frac{d\sigma}{dX_F}$
-·-·- Exponential in $E\frac{d\sigma}{dX_F}$
$\pi^+ \times 10^{-4}$
Total Dimuon Contribution
Vector Mesons
ψ (Flat)

Fig. 53.--The μ^-/π^- ratios obtained from the previous figure. Vector meson and total contributions are shown for the flat extrapolation and the total contribution is shown for the exponential extrapolations. The two methods of extrapolations represent the range of the possible values of the low x_F signal and hence the "errors" in the μ^-/π^- ratio are represented by the differences in methods of extrapolation. The results of single muon experiments are superimposed.

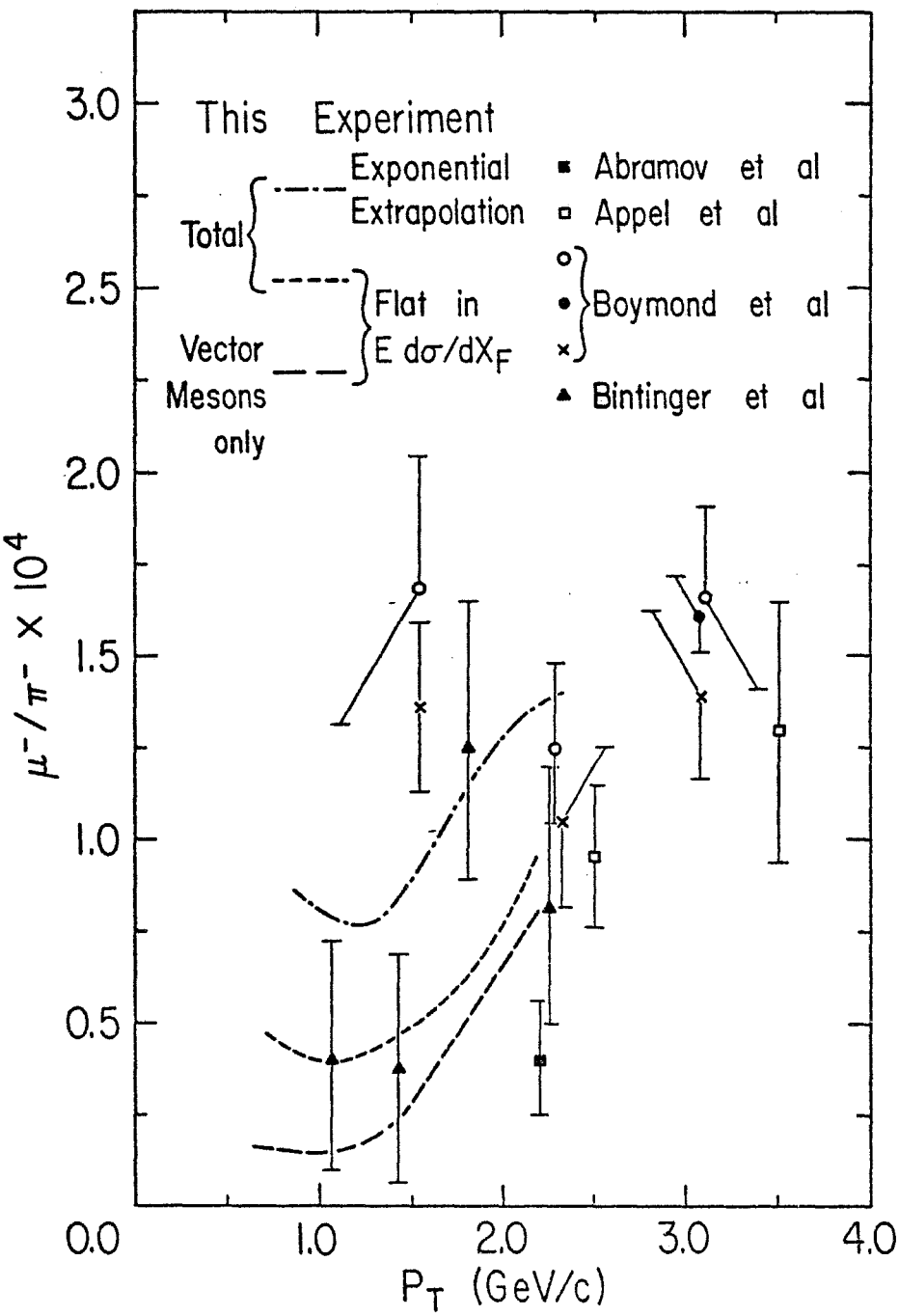
This Experiment
Total
Exponential Extrapolation
Vector Mesons only
Flat in E dσ/dX_F
Abramov et al
Appel et al
Boymond et al
Bintinger et al
μ⁻/π⁻ × 10⁴
P_T (GeV/c)
0.0
0.5
1.0
1.5
2.0
2.5
3.0
4.0

Fig. 54.--The 80 cm MWPC with side and top fan housing covers removed, with transporting hardware (top cross bars and bottom stand) attached. A one-foot rule shows the scale. In practice the chamber was hung from above to allow the hadron absorber to be rolled out (to the left).

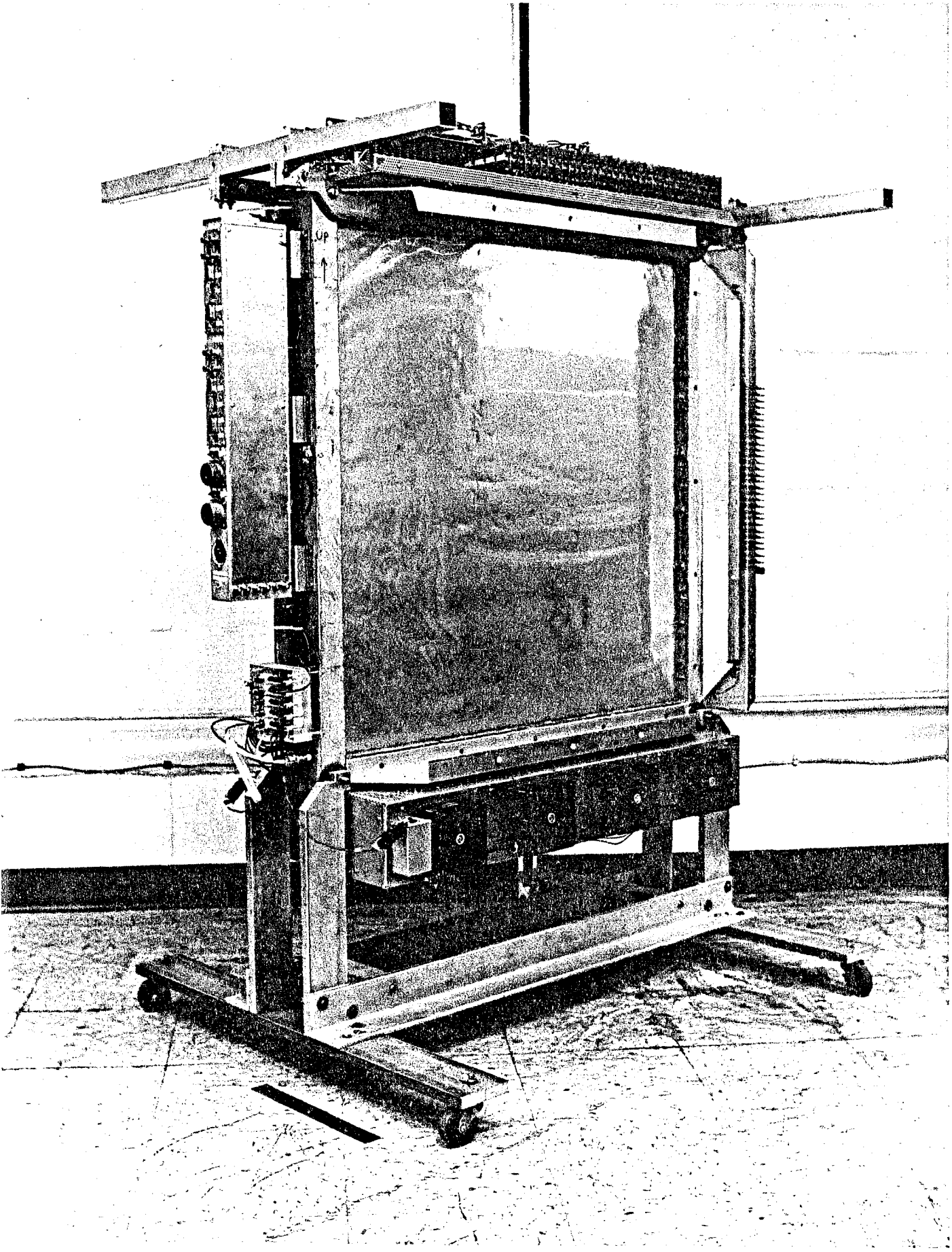
UP

Fig. 55.--The 30 cm chambers with supporting stand. The target was hung by the box-beam extending to the right. T_5 was attached to the frame from below. (The hose-clamp used to attach it is seen below the target support.)

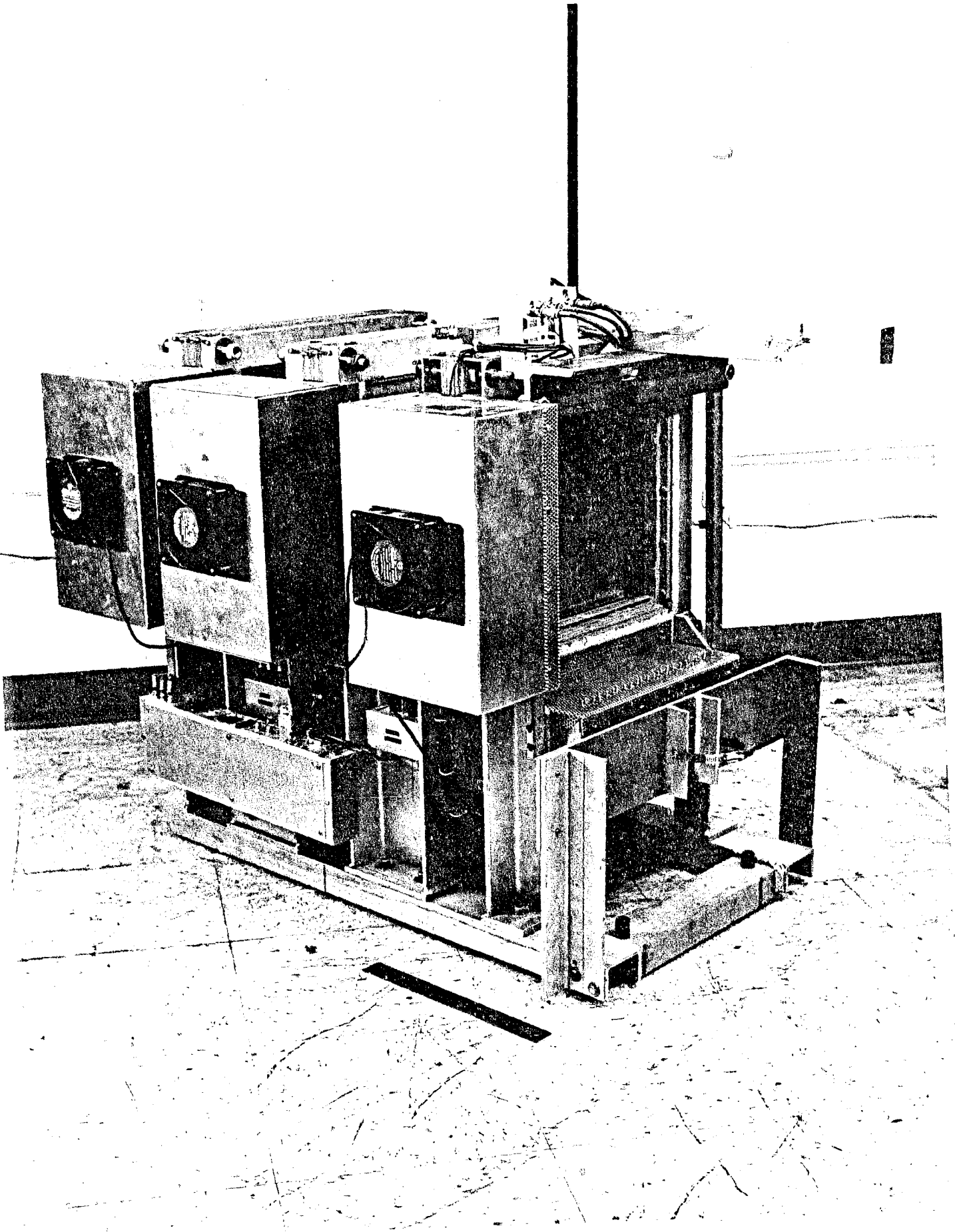

Fig. 56.--An exploded view of the 55 cm MWPC chamber frame and plane construction.

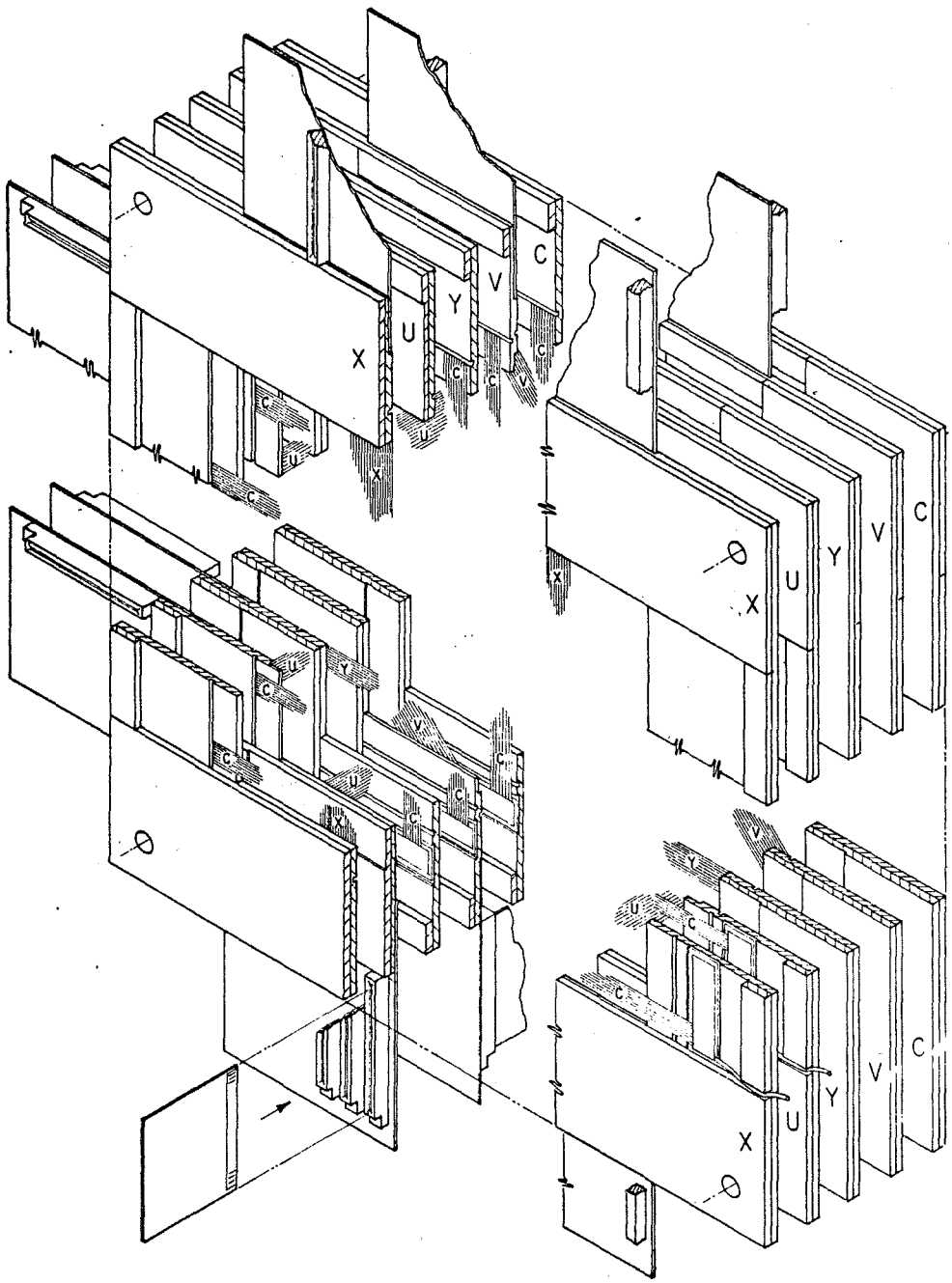
X
U
Y
V
C

Fig. 57.--The individual frames used in the absorber chambers.

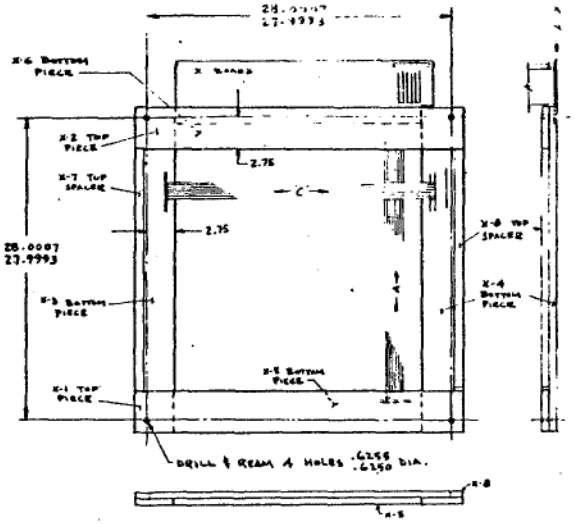

"X" Plane #1

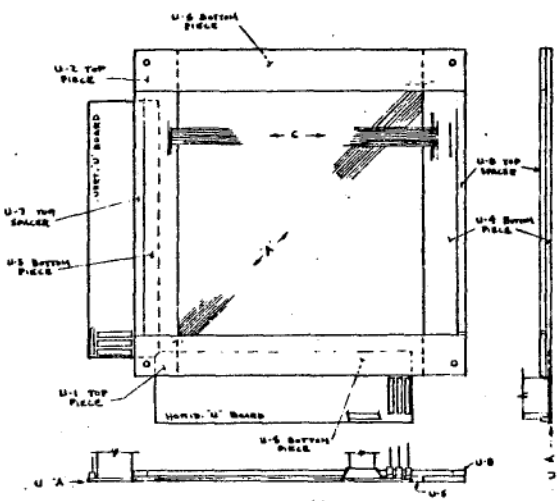

"U" Plane #2

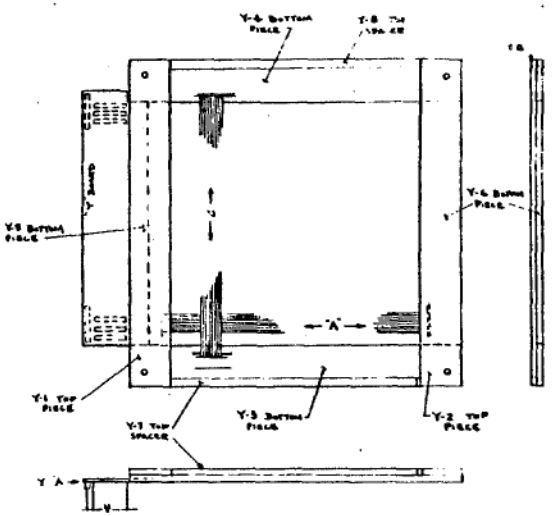

"Y" Plane #3

Note: Hole Locations Typical All Frames.

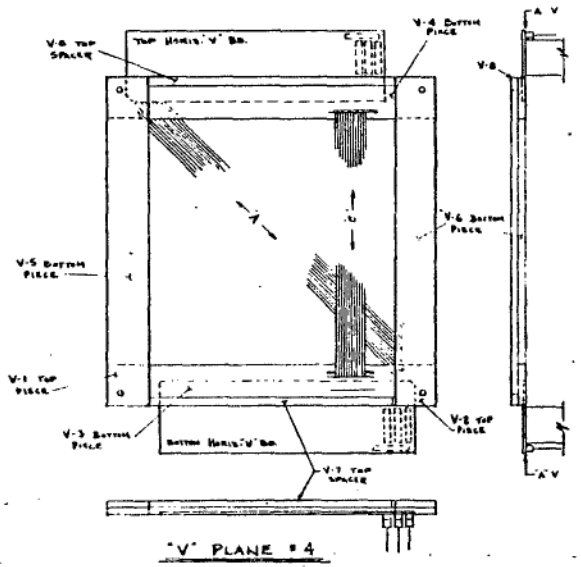

"V" Plane #4

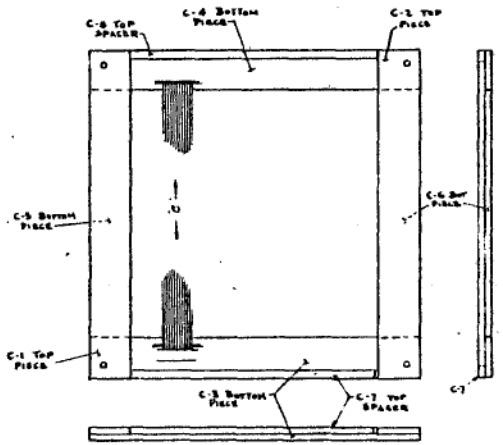

Cathode Plane #5

"C" = Cathode

"A" = Anode

Fig. 58.--An exploded view of the 30 cm chamber.

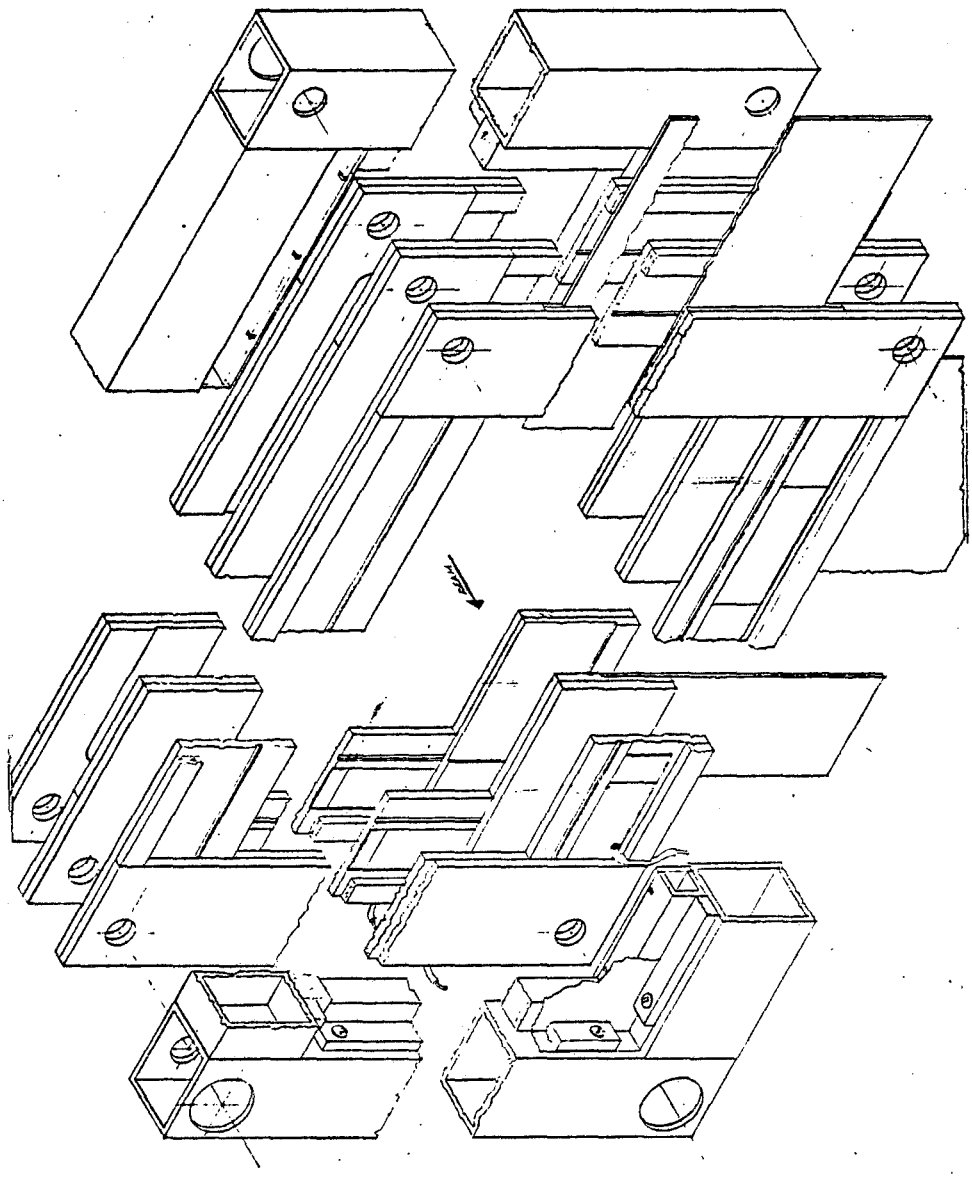

Fig. 59.--A drawing of the 55 cm MWPC frame, without C beam supports.

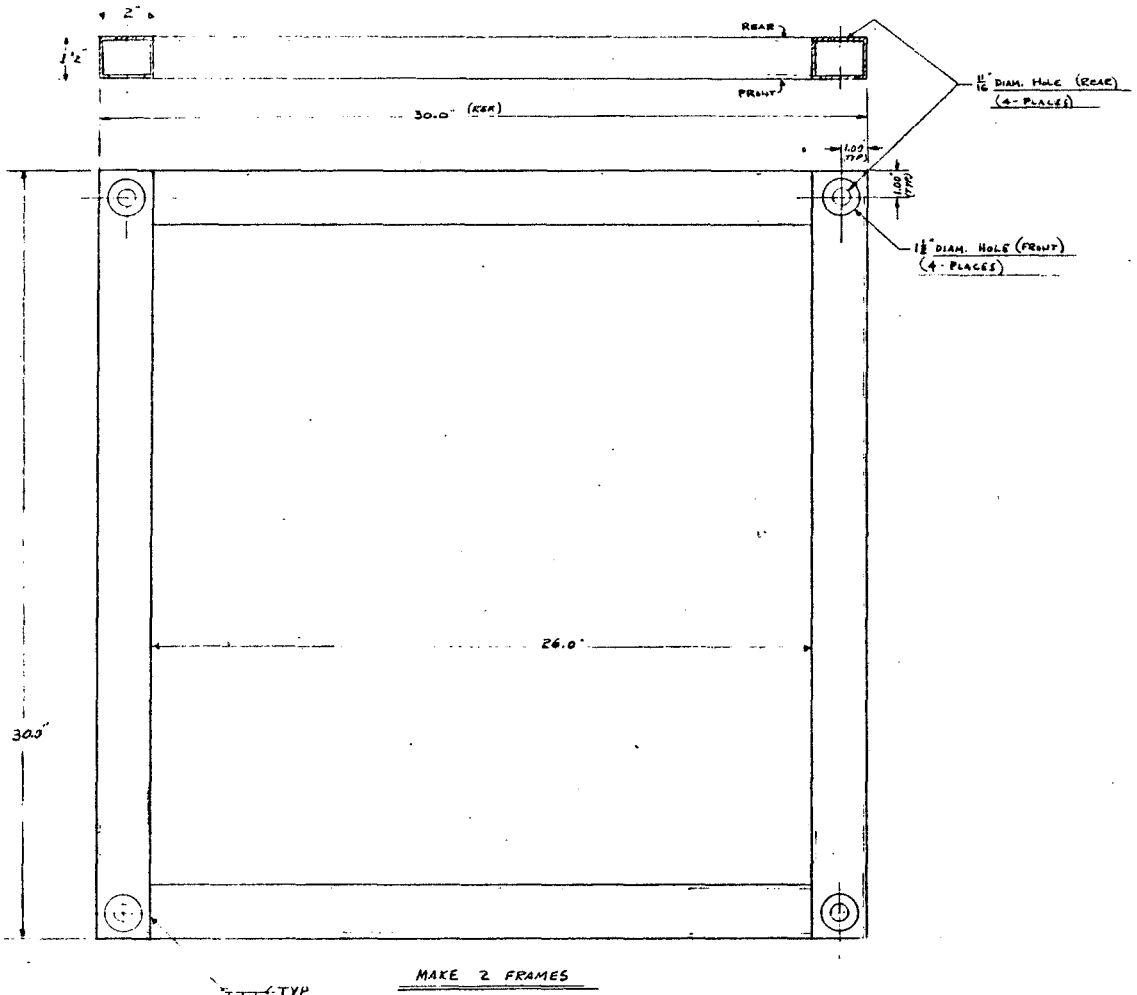

MAKE 2 FRAMES

ALUM. TUBE 6063-T52 — 2 REQ PER FRAME 1½"x2"x.125"x 26.0"
SAND BLAST ALL OVER — 2 REQ PER FRAME 1½"x2"x.125"x 30.0"

NOTES

FRAME TO BE FLAT TO WITHIN ± .010
BREAK ALL SHARP EDGES

Fig. 60.--The amplifier card used on 30 cm, 55 cm and 80 cm MWPC's.

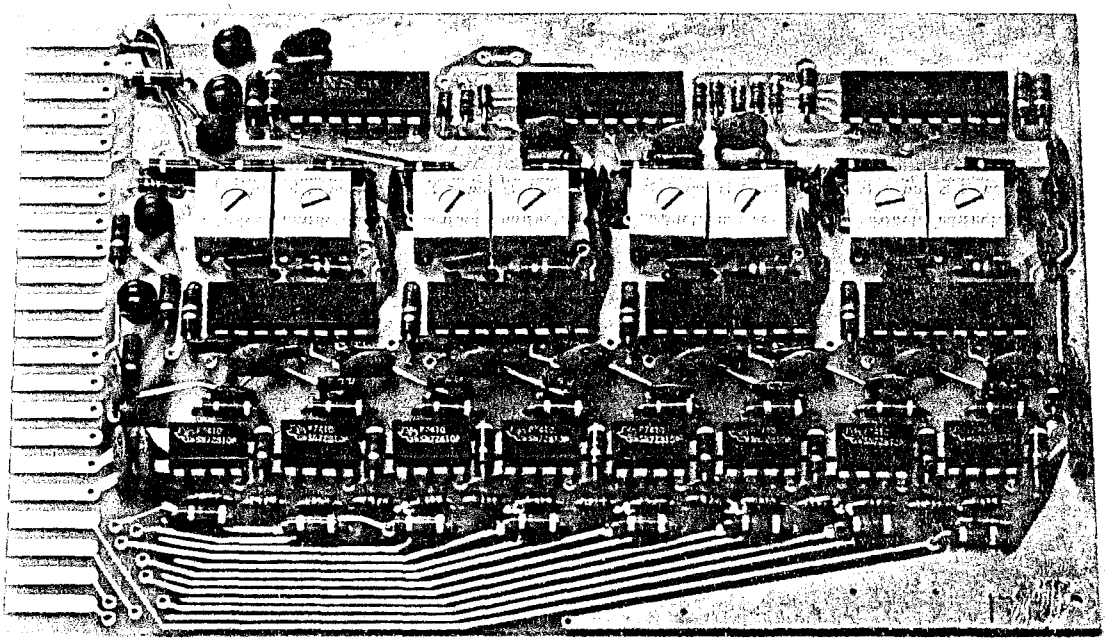

Fig. 61.--The component diagram of the amplifier and shift register card.

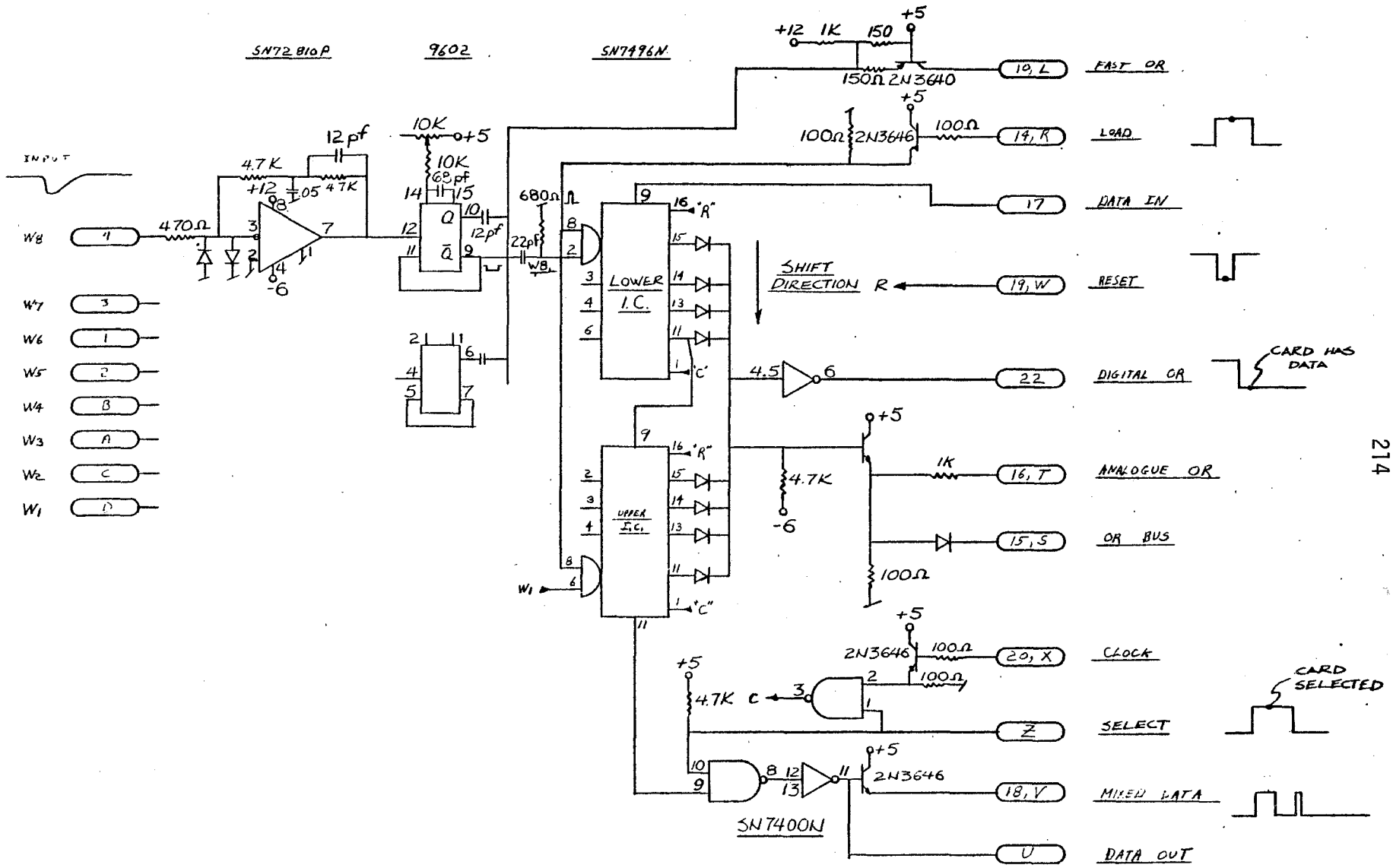
SN72810P
9602
SN7496N
INPUT
W8
W7
W6
W5
W4
W3
W2
W1
470Ω
4.7K
12pf
10K
68pf
680Ω
22pf
LOWER I.C.
UPPER I.C.
SHIFT DIRECTION
+12
+5
-6
1K
150
150Ω 2N3640
100Ω 2N3646
4.5
4.7K
SN7400N
10, L
FAST OR
14, K
LOAD
17
DATA IN
19, W
RESET
22
DIGITAL OR
CARD HAS DATA
16, T
ANALOGUE OR
15, S
OR BUS
20, X
CLOCK
Z
SELECT
CARD SELECTED
18, V
MIXED DATA
U
DATA OUT

Fig. 62.--The efficiency of the 55 cm chamber as a function of voltage for each of the four planes. Also shown is the dark current of all planes as a function of voltage.

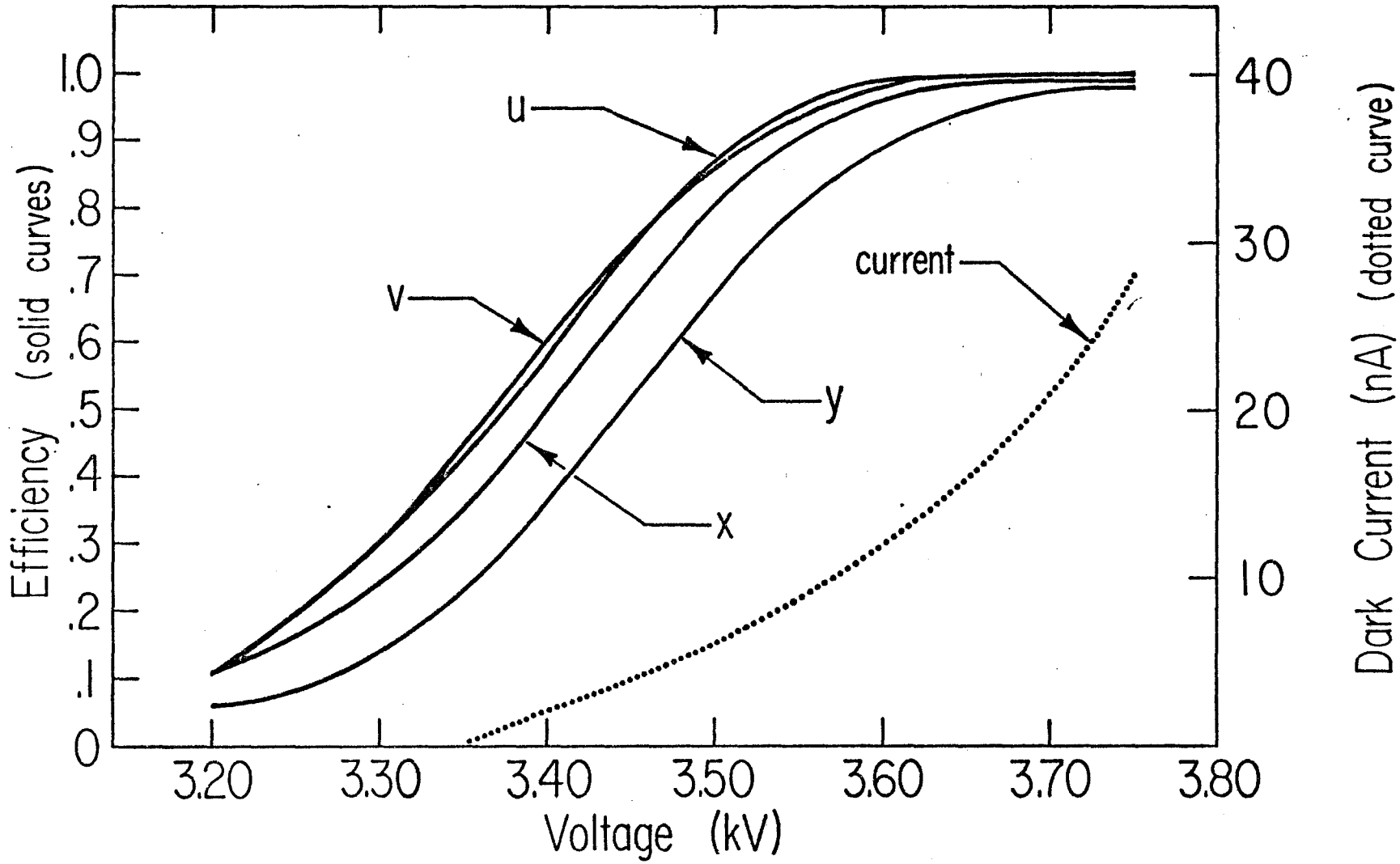
Efficiency (solid curves)
1.0
.9
.8
.7
.6
.5
.4
.3
.2
.1
0
u
v
y
x
current
40
30
20
10
Dark Current (nA) (dotted curve)
3.20
3.30
3.40
3.50
3.60
3.70
3.80
Voltage (kV)

Fig. 63.--The timing of the trip-wire signal so as to insure suppression of noise signals.

Electronics

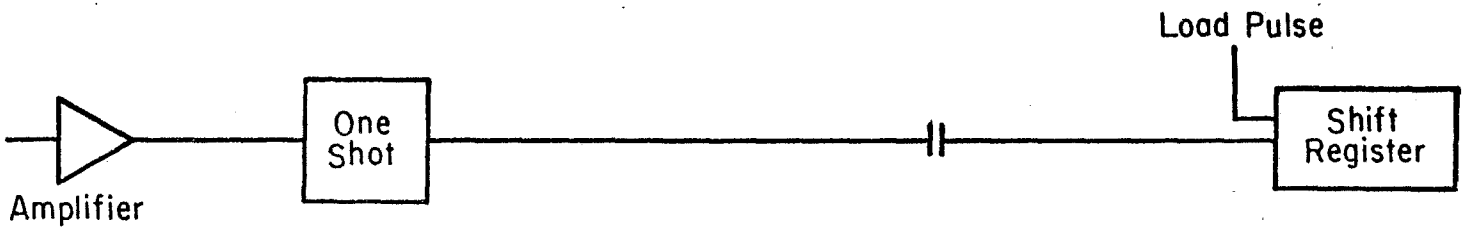

Timing

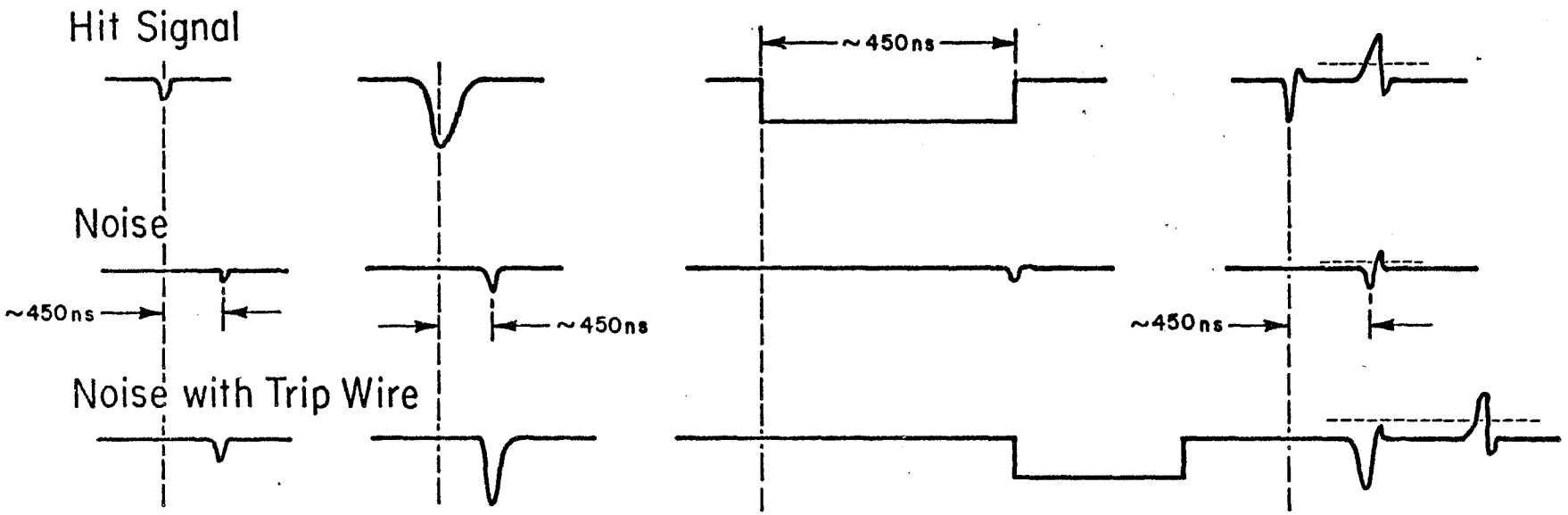

Fig. 64.--A schematic diagram of the trip-wire configuration.

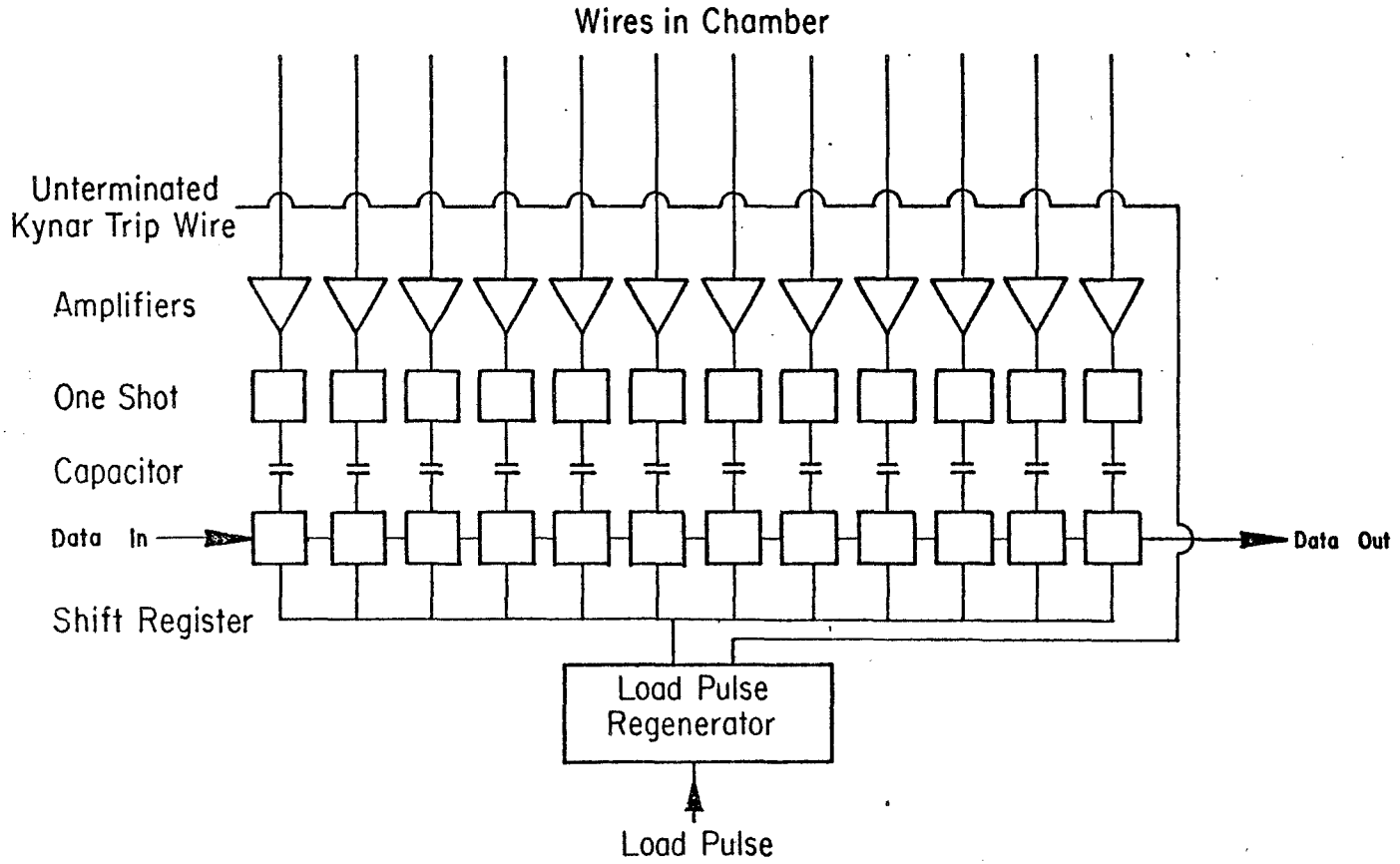
Wires in Chamber
Unterminated
Kynar Trip Wire
Amplifiers
One Shot
Capacitor
Data In
Data Out
Shift Register
Load Pulse
Regenerator
Load Pulse

Fig. 65.--The distributions of hit wires in the 55 cm chamber using a ruthenium test source. The x and y distributions are shown, along with noise observed prior to trip-sire noise suppression. The noise was suppressed to $\leq$ 0.01 per cent of the signal by use of the trip wire.

Fig. 66.--The distribution of the wire spread (or number of adjacent wires struct) in the 55 cm chamber.

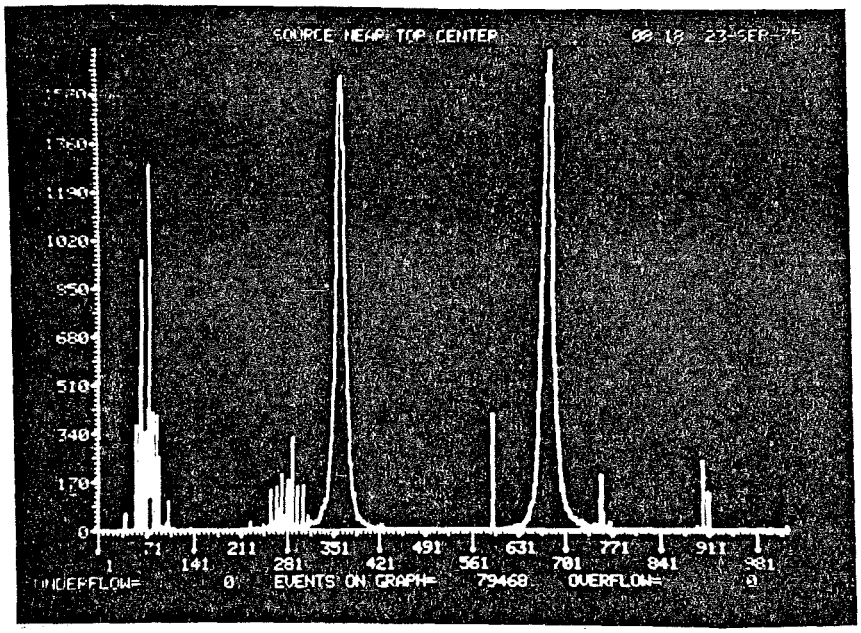
SOURCE NEAR TOP CENTER
1360
1190
1020
850
680
510
340
170
0
1
71
141
211
281
351
421
491
561
631
701
771
841
911
981
UNDERFLOW= 0
EVENTS ON GRAPH= 79468
OVERFLOW= 0

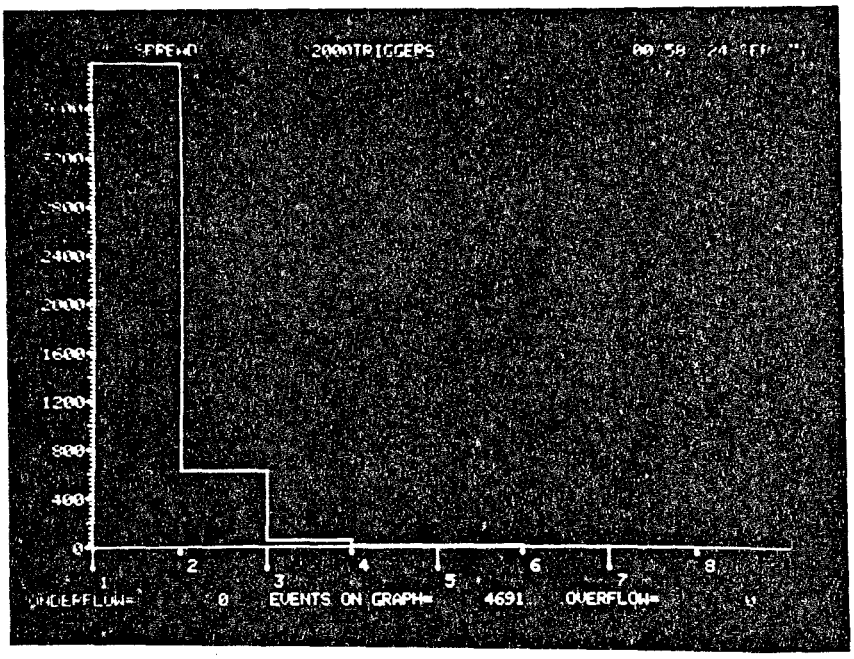
2000TRIGGERS
2800
2400
2000
1600
1200
800
400
0
1
2
3
4
5
6
7
8
UNDERFLOW= 0
EVENTS ON GRAPH= 4691
OVERFLOW= 0